CHARACTERIZATION AND APPLICATION
OF MeV ION IMPLANTED LAYERS
IN III-V COMPOUND SEMICONDUCTORS

Thesis by

Fulin Xiong

In Partial Fulfillment of the Requirements
for the Degree of
Doctor of Philosophy

California Institute of Technology
Pasadena, California

1990
(submitted on January 10, 1990)

Jan. 30, 1990

Dear Thad,

This is a way to express my special thanks to you for your guidance and encouragement to my work at Caltech.

It is also for your interest and criticism.

Best regards,

To My Parents
My Wife, Honghong
My Daughter, Jenny

ACKNOWLEDGEMENTS

Though I have had the privilege of conducting the experiments described in this thesis, the result of this work is a product of direct or indirect contributions from many individuals. I have also benefited from much help and many collaborations during the course of my graduate research at Caltech.

Foremost, I thank my advisor, Professor Thomas A. Tombrello, for his increscent guidance, continual support, and constant encouragement, which made this work possible and my study at Caltech a very memorable and profitable experience. I have always been inspired by his keen insight and creativity in scientific research, and patience in teaching, which have made their branded marks upon my memory and research.

I am deeply indebted to many people in the Basic and Applied Science Group and Materials Research Group, from whom I have been truly privileged to learn in the course of these experiments. My special gratitude goes to Prof. Thad Vreeland Jr. for his initial guidance in mastering x-ray technique as well as many invaluable discussions on data analysis and interpretation, and to Dr. Simon C. W. Nieh for his excellent collaboration on TEM work. I give my thanks to Alan Rice, whose patient advice and midnight-available help made my work in the Tandem lab very pleasant, to Steve Stryker whose technical assistance in the art and craft of machining made my experiments go smoothly and on time. I would like to thank Prof. Marc-Aurele Nicolet and Dr. David N. Jamieson for introducting me to CRBS experiments on the Pelletron machine; to Prof. Brent T. Fultz, Dr. Channing Ahn and Ms. Carol Garland for their instruction, assistance and discussion of TEM work; to C. J. Tsai for letting me use his computer code for XRC analysis.

I have also profited a great deal from fruitful interactions with many excellent scientists within and outside Caltech. I deeply acknowledge the help of Prof. Amnon Yariv at Caltech and Prof. Haris Morkoç at University of Illinois, Urbana-Champaign, who introduced me to quantum electronics and MBE technology. I highly appreciate the collaboration with Dr. Haila Wang, Dr. Tirong Chen, Ms. Yuhua Zhang, and Mr. Z. H. Chen in Yariv's group at Caltech on laser device fabrication and ion beam modification of GaAs and InP materials. I am very grateful to Dr. Steve A. Schwarz and Ms. C. L. Schwartz in Bellcore for their help on SIMS analysis.

In addition to those named above, most of the members of and visitors to this group have contributed in one way or another to my experience at Caltech. I specially acknowledge Prof. F. Rauch from Johann Wolfgang Goethe Universitat, Frankfurt, FRG, Dr. R. P. Livi from Instituto de Fisica-UFRG-9000, Porto Alegre, Brazil, Dr. Chengru Shi from Lanzhou University, China, and Dr. Zhuying Zhou from Fudan University, China for their initial collaboration on technical developments in nuclear resonant reaction analysis. I enjoyed the group tea time and many discussions with Dr. Peter Haff, Duncan L. Weathers, Steve Spicklemire, Davy Lo, Todd Jones, Shouleh Nikzad, and Phil Haubert. I also enjoyed sharing an office with Gary Gutt, although we were both too busy to talk much. My deep gratitude also goes to Michelle Vine for her assistance with secretarial tasks and travel arrangements as well as arrangement of birthday parties for me and others.

Last but not least, I would like to express my deepest gratitude to my family for their love, expectations, encouragement, and support throughout the years of my life and along my scientific path. I am also glad to express my deepest appreciation to my daughter Jenny for her many big smiles every morning and evening after her birth, which make me very happy during this last moment of this thesis writing. I dedicate this thesis to my parents, my wife Honghong, and my daughter Jenny.

Financial support of this work was provided by the National Science Foundation through grants to the Caltech Materials Research Group (DMR84-21119 and DMR88-11795) and to the Caltech Basic and Applied Sciences Group (DMR83-18274 and DMR86-15641).

ABSTRACT

Ion implantation at keV energies has become a well-established technique for surface modification of solid materials, especially semiconductors. The technique of MeV ion implantation has attracted considerable attention in recent years as it provides an extension of ion implantation technique with a high potential for interface modification of solid materials and for 3-dimensional electronic device fabrication. Extending the ion energy from keV to MeV provides many advantages in terms of the great ion range for deep implantation and the minimized surface damage for modification of deeply buried layers. It also gives rise to many interesting questions about the mechanism of radiation damage and ion-radiation-induced phase transitions. A comprehensive experimental study, from the fundamental to the practical, has been undertaken to investigate MeV ion irradiation effects in III-V compound semiconductors, especially InP and GaAs, and to explore the possibility of its application to optoelectronic semiconductor device fabrication.

Characterization of implanted samples has been conducted by a variety of analytical techniques, such as NRRA, CRBS, XRC, XTEM, HRTEX, SIMS, and IVC. The results have not only demonstrated the complementary nature of all these techniques but also have given clear pictures about the implant distribution, profiles and microstructures of radiation damage and lattice defects, structural phase transformation, and the build-up of lattice strain, as well as electrical property changes. They have revealed the physical relation among all of the effects and led to a better understanding of physical processes involved in MeV ion implantation into III-V compound semiconductors. It has been discovered that MeV nitrogen ion implantation can create a deeply buried high resistivity layer in n-type InP crystals, similar to the case where MeV oxygen ion implantation generates a semi-insulating layer in GaAs-AlGaAs systems. Application of this technique to the fabrication

of GaAs-AlGaAs quantum well laser devices with MeV oxygen ions for the electrical isolation and carrier confinement has resulted in a device with high quantum efficiency, low current threshold, and excellent electrical characteristics.

In this thesis, the experimental studies on MeV ion implanted InP and GaAs are presented. Based on the experimental results obtained, the mechanism of MeV-ion-implantation-induced damage and phase transitions in III-V coumpound semiconductors is discussed in terms of electronic spikes and nuclear spikes. A mechanism for ion-implantation-induced lattice strain in III-V compound crystals is also proposed. Finally, an example of the application of MeV ion implantaion to semiconductor laser device fabrication is given.

TABLE OF CONTENTS

ACRONYMS

CRBS	Channeling Rutherford Backscattering Spectroscopy
DCD	Double Crystal Diffractometer
EOR	End-of-Range
HEIM	High Energy Implantation
HRTEM	High Resolusion Transmission Electron Microscopy
HN	Homogeneous Nucleation
HT	High Temperature
IVC	Current-Voltage Characteristic curve
LEIM	Low Energy Implantation
LN_2	Liquid Nitrogen
LNT	Liquid Nitrogen Temperature
LPE	Liquid Phase Epitaxy
LT	Lower Temperature
MBE	Molecular Beam Epitaxy
NRRA	Nuclear Resonant Reaction Analysis
RBS	Rutherford Backscattering Spectroscopy
RS	Raman Spectroscopy
RT	Room Temperature
SIMOX	Separation by Implantation of Oxygen
SIMS	Secondary Ion Mass Spectroscopy
SPE	Solid Phase Epitaxy
SOI	Semiconductor-on-Insulator
XRC	X-ray Rocking Curve
XTEM	cross sectional Electron Transmission Microscopy
UHV	Ultra-High Vacuum

FIGURE LIST

annealed at 650°C for 1 hour, (1) implanted with a dose of $1 \times 10^{14}/\mathrm{cm}^2$, and (2) of $1 \times 10^{16}/\mathrm{cm}^2$.

FIG. 2.8. X-ray rocking curves of the 15 MeV-^{35}Cl-ion-implanted InP and GaAs from (400) symmetrical diffraction with respect to the substrate. The radiation-induced strain and the strain saturation are shown.

FIG. 2.9. X-ray rocking curves of the 5MeV-^{15}N-ion-implanted InP from (400) symmetrical diffraction with respect to the InP substrate. The evolution of radiation-induced strain is shown.

FIG. 2.10. Channeling RBS spectra of InP crystals as-implanted with 5 MeV ^{15}N at room Temperature with a sequence of doses.

FIG. 2.11. XTEM micrographs of 5 MeV nitrogen ion as-implanted InP and $< 110 >$ diffraction patterns of the buried implanted layers. The samples were implanted with a dose of a) $5\times10^{14}/\mathrm{cm}^2$, b) $1\times10^{15}/\mathrm{cm}^2$, c) $2\times10^{15}/\mathrm{cm}^2$, and d) $1\times10^{16}/\mathrm{cm}^2$.

FIG. 2.12. A plot of the width and the depth of the buried amorphous layer *versus* the implanted dose in 15 MeV Cl ion implanted InP(100) samples. The data are obtained from XTEM measurements.

FIG. 2.13. HRTEM micrographs of MeV ion as-implanted InP near interfaces, showing damage production and gradual crystalline-to-amorphous transition with increasing the implant dose. a) a dose of $1 \times10^{14}N/\mathrm{cm}^2$, in a heavily damaged area, a high density of lattice defects lying in $\{111\}$ planes; b) $2.5\times10^{15}Cl/\mathrm{cm}^2$, around the top interface, an intimate mixture of individual amorphous and crystalline pockets; c) $2.5\times10^{15}Cl/\mathrm{cm}^2$, around the inner interface, where the amorphous zone with crystalline inclusions, nuclear spike induced amorphous pockets in the ion tracks, and recoil nuclei tracks before the end of ion stopping points can be found, as indicated by small arrows; and d) $1 \times10^{16}N^+/\mathrm{cm}^2$, at the inner interface, sharp crystalline-to-amorphous transition boundary.

FIG. 2.14. A set of XRCs taken at RT from an InP sample implanted by 2 MeV oxygen ions at 77K with a dose of $2\times10^{14}/\mathrm{cm}^2$, showing the RT annealing process in MeV ion implanted InP.

gion around the active area for lateral current control and carrier confinement; b) buried cresent double heterostructure in a semiconductor-on-insulator (SOI) InP substrate prepared by MeV ion implantation.

TABLE LIST

Chapter 1

INTRODUCTION TO MeV ION IMPLANTATION

1.1 Brief Historic Review of Ion Implantation

Nuclear physicists developed the art of producing energetic ions with accelerators in the early 1930s, which led to the study of nuclear structure. During this research they noted the discoloration and modification of accelerator components and experimental targets after ion bombardment. Solid-state physicists discovered the technology to produce many new materials, especially semiconductors, which has led to a revolution in modern instrumentation. There was also a rapid expansion of research into, and a persistent demand for, techniques for modification of materials and doping of semiconductors. Joint efforts from people in these two areas in the early 1950s opened a new and challenging field of ion beam processing of materials. Using nuclear experimental approaches, several kinds of ion beam techniques have been developed for material analysis and characterization, such as nuclear reaction analysis (NRA), particle-induced x-ray emission analysis (PIXE), and Rutherford backscattering spectroscopy (RBS). In the area of ion beam modification of materials, ion implantation into semiconductors has been one of the most attractive and interesting fields and has attracted a major amount of this effort. This is the subject we address in this thesis.

The earliest report of ion beam modification of semiconductors was made by Ohl[1] in 1952, showing that ion beam bombardment could modify semiconductor diode characteristics. The first experimental study on ion implantation for electrically doping a semiconductor was reported by Cussins[2], who looked at the electrical changes in Ge after implantation with various ions. There were several patents filed in that period. In this early period, because there was not easy access to ion accelerators by solid-state physicists, a large effort was devoted to develop low-energy ion implantors for material scientists to use. The experimental research was focused on the use of low energy ions, ranging from a few keV to a few hundred keV. There was an increasing stream of publications on the research that included both theoretical and experimental work on keV ion implantation. These investigations covered the topics of ion range distribution, damage profiles, annealing studies of activation of implants and recovery of crystallinity, and device applications. The theoretical treatment in this field can be found in many publications associated with names such as Bohr, Bethe, Thompson, and Lindhard. The experimental investigations of these subjects can be found in numerous reports by a too large number of people to be listed. Extensive reviews[3–8] have been made every few years lately due to the rapid development in this field. Today, keV ion implantation has been accepted as a well-established technique in the Si industry[9,10], and is being extended to III-V compound semiconductor technology[11].

The development of processes for semiconductor technology using high energy implantation (HEIM) in the MeV range (thereafter we refer to the MeV ion implantation as high energy implantation, and to keV ion implantation as low energy implantaion (LEIM)) was limited and the progress was surprisingly slow at first. There have been more theoretical studies than experimental ones. This is not due to the lack of application potential in semiconductor technology, but to the lack of availability of MeV energy implantation machines. Another reason originated from the experimental difficulties in analysis of the deep implants and characterization of the buried implanted layers at that time. The first experiment of HEIM dated from the 1950s when nuclear physicists were trying to inject ^{3}He into Al for use as a target and noted the embrittlement and flaking of the target after the heavy dose implantation[12]. In the late 1960s, the investigation of HEIM was stimulated by establishment of an implantation beam line on the 2.5 MeV accelerator at the Air Force Cambridge laboratories in the United States and by the establishment of a "Rent-a-Beam" 4 MeV accelerator facility at Ion Physics Co. In that period, Schwuttke and collaborators[13] investigated in detail the special case of damage and annealing of ion implanted silicon where the surface remains mostly crystalline. At the end of this decade the first successful application of HEIM was made by Martin[14]. An integrated E+dE/dx detector was made by implantation with 11 MeV or 22 MeV boron ions to separate the two detector devices in a single silicon crystal. In 1970s, a few experimental investigations were continued, such as measurements of electrically active profiles in MeV ion implanted samples, studies of formation of isolation and buried layers, and applications of HEIM for surface and interface modification. It was not until the 1980s that high energy accelerators or commercial MeV ion implantors became available to solid-state physicists and material scientists. More publications on HEIM have appeared in the early five-year period of the 1980s than in the proceeding thirty years. This increased interest is also probably due to the saturation of information for LEIM and the natural evolution of interest towards the new frontiers of implantation at MeV energies. An extensive review covering the main interests shown in that period has been made by Ziegler[15]. In addition, as commercial and military uses of GaAs and other III-V compounds increased, the study of HEIM into these semiconductors also expanded.

At Caltech, starting from the early 1970s, our MeV tandem accelerator was fully devoted to applied physics and material science research. Several initial investigations in the field of MeV ion beam processing of solid materials have been performed. The work includes the development of ion beam analysis techniques (e.g., NRRA) for elemental composition profiling[16–18], MeV ion beam modification of interfaces (e.g., MeV ion beam induced enhanced adhesion in metal-semiconductor and metal-metal interfaces[19–21]), and MeV ion implantation in semiconductors (e.g., MeV ion radiation effects in GaAs[21,22] and the formation of buried insulating layers in Si crystals[23]). All of them have been successful. Following this previous work, we have continued to devote our efforts to this field (see the Appendix for work the author has done at Caltech). The main thrust of our interest lies in understanding the physical processes involved in MeV ion implantation, the formation of buried layers in III-V compound semiconductors, and its application in device fabrication. We present in this thesis the results of experimental investigations of formation, characterization, and application of MeV ion implanted layers in III-V compound semiconductors.

1.2 Introduction to MeV Ion Implantation

The development of HEIM for semiconductor device technology and other applications has been steadily increasing in recent years. The motivation may come, as mentioned above, from the scientific interest in fundamental knowledge of the processes involved. However, another driving force stems from its high application potential in the modification of interfaces, doping of deep buried layers, formation of deeply buried heterostructural layers, and for 3-dimensional device fabrication, based on the nature of HEIM[24]. For basic research interest, HEIM can also provide an efficient means for producing a buried amorphous layer in a crystal for amorphous semiconductor studies[25]. There are several areas where HEIM offers a decided advantage over alternative methods such as thermal diffusion, chemical etching, and liquid-phase and molecular-beam epitaxy (LPE and MBE). In addition to known features of highly precise control, high reproducibility, and spatial masking selectivity that LEIM has, the most obvious advantage of HEIM is the greater range of the ions, which allows them to be implanted deeper into a target or through overlying layers with minimal damage at the surface. Another distinct feature of HEIM is its electronic ionization effect (that is, electronic spikes as we will term them in this thesis) at the sample surface region during implantation. These electronic spikes may induce many other interesting phenomena, which LEIM does not have.

In order to understand the distinct features of HEIM, it is necessary to understand first how an MeV ion loses its energy when travelling in the target, and

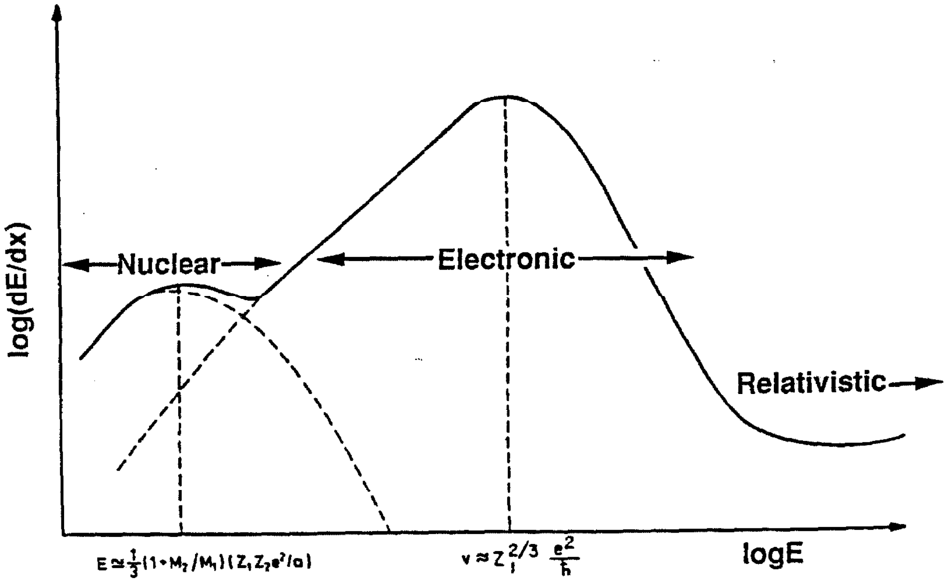

Figure 1.1 The general dependence of the energy loss per unit length for an ion in a solid, dE/dx, on its incident energy, E, in a nonrelativistic regime. (taken from Sigmund[26])

its relation to its incident energy. When an incident ion penetrates into a solid, it loses its energy by collisions along its path with electrons and nuclei in the target. The strength and probability of the collision would not only depend on the target properties, but would also be determined by the ion's charge and energy. Fig. 1.1 illustrates a schematic graph of the energy loss per unit length of an energetic ion, dE/dx, as a function of the ion energy, E. There exist two distinct regimes — a nuclear stopping regime and an electronic stopping regime. In the nuclear stopping regime where the ion's energy ranges from a few eV/amu to a few tens of keV/amu, the primary means of energy loss of the ion is through screened-Coulomb collisions with nuclei in the target. The energy transfer and stopping cross section can be estimated by classic two-body elastic collision kinematics[27]. When the direct transfer of kinetic energy from the ion to a target nucleus is greater than a threshold, it results in considerable atomic recoil motion and displacements. At a higher energy — particularly in the range of a few hundred keV/amu to a few MeV/amu — electronic stopping through interactions of the ion and the electrons in the solid dominates the energy loss process. In this electronic stopping regime, the ion's kinetic energy is dissipated primarily in the production of ionized or excited electronic states of the lattice atoms in the target. The atomic displacement can be induced in this regime only if other fast deexcitation mechanisms are unavailable. The electronic energy loss is determined by the properties of the incident ion itself, and its maximum value lies at the ion incident energy about $v \approx Z^{2/3}\ e^2/\hbar$. For instance, an oxygen ion has its maximum electronic energy loss around 6~8 MeV. While, the nuclear energy loss is dependent on the target atoms; and its maximum loss occurs at the incident energy, $E \simeq (1/3)(1+M_2/M_1)(Z_1 Z_2 e^2/a)$, about a few keV/amu for most light ions. Therefore, in the context of these two energy loss regimes, one realizes that the case of LEIM lies in the nuclear energy stopping regime, while HEIM employed in this work falls into the regime where the electronic stopping initially dominates, but below the maximum electronic energy loss region.

Due to energy transfer through ion-electron collisions in the target surface region, an MeV ion eventually loses its kinetic energy and gets into the keV range. Then the ion behaves very much the same as a keV ion, where the nuclear stopping dominates. Fig. 1.2 shows an example of stopping powers of 200 keV and 5 MeV oxygen ions in GaAs as a function of the ion's penetration depth. They were calculated by a program that uses the theory of the transport of ions in matter (TRIM)[27]. As seen in the figure, the ion energies have determined the maximum penetration range of 5000 Å for 200 keV and 3.6 μm for 5 MeV. In the low energy case, the electronic stopping ($(dE/dx)_e$ = Se) and nuclear stopping ($(dE/dx)_n$ = Sn) are comparable over the whole range of the ion path, while there exist two distinguishable regions for MeV ions. As most of the range (Region 1, about 3.1 μm) is

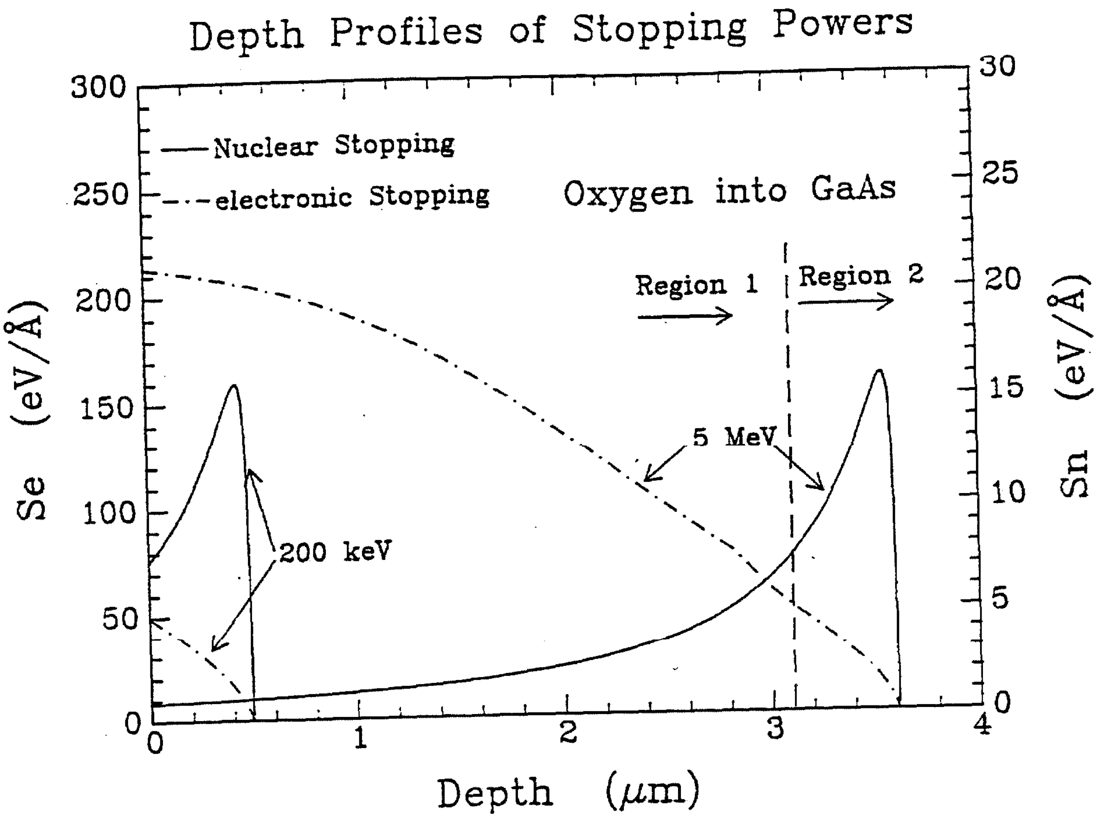

Figure 1.2 Depth profiles of nuclear and electronic energy losses of oxygen ions in energies of 200 keV and 5 MeV in GaAs.

dominated by the electronic stopping (Se >> Sn), in the last 0.5 μm region (Region 2), the behavior of both electronic stopping and nuclear stopping is very much like the case of the keV ions. The nuclear stopping is peaked in this region, with a tail extending into Region 1. The nuclear stopping power in Region 2 is typically several ev/Å, higher than the threshold energy (~10 ev/atom) required for a lattice atom's displacement. Thus, significant structural damage is produced in this region by ion-nucleus cascade collisions and lattice atomic displacements. An amorphous layer forms when individual damage zones uniformly overlap. This is the most important region for application in semiconductor device processing, and thus has attracted the most attention. In Region 1, however, the electronic stopping induces electronic excitation and ionization of the target atoms (electronic spikes) and does not cause direct lattice displacement unless the target is an insulating material. It distorts the electronic configuration of the lattice and changes the charge state of lattice atoms and defects. As a result, it will stimulate atomic diffusion, defect migration, defect recombination and other secondary effects. The effect of the electronic spike has attracted interest and has been employed for studies of MeV ion-induced crystal regrowth[28], MeV ion bombardment stimulated impurity interdiffusion[29], and MeV ion modification of the surface[30]. However, considering structural damage in MeV ion implanted samples, the damage in the target surface is minimal and contains only point defects caused by the tail of nuclear stopping damage. Thus, we can take advantage of this in the interface modification of deeply buried layers with an undamaged surface, and in three-dimensional device fabrication.

1.3 MeV Ion Implantation into III-V Compounds — An Overview of the Thesis

Application of ion implantation, especially with keV ions, for Si device processing has been a standard technology in the Si industry. However, along with epitaxial growth techniques (such as LPE, MBE, and MOCVD) it is extremely useful and important for III-V compound semiconductor technology because the alternative processing methods of thermal diffusion and chemical etching are rather hard to control. HEIM in III-V compound semiconductors has received considerable attention in recent years due to practical imperatives arising from the demands of microelectronics and optoelectronic technology. Application of ion implantation in GaAs device fabrication has achieved great success, where ion implantation is the preferred method for forming active layers for production GaAs FET devices and integrated circuits[11].

In situations of practical importance, however, the damage mechanisms as well as other associated physical processes during the ion implantation are severe.

A thorough understanding of the nature of these processes is crucial for appropriate application of ion implantation. Only if this is accomplished can one take advantage of MeV ion implantation to tailor devices to specific requirements in the semiconductor technology. III-V compound semiconductors are more complex systems than Si and Ge, because primary defect formation in a binary compound is more complicated, and the threshold energies for damage production and crystalline regrowth are much lower than for Si. It is the purpose of our research to investigate further the physical processes involved and to get a good understanding of the mechanism of the transient physical processing and damage production that occurs in the high-energy heavy-ion implantation into III-V compound semiconductors.

The work described in this thesis is divided into three parts. In the first part, we present the experimental results of the investigation of MeV ion implantation into III-V compounds. Chapter 2 deals with the case of InP materials, for which few HEIM results have been previously documented. We have found that MeV nitrogen ion implantation can generate a buried high-resistivity layer in InP, which can be used for electrical isolation in device fabrication. By characterizing the implanted samples with several analytical techniques (such as NRRA, CRBS, XTEM, and XRC) we have obtained a clear picture of the implant depth distribution, lattice damage profile, microstructural changes, and phase transitions induced by ion implantation as well as subsequent thermal annealing. In Chapter 3, the study of ion implantation into the GaAs system is presented. The investigation emphasized ion-implantation-induced electrical change and the influence of the target temperature on the radiation-induced lattice damage. We have confirmed oxygen-ion-implantation-induced high resistivity in the n-type GaAs by *in situ* resistivity measurement. It has also been found that the implantation at room temperature involves significant dynamic *in situ* annealing, which has been confirmed by lattice strain measurement with the XRC and damage profiling with the CRBS. In the AlAs/GaAs superlattice system, we have discovered that oxygen ions can induce compositional disordering with Al interdiffusion through both the electronic spike effect and the nuclear spike effect. Low temperature implantation greatly enhances this effect. Here, critical dose for completed lattice disordering would be lower by one or two orders. From the results presented in Part 1, we have obtained a better insight of the physical processes involved in MeV ion implantation. Two important issues are treated in Part 2. In Chapter 4, we discuss the defect generation and lattice strain build-up in ion-implanted III-V compounds. A kinematic model describing defect generation, migration, and recombination in ion implantation is proposed. Based on this model, the mechanism of lattice strain generation and build-up in terms of its magnitude and sign is presented. In Chapter 5, the mechanisms for lattice structural damage and phase transitions during MeV ion implantation as well as during thermal annealing are examined. It leads us to a clear understanding of the effects of the electronic spike and nuclear spike induced by MeV ions. We have also obtained a comprehensive picture of defect annealing and recrystallization in an MeV-ion-implanted amorphous layer under thermal heating. In the last part (Chapter 6), an example of the application of MeV ion implantation for optoelectronic device fabrication is presented. We utilized 2 MeV oxygen ions implanted into a single quantum well GRINCH laser device for electrical isolation and interface modification. The devices fabricated in this way have demonstrated excellent performance with better electrical and optical confinement.

1.4 References

1. R. Ohl, Bell Sys. Tech. J. 31 (1952) 104.
2. W. D. Cussins, Proc. Phys. Soc. B68 (1955) 213.
3. *Ion Implantation in Semiconductors*, eds. S. W. Mayer, L. Erikson, and J. A. Davies (Academic Press, New York) (1970).
4. *Ion Implantation in Semiconductors,* eds. I. Ruge and J. Graul (Springer-Veerlag, Berlin) (1971).
5. *Ion Implantation,* eds. G. Dearnaley, J. H. Freeeman, R. S. Nelson, and J. Stephen (North-Holland, Amsterdam) (1973).

6. *Ion Implantation Techniques,* eds. H. Ryssell and H. Glawisching (Springer-Veerlag, Berlin) (1982).
7. *Ion Implantation — Science and Technology,* ed. J. F. Zeigler (Academic Press, New York) (1984).
8. *Ion Implantation and Beam Processing,* eds. J. S. Williams and J. M. Poate (Academic Press, New York) (1984).
9. O. W. Holland, J. Narayan, and D. Fathy, Nucl. Instr. and Methods, B7/8 (1985) 243, and references therein.
10. Y. Akasaka, Nucl. Instr and Methods, B37/38 (1989) 9.
11. R. E. Williams, *Gallium Arsenide Processing Techniques*, (Academic Press, New York) (1987) p.47.
12. W. M. Good, W. E. Kunz, and C. D. Moak, Phys. Rev. 94 (1954) 87.
13. See listed bibliography in Ref. 15.
14. F. W. Martin, Nucl. Instr. and Methods, 72 (1969) 223.
15. J. F. Ziegler, Nucl. Instr. and Methods, B6 (1985) 270.
16. D. A. Leich, PhD thesis, Caltech (1973) unpublished.
17. F. Xiong, F. Rauch, C. R. Shi, Z. Zhou, R. P. Livi, and T. A. Tombrello, Nucl. Instr. and Meth. B27 (1987) 432.
18. F. Xiong, T. A. Tombrello, H. Z. Chen, H. Morkoç, and A. Yariv, J. Vac. Sci. Technol. B6(2) (1988) 758.
19. J. E. Griffith, Y. Qui, and T. A. Tombrello, Nucl. Instr. and Meth. 198 (1982) 607.
20. R. P. Livi, S. Paine, C. R. Wei, M. H. Mendenhall, J. Y. Tang, T. Vreeland Jr., and T. A. Tombrello, Mater. Res. Soc. Symp. Proc. 37 (1985) 467.
21. C. Y. Wei, PhD thesis, Caltech (1985) unpublished.
22. T. T. Bardin, J. G. Pronko, F. A. Junga, and W. G. Opyd, A. J. Mardinly, F. Xiong, and T. A. Tombrello, Nucl. Instr. and Methods, B24/25 (1987) 548.
23. C. W. Nieh, F. Xiong, C. C. Ahn, Z. Zhou, D. N. Jamieson, T. Vreeland Jr., B. Fultz, and T. A. Tombrello, Mat. Res. Soc. Sym. Proc. Vol. 107 (1988) 73.
24. T. A. Tombrello, J. Physique (Paris), Col. C2 (1989) C2-1.

25. J. S. Lannin, Physics Today, 41(7) (1988) 28.

26. P. Sigmund, in *Inelastic Ion-Surface Collisions*, ed. N. H. Tolk and J. C. Tully (Academia Press, New York, 1977), p.121.

27. J. F. Ziegler, J. P. Biersack, and U. Littmark, *The Stopping and Range of Ion in Solids*, (Pergamon press, New York) (1985).

28. J. M. Poate, J. Linnros, F. Priolo, D. C. Jacobson, J. L. Batstone, and M. O. Thompson, Phy. Rev. Lett. 60 (1988) 1322.

29. J. M. Poate, D. C. Jacobson, F. Priolo, and M. O. Thompson, Mat. Res. Soc. Sym. Pro. Vol. 122 (1988) 533.

30. P. A. Ingemarsson, A. Hedin, B. U. R. Sundqvist, T. A. Tombrello, and R. E. Johnson, Rad. Eff. and Defects in Solids, Vol. 108 (1989) 205.

Chapter 2

MeV ION IMPLANTATION INTO InP COMPOUND SEMICONDUCTORS

2.1. Introduction

InP is an important III-V compound semiconductor because InP and alloys on InP substrates can be used for the fabrication of microwave, integrated electronic, and optoelectronic devices on the same chip for high speed computer and communication applications. This is due to the fact that high electron mobility can be obtained in n-type InP materials, and the emission wavelength of the InGaAsP/InP material system falls into the right range for present optoelectrical fiber communication.

As is well known, ion implantation has been widely used for semiconductor doping and surface property modification as well as device fabrication[1]. It is extremely useful and important in III-V compound semiconductor technology because the alternative method, thermal diffusion processing, is rather hard to control. Application of ion implantation to GaAs has achieved great success in the fabrication of GaAs FETs and integrated circuits[2,3], but application to InP is just at the beginning stage, in part because the potential of this compound in device technologies has been widely recognized for only about ten years and because it is thought to have similar properties to GaAs in several respects.

The thrust of our effort on the study of MeV ion implantation into InP is to create a deep buried semi-insulating layer under a semiconducting crystalline layer, also known as a semiconductor-on-insulator (SOI) structure, which may be used as a substrate for laser device fabrication and other integrated optoelectronic devices, or to produce an electrical isolation of a desired region in a device. A method called separation by implanted oxygen (SIMOX)[4] has been developed in silicon device technology, which requires high-dose ($2\times10^{18}/cm^2$) oxygen ion implantation plus subsequent high temperature annealing. Among III-V compound semiconductors, most of the interest has been focused on ion implantation in GaAs. It is reported that proton or deuteron bombardment[5,6] and implantation of oxygen ions[7,8] into GaAs can create excellent electrical isolation. This technique has been employed for fabrication of GaAs devices such as GaAs/AlGaAs optoelectronic lasers[9−11] and microwave devices[12]. Several works on InP have been reported. In 1977 Donnelly and Hurwitz[13] reported using proton bombardment to make p-type InP highly resistive, but they observed that the bombarded layer converted to n-type material at high dose, and the maximum observed resistivity of proton bombarded n-type InP was approximately 10^3 ohm-cm. In 1983 similar work was reported by Focht and Schwartz[14]. They used deuteron bombardment to make high resistivity layers in p-type InP and showed the relationship of sample resistivity to bombardment dose. In n-type InP, a semi-insulating layer with a resistivity as high as 10^6 ohm-cm made by Fe-ion implantation has been demonstrated by Donnelly and Hurwitz[15], employing Fe-doping during the growth of bulk semi-insulating InP crystals. A technique of this kind has been utilized to make channeled substrate buried heterostructure lasers[16]. In our study[17] it has been found that implantation with MeV nitrogen ions at a moderate dose can create a high resistivity layer buried deeply inside an InP crystalline substrate.

A comprehensive study on MeV ion implanted InP crystals has been undertaken using a variety of techniques, in order to understand the radiation damage mechanism, crystalline structural phase transitions, and electrical modification as well as the influence of post-implantation annealing. The distribution of the implanted ions was determined by using nuclear resonant reaction analysis (NRRA).

Radiation damage and lattice strains induced by the implanted ions were measured with the x-ray rocking curve technique (XRC). Channeling Rutherford backscattering spectrometry (CRBS) and cross-sectional and high resolution transmission electron microscopy (XTEM and HRTEM) have been employed to observe the structural changes and radiation-induced defect distribution in the as-implanted and subsequently annealed crystals. The electrical change has been examined with the I-V characteristic curve (IVC) measurement. These techniques have clearly revealed substantial changes in structural properties and radiation-induced damage distribution as well as the influence of post-implantation annealing in ion-implanted InP samples. The results from these measurements are shown to be consistent with each other, and have led to a coherent description of the effects of the implantation and subsequent annealing.

In this chapter, the experimental aspects and the charaterization results are presented in detail. The mechanisms for damage production, phase transitions, and other associated phenomenon based on these results will be discussed in Chapters 4 and 5. Its application for device fabrication will be proposed in Chapter 6.

2.2. Experimental Aspects

2.2.1. Sample Preparation

The samples used in this study were cut from n-type InP single crystalline wafers. They were 0.5 mm thick with a polished surface in the (100) orientation with an Sn-doping concentration of $\sim 10^{18}/\mathrm{cm}^3$. Implantation was done with the Caltech 6 MV EN-tandem accelerator. The beams of nitrogen, oxygen, or chlorine ions in the energy range of 2 to 15 MeV were used. In order to make depth profiling easier, ions of the rare isotope, ^{15}N, were also used. The incident beam was uniformly defocused and projected onto the sample through a 6×6 mm^2 collimator. The samples were irradiated at ambient room temperature onto the front polished surfaces at a beam flux of $0.5\sim0.8$ μA/cm^2. The doses ranged from 5×10^{13} to 5×10^{16} ions/cm^2. During implantation, the sample was tilted about 5~7 degrees to minimize the possibility of ion channeling. The beam flux had to be limited to under $1\mu A/cm^2$ to prevent the sample from overheating, which was found to cause *in situ* dynamic annealing during implantation.

Post-implantation annealing was done by the conventional process using a graphite strip heater with an ambient H_2 gas flow. Samples were uncapped and set in the heater in the face-to-face configuration with a large piece of virgin InP crystal covering the implanted sample surfaces. This provides a local phosphorus pressure to prevent compositional dissociation of InP occuring near the surface during high temperature annealing. For the detailed study of the influence of annealing temperature on the lattice strain relaxation, a process of isochronal annealing was carried out with a step of 50°C every 15 min up to 600°C. Based on the XRC study of this isochronal annealing, which showed complete strain recovery for ion-irradiated InP at temperatures higher than 450°C, the temperature of 500°C for 20 min was chosen for a normal annealing process. As a special test, a few samples were also annealed in a liquid-phase-epitaxial (LPE) growth furnace at 650°C for one hour. This condition was taken to simulate the environment during crystal regrowth by LPE for further steps in device fabrication.

2.2.2. Sample Characterization

In order to evaluate the property changes in the samples after implantation, both the as-implanted and implanted-annealed samples were subsequently characterized by a variety of analytical techniques available in the laboratories in the Caltech Material Research Group.

1. Implant Depth Profiling by NRRA

Nuclear resonant reaction analysis (NRRA) has been well developed and applied extensively in the last decade. This technique has proved to be valuable in

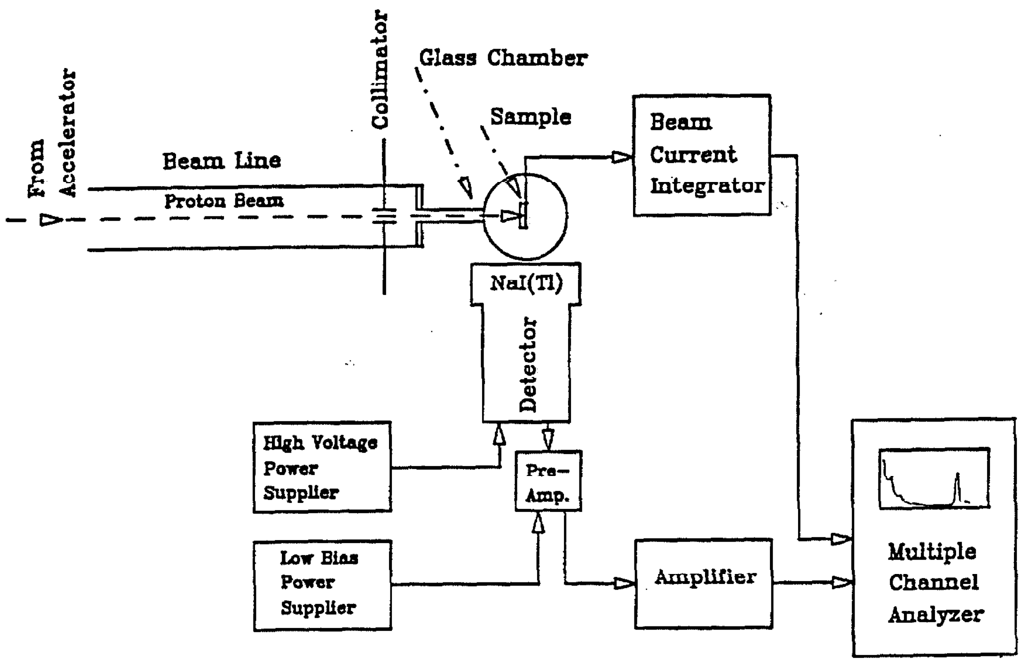

Figure 2.1 Schematic of experimental set-up for nuclear resonant reaction analysis.

providing detailed depth profiles of certain elements in materials. Its success depends on the existence of an isolated δ-function-like resonance in a nuclear reaction involving the element to be profiled. Its principle can be found elsewhere[18].

To locate precisely the implanted nitrogen with depth in InP crystals, the resonant reaction $^{15}N(p, \alpha\gamma)^{12}C$ at a proton energy of 897 keV was employed. The reverse reaction $p(^{15}N, \alpha\gamma)^{12}C$ has been investigated intensively in this laboratory[18]. We found that the resonance at 13.35 MeV for incident nitrogen-15 ions (corresponding to an incident proton energy at 897 keV in the reaction of $^{15}N(p, \alpha\gamma)^{12}C$) can provide high sensitivity and good depth resolution for depth profiling. In the measurement, the characteristic 4.43 MeV γ-rays emitted promptly during the de-excitation of excited states of the residual nucleus $^{12}C^*$ were detected. The yield, as the incident beam energy is varied, gives a direct indication of element concentration as a function of depth in the target. The experimental set-up is shown in Figure 2.1, which is the same as that used for hydrogen depth profiling, described in detail in Ref. 18. It consists of a glass chamber with a sample holder, a NaI(Tl) scintillation detector for γ-ray detection, electronics for power supply and pulse analysis, and a beam current integrator. In the resulting profiles, the depth scale is converted from the corresponding incident proton beam energy using the stopping power, which can be estimated using the InP density of 3.95×10^{22} atoms/cm^3 and stopping cross sections for single-element solids found in standard references[19]. The yields were normalized by setting the integrated yield under the peak to be equal to the implanted doses.

2. Electrical Evaluation with IVC

To find the electrical property change in these nitrogen-ion-implanted InP samples, IVC measurement was conducted in the face-to-back mode, as shown in Figure 2.2. Metallized ohmic contacts with GeAu/Au (about 1000 Å) were evaporated on both sample surfaces, an array pattern on the front face with a contact pad size of 150×150 μm^2, and a full surface contact on the back face. These samples were then alloyed at 380°C for 20 sec. The IVC measurement was made with a Tektronix type 576 transistor curvetracer, biasing the sample positive on the front surface contact pad. The slope of the I-V curve was taken, which gives a value of the resistance, R_t, at a given bias voltage point. Then, an average resistivity, ρ_i, of the buried implanted layer is deduced based on a simple model given by Focht and Schwartz[14]:

$$\rho_i = R_t A / W_i,$$

where A is the area of the metal ohmic contact pat. W_i is the width of the buried implanted layer, which is believed to contribute the most to the value of R_t measured

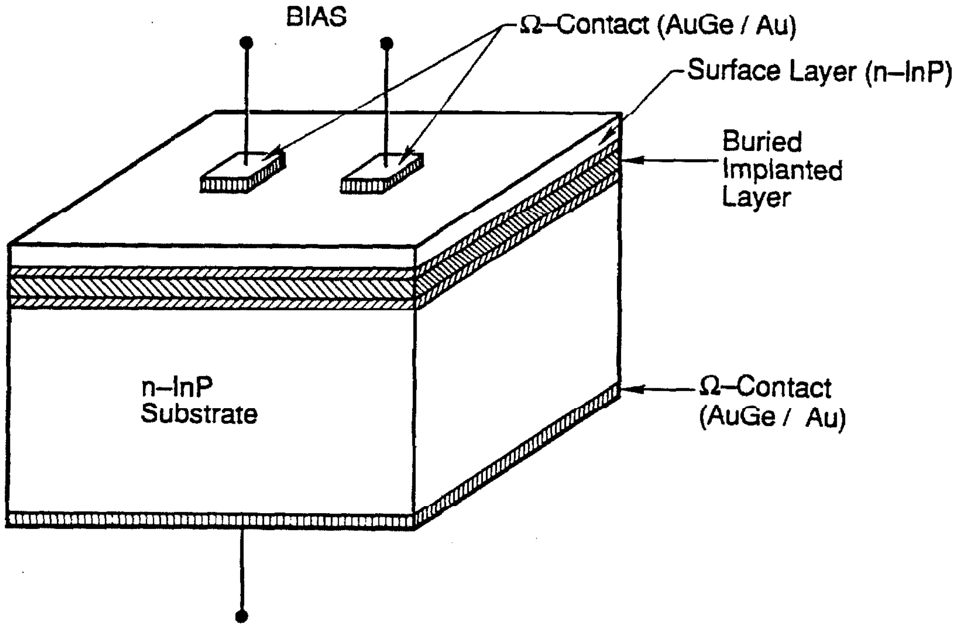

Figure 2.2 Schematic of sample chip for the current-voltage characteristic curve measurement.

and that dominates the resistance due to the remaining bulk material and the contacts.

A testing measurement on a virgin InP sample ensured the ohmic nature of metallization contacts with a bulk resistance less than 1 ohm.

3. Lattice Strain Measurement by the XRC Technique

The so-called x-ray rocking curve (XRC) technique based on x-ray double-crystal diffractometry (DCD) is a very sensitive, precise, nondestructive, and rapid technique for crystalline structural analysis, especially for deformation-induced strain

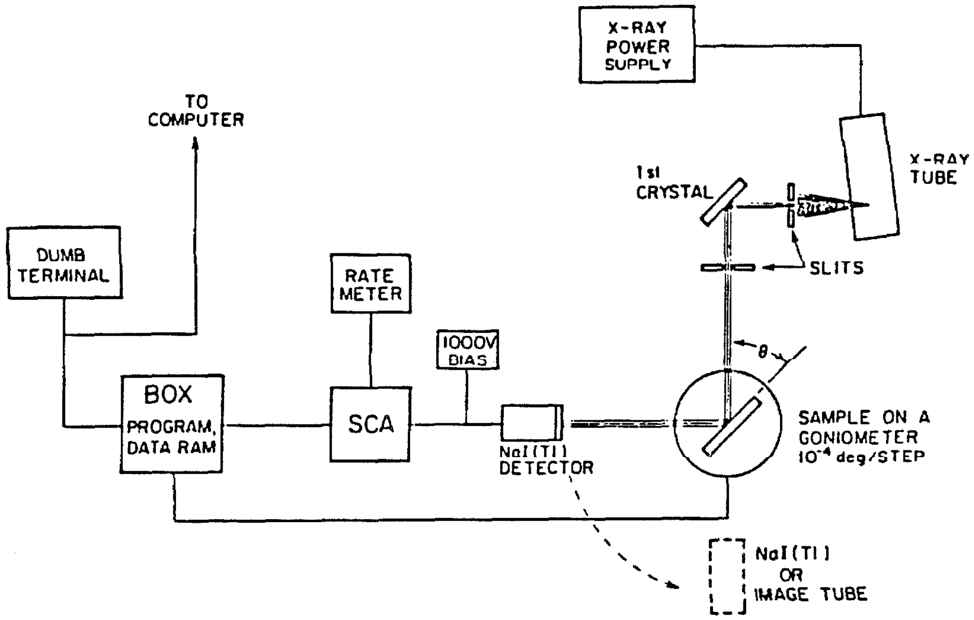

Figure 2.3 Schematic of experimental apparatus for x-ray rocking curve measurement in the Caltech Material Research Laboratory.

and damage depth profiling in semiconductor crystals[20−22]. Much progress was made during the last ten years both in the theoretical and the experimental aspects of the XRC technique. Many successful applications have demonstrated its capability for the study of imperfect crystals, superlattices, epitaxial layers, as well as radiation-induced damage and strain in semiconductors. We have used this method in characterizing the high-energy heavy-ion implanted III-V compound crystals.

The XRC measures the reflecting power of the sample as a function of the deviation of the incident angle from the Bragg angle. In the measurement, the sample is mounted on a goniometer that rotates (i.e., "rocks") the sample crystal by a step angle with a high precision of up to one thousandth of a degree at a time. At each step the reflection intensity is measured and recorded by a computerized data acquisition system. Figure 2.3 shows a schematic of a typical system developed at the Caltech Material Science Laboratory. A highly monochromatic, planar, and partially polarized beam out of the first crystal (GaAs(100) is used) is incident onto the sample (i.e. the second crystal) through a Bragg angle for a certain diffraction. The reflecting power is defined as the intensity ratio at the sample surface of the diffracted beam to the incident beam.

In the rocking curve, the angular shift in reflection peaks is caused by the misorientation and the deviation of the lattice parameter from its reference value, i.e., deformation-induced strains; while both the thickness of a strained layer and the change of the structure factor induced by random displacement of atoms from the original lattice sites, i.e. lattice damage and defects, cause a decrease in the integrated intensity of Bragg peak as well as a broadening of the peak width. The rocking curve from a sample with a uniformly strained layer on a relatively thick (approximately unstrained) substrate has a well defined zero order peak separated from the substrate Bragg peak. A series of small peaks of decreasing amplitude are formed on either side of the zero peak when the crystal layers are of good quality. When the normal to the sample surface lies in the diffraction plane defined by the incident and diffracted beams, the angular separation of a misoriented layer is related to the strains by[21,22]

$$-\Delta\theta_0 = -(\theta - \theta_B) = k_1\varepsilon^{\perp} + k_2\varepsilon^{\parallel} \pm \xi_\phi, \tag{2.1}$$

where

$$k_1 = cos^2\psi tan\theta_B \pm sin\psi cos\psi, \tag{2.2}$$

and

$$k_2 = sin^2\psi tan\theta_B \mp sin\psi cos\psi. \tag{2.3}$$

ψ = angle between the diffracting plane and the crystal surface.

$\theta_B =$ Bragg angle of the substrate.

$\varepsilon^{\perp} =$ strain normal to the crystal surface relative to the substrate.

$\varepsilon^{\|} =$ strain parallel to the crystal surface relative to the substrate.

$\xi_\phi =$ component of the misorintation of the layer with respect to the substrate in the diffraction plane.

The upper sign in equations is used when the angle of incidence of x-rays is $\theta_B - \psi$ from the surface, and the lower sign is used for $\theta_B + \psi$ incidence. The lattice damage and defects cause a decrease in the structure factor and the diffuse x-ray scattering. Commonly, the Debye-Waller factor is used for the structure factor correction. It is expressed in terms of the average atomic displacement by

$$F_H = F_H^0 exp[-\frac{8\pi^2 sin^2\theta_B}{\lambda^2} U^2] = F_H^0 e^{-w(U)}, \tag{2.5}$$

where the subscript H represents the Miller indices of the reflecting lattice plane, F_H^0 is the structure factor of an undamaged crystal, and U is the root mean square atomic displacement where a random Gaussian distribution is assumed.

In the quantitative analysis of x-ray rocking curves, the dynamical x-ray diffraction theory as well as kinematical theory would be used. The dynamical model properly accounts for normal absorption (photoelectric process and Compton scattering) and extinction (coherent scattering or diffraction) of wave fields in a crystalline medium. The kinematical theory is just an approximate model when the strained layer is thin and the absorption and extinction can be neglected. By comparing the experimental rocking curves of imperfect crystals with the theoretical curves, information about strain and damage distributions as well as the composition and structure of the crystal can be extracted with high sensitivity and precision.

In our experiment, the symmetric (400) diffraction XRCs were taken from (100) InP by using a Fe-Kα_1 beam. In this case, perpendicular lattice strain has been measured. Here, because $\xi_\phi = 0$ and $\psi = 0$, thus $k_2 = 0$ and $k_1 = tan\theta_B$. Then the perpendicular lattice strains in the sample can be extracted from the angular shift in the rocking curve, described by:

$$\varepsilon^{\perp} = -\Delta\theta_0/k_1 = -\Delta\theta/tan\theta_B \tag{2.6}$$

Asymmetric (333) diffraction measurements were taken to obtain the parallel lattice strain through:

$$\varepsilon^{\|} = -(\Delta\theta_0 + k_1\varepsilon^{\perp})/k_2 \tag{2.7}$$

In the plots, the small peak from the substrate contribution is centered at the zero point as a reference. The large peak away from the 0 degree angle is the reflection contribution from the radiation-induced strained surface layer and the buried amorphous-crystalline interfaces. In the analysis of these rocking curves, the dynamical theory has to be used because the radiation-induced strain layers are very thick (about 2 ~ 5μm) and the maximium reflecting power of the surface strained layer is much higher than that from the substrate.

4. Damage Depth Profiling by CRBS

Channeling measurement of crystalline materials with Rutherford backscattering spectroscopy (CRBS)[23,24] is a well-established analytical tool for profiling imperfections and damage in crystalline solids.

In our laboratory, the channeling RBS experiments were performed using the EN-tandem accelerator. As an implanted layer is deeply buried (in a few μm), a high energy $^4He^+$ beam is required (3.5 MeV was used). The 400-keV $^4He^+$ beam is first generated by a JN-injector (a 1-MV Van de Graaff accelerator), then neutralized by passing through a differentially pumped canal filled with helium gas. The neutralized beam then enters into EN-Tandem accelerator and coasts through the first acceleration stage. Following charge exchange by gas stripping, the positively charged beam is re-accelerated to the energy required. Finally, 3.5 MeV $^4He^+$ ions are selected by analyzing magnet and focused to a spot of 2 mm in diameter on the target surface. Crystal channelling alignment was carried out with a goniometer, which can tilt the sample with respect to the incident beam direction and rotate the sample in the plane normal to the beam direction.

During channeling measurements, the samples were aligned along the surface normal axis direction, and backscattered particles were detected by a solid detector sitting at a lab angle of 165°. The random spectra were obtained by tilting the sample about $5 \sim 7$ degrees and rotating the sample continuously.

5. Structural Characterization by XTEM

Transmission electron microscopy (TEM) is an extremely interesting technique for crystalline structure studies[25,26]. When a parallel, monochromatic, and high energetic (a few hundred keV) electron beam is incident on a very thin specimen, the transmitted beam and diffracted beam as well as other secondary products (x-rays, Auger electrons, and scattered electrons) carry the information about the structure, imperfection, and composition in the specimen with a spatial resolution of a few angstroms. The most important advantage of TEM in material science is its ability to provide almost all the data needed to characterize completely the microstructure of materials. Cross sectional TEM (XTEM) has been used in this study to characterize MeV-ion-implanted layers and radiation-induced defects in the surface layers of implanted samples.

The cross-sectional specimens of both as-implanted and subsequently annealed samples were prepared through a standard procedure[27]. This was, however, difficult in this case because the InP crystals, especially the implanted samples, are much more fragile than those of Si and GaAs. The samples to be analyzed were first cut along the (110) direction into 1×3 mm^2 pieces, then two pieces were glued together in a face to face configuration with epoxy (M-Bond 60). After being cured in a heater at 100°C for 1 hour, the specimen was first mechanically thinned down to a few tens of μm thick, polished with 1 μm sized diamond paste, and then dimpled down to a few thousand angstroms thick in the center part. The specimen was finally thinned by ion milling with 5 keV ions to obtain a very thin region (electron transparency) for observation. Reactive iodine ion etching[28] has to be used because Ar ion milling causes preferential sputtering of phosphorus, leaving minute metallic indium islands on the sample surface. The specimen is also cooled down to LN_2 temperature during the milling process in order to minimize milling artifacts and avoid *in situ* annealing of the amorphous layer at ambient temperature.

The XTEM observation was conducted using the Caltech Material Research Group's Phillips Model EM430 TEM. The machine was operated at 300 kV. Bright field imaging was used to obtain a cross section view of the implanted layer. In the micrograph, the implanted layer and defect clusters in the sample shallow surface were shown in a different contrast with respect to the perfect crystalline substrate. The diffraction patterns were taken to identify the specimen orientation, crystalline quality, and defect spatial location. The fine features of the structure changes in the specimen have been studied by high resolution lattice imaging. The observation was normally taken in a $< 110 >$ direction plane at a magnification of 5×10^5. In this case, the lattice structure has been shown at the atomic scale, and the lattice spacing of 3.4 Å from the $\{111\}$ plane is clearly visible.

2.3. Distribution of MeV Implanted Atoms in InP

Depth profiling with the NRRA method with the reaction of $^{15}N(p, \alpha\gamma)^{12}C$ has experimentally established the distribution of implanted atoms in the ^{15}N-ion-implanted samples. The measured depth profiles are shown in Figure 2.4. As expected, the profiles show Gaussian-like distributions of ^{15}N implanted in InP with a slight asymmetry tail extending towards the surface. The nitrogen peak concentration reaches a level of 5×10^{20} atoms/cm^3. In the figure the calculated Gaussian

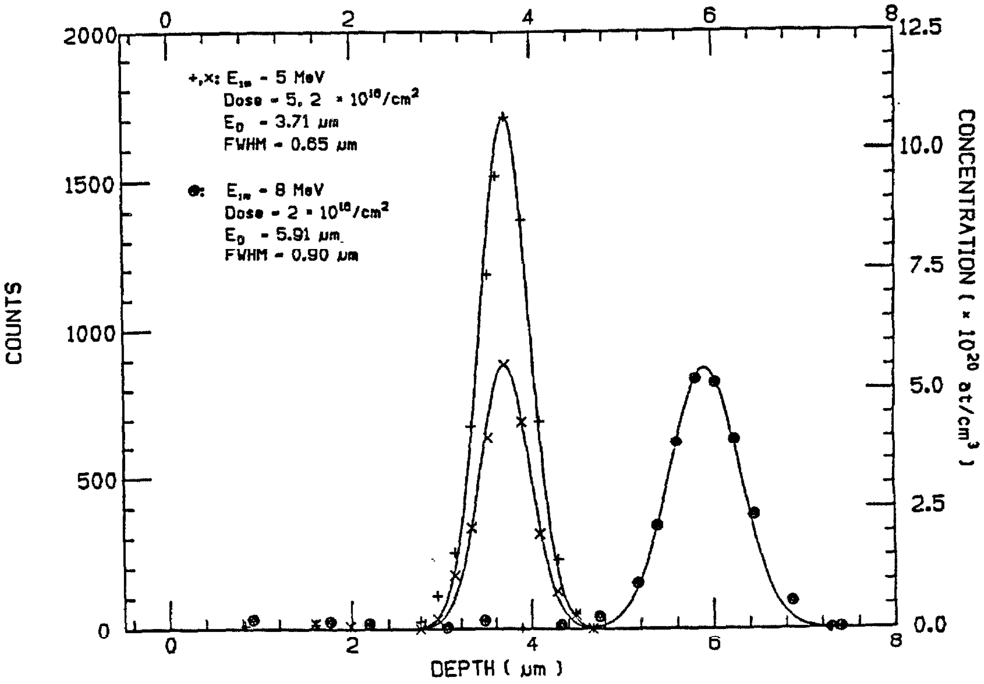

Figure 2.4 Depth profiles of ^{15}N by NRRA in the InP crystals implanted with 5 MeV ^{15}N to doses of 2x10^{16}/cm^2 (x points) and 5x10^{16}/cm^2 (+ points). The Gaussian-like distributions were found with a depth centered at 3.71 μm and a width of 0.65 μm and were independent of dose. The solid curves are calculated from Gaussian function with the parameters listed. The profile with o points is taken from the sample implanted with 8 MeV ^{15}N, illustrating the energy dependence of the depth range and width.

function curves (solid lines) are plotted. The depths of these peaks mark the average depth range of the 5 MeV ^{15}N ions in the InP single crystal. It shows that the implant distribution has a peak centered at 3.71 μm, which is dose-independent. The measured peak width (FWHM) is shown to be 0.65 μm. Considering the energy straggling of MeV protons in InP, which is estimated through the Bohr formula[29], incident beam spreading, and other instrumental broadening effects, the total broadening would be less than 5 keV (~0.2 μm) at a depth of 4 μm in InP. Thus, the real width of the implant distribution is about 0.64 μm. Considering the experimental uncertainties, these data are consistent with simulation by the TRIM code[30], which predicts the mean range to be 3.81 μm with a standard deviation

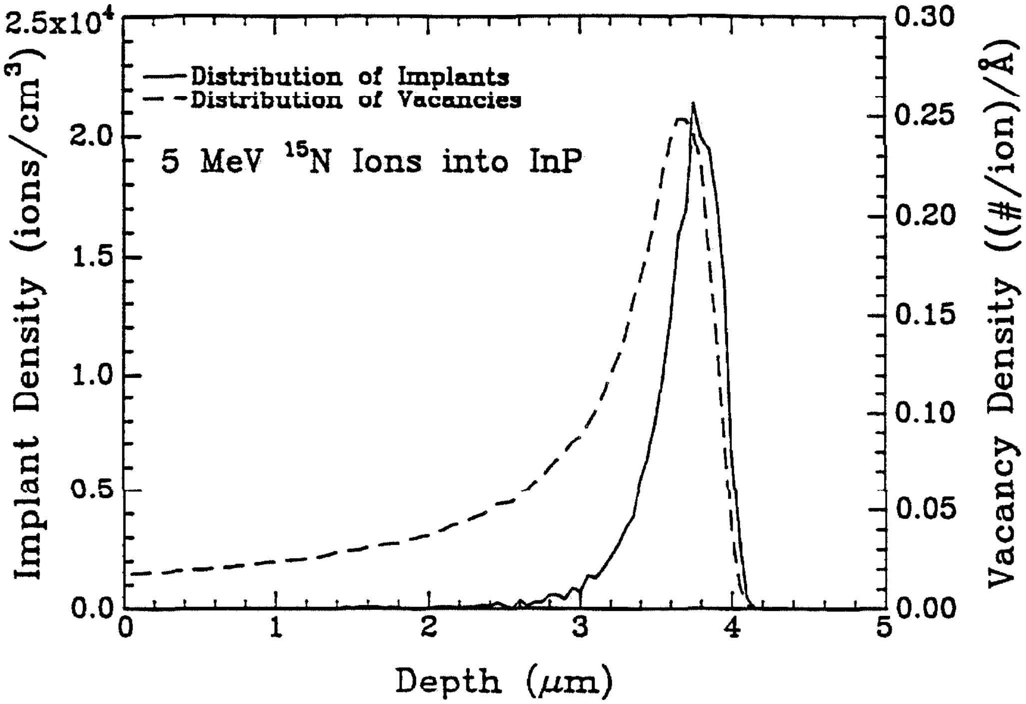

Figure 2.5 Ion distribution and damage profile of 5 MeV nitrogen-15 ions in InP, calculated by the TRIM code.

of 0.32 μm (FWHM = 2.35 × 0.32 = 0.752 μm) for 5-MeV-^{15}N-ions in InP (see Fig. 2.5). In addition, a profile from the sample implanted with 8 MeV ^{15}N is also presented in Fig. 2.4, illustrating the energy dependence of the depth range and the distribution width of the implanted ^{15}N in InP.

2.4. High Resistivity Produced by Nitrogen in n-Type InP Cystals

A major effort of our investigation is to produce deeply buried insulating layers in InP crystals by MeV ion implantation. The IVC measurement has given clear evidence that the implantation of MeV nitrogen ions plus subsequent thermal annealing can generate a deep buried layer with a resistivity up to about 10^6 ohm-cm in n-type InP crystals. This layer exhibits high thermal stability and reproducibility over a dose range $5 \times 10^{14} - 1 \times 10^{16}/\text{cm}^2$.

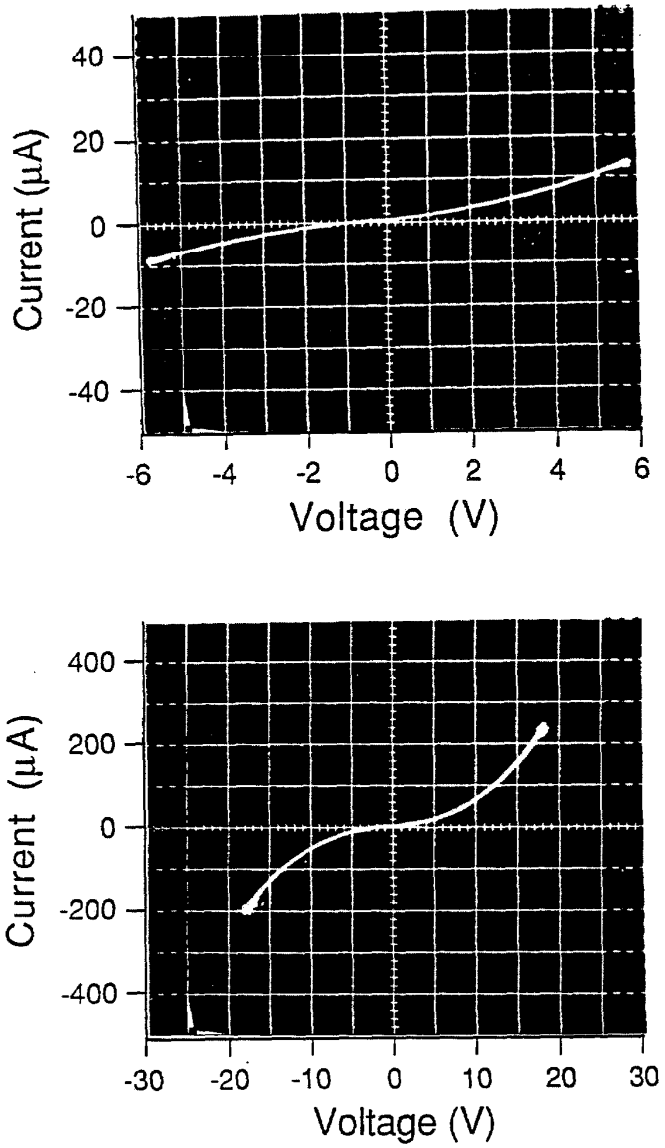

Figure 2.6 Typical I-V curve measured in a front-to-back mode. The sample was implanted with 5 MeV nitrogen ions at a dose of $5 \times 10^{15}/\text{cm}^2$ and annealed at 500°C for 20 min. a). measured with a small bias, a zero bias resistivity of about 10^6 ohm-cm is obtained. b). with a larger bias, which shows that the high resistivity is maintained, with a beakdown voltage greater than 20 volts.

Typical I-V characteristic curves of an implanted sample are illustrated in Fig. 2.6. This sample was implanted with 5 MeV nitrogen ion at a dose of $5 \times 10^{15}/\mathrm{cm}^2$ and annealed subsequently at 500°C for 20 min. The curve shows a nonlinear relation between the current and the bias voltage, which is nearly symmetrical for forward and reverse bias on the sample. The curve in Fig. 2.6a was taken with a relatively low bias, where the slope of the curve gives a resistance of about 10^6 ohms at the zero bias point. With a contact dot area, $A = 150\times150\ \mu\mathrm{m}^2$, and a width of the buried implanted layer, $W_i = 1 \sim 2\mu\mathrm{m}$, as observed by XTEM, the corresponding resistivity is deduced to be $\sim 10^6$ ohm-cm. From the curve shown in Fig. 2.6b one can clearly see that the highly resistive layer can sustain a high bias, the breakdown voltage being greater than 20 volts. The effect of dose-dependence on such nitrogen-implantation-induced electrical isolation was investigated with a sequence of samples implanted at doses from $1 \times 10^{14}/\mathrm{cm}^2$ to $1 \times 10^{16}/\mathrm{cm}^2$. It has been found that the high resistance behavior appears on samples implanted with doses greater than $5\times10^{14}/\mathrm{cm}^2$, and the resistivity increases slightly with increasing implant dose. This can be correlated with the expansion of the buried layer width as the implant dose increases, as shown below by the XTEM results (see Section 2.6). Thus, the estimated average resistivity of buried semi-insulating layers at different implant doses is roughly unchanged after a uniform buried layer is formed.

The thermal annealing effect and thermal stability of the resistivity change have been studied with the samples treated under different thermal conditions. The result is presented in Fig. 2.7. In Fig. 2.7a the samples were implanted with a dose of $5 \times 10^{14}/\mathrm{cm}^2$. Curve 1 is taken from the as-implanted sample with non-alloyed metal contacts, showing weak Schottky-junction-type characteristics with a resistance of only a few kΩ. Curve 2 results from an implanted sample after alloying at 380°C for 20 sec, where a significant thermal annealing effect has been observed. The desired characteristic of high resistivity due to nitrogen implantation is obtained after annealing the samples at high temperature (at 500°C for 20 min.)

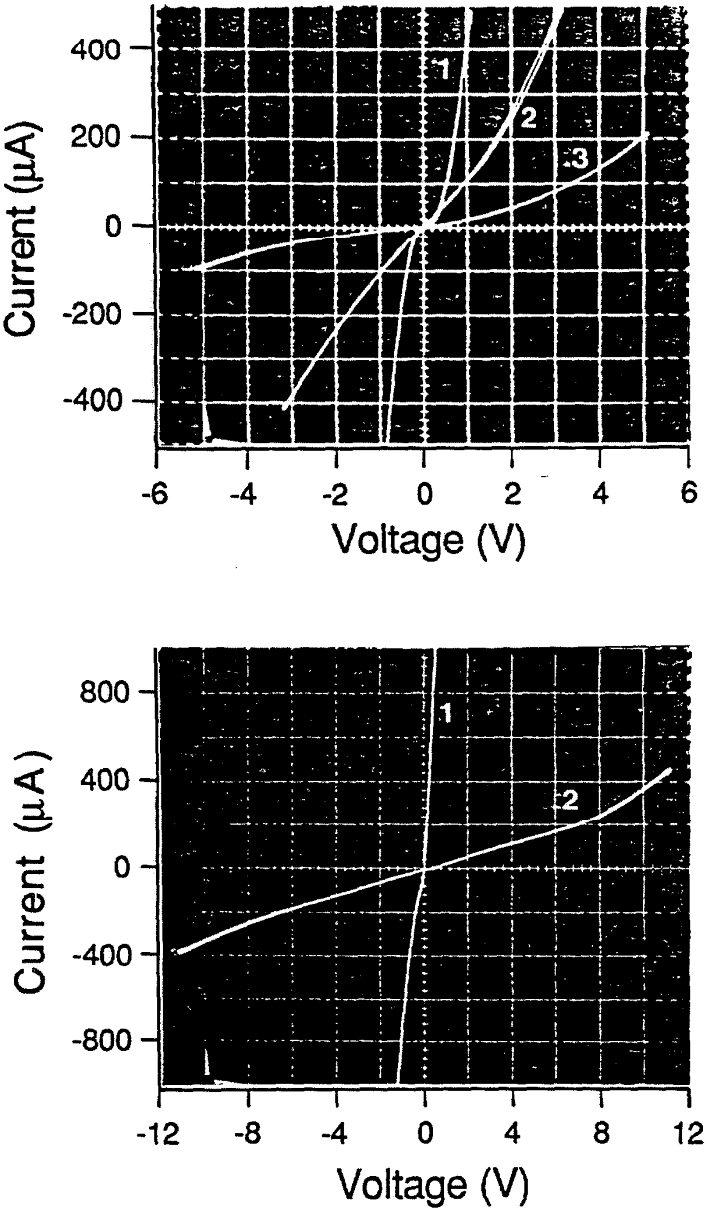

Figure 2.7 I-V characteristic curves of the implanted samples which have been subsequently treated in different thermal annealing conditions. a). the sample implanted with a dose of $5 \times 10^{14}/\mathrm{cm}^2$, (1) as-implanted, (2) annealed at 380°C for 20 sec, (3) annealed at 500°C for 20 min; b). the samples were annealed at 650°C for 1 hour, (1) implanted with a dose of $1 \times 10^{14}/\mathrm{cm}^2$, and (2) of $1 \times 10^{16}/\mathrm{cm}^2$.

as shown by Curve 3 in Fig. 2.7a. In order to investigate the stability of the nitrogen-implantation-induced high resistivity after higher temperature and long period heating, which is the required environment of LPE crystal regrowth for further device fabrication, two samples implanted with doses of $1 \times 10^{14}/\mathrm{cm}^2$ and $1 \times 10^{16}/\mathrm{cm}^2$, respectively, were annealed in an LPE furnace at 650°C for 1 hour. The I-V curves, as illustrated in Fig. 2.7b, show that after such a high-temperature and long-period annealing process the low dose implanted sample has become almost conducting, behaving like an unimplanted sample; while the high dose implanted one remains insulating with linear characteristics. The correlation of these features with the lattice damage and implanted layers can be interpreted by CRBS and XTEM studies of these samples, which will be presented in the next section.

A full understanding of the mechanism of ion implantation induced electrical isolation in III-V compound semiconductors is complicated. It is believed that the effect of electrical isolation in light ion (proton or deuteron) bombarded samples[5,6,13,14] is mainly due to radiation-induced crystal defects because the resistivity in the as-implanted layers increases with the implant dose, and decreases or even disappears after annealing at temperatures over 600°C. In oxygen implanted GaAs materials[7,8], it is found that oxygen-related deep electron traps are responsible for semi-insulation generation. In Fe-implanted n-type InP[15], chemical doping is the dominant effect, where the implanted Fe acts as a simple deep acceptor near the middle of the energy band gap, and compensation of free carriers drives the Fermi level to the intrinsic Fermi level position. In the case of nitrogen implantation into InP, the process seems much more complex. Evidence from the experimental results presented above suggests that the effect of high resistivity in nitrogen implanted InP layers is not directly due to radiation induced crystal damage, but rather to a highly disordered structure in the implanted layer, which is formed after thermal annealing. Such a structure would greatly reduce the mobilities of charge carriers. However, another possible mechanism is that the high resistivity behavior of the nitrogen implanted InP is not solely due to the disordered regrowth structure but also requires nitrogen to be present. One experiment of MeV oxygen ion implantation into n-type InP crystals was performed earlier[31]. The IVC measurement of the sample implanted at a dose 1 $\times 10^{15}/\mathrm{cm}^2$ showed moderate resistivity after annealing at 450°C for 15 min, but it decreased dramatically after annealing at 650°C for 1 hour. This is in contrast to the cases of oxygen in GaAs and nitrogen in InP because oxygen is a typical shallow donor in these compounds, which was also observed early in GaP system [32]. Nitrogen is known to be a different type of impurity in III-V compounds than is commonly used in semiconductors. From the point of view of chemical bonding, it is called an isoelectrical impurity because it comes from column V of the periodic table and therefore has five valence electrons, as does the phosphorous that it replaces in crystal lattices. As a consequence, nitrogen introduces no charges if it replaces phosphorous in the crystal lattice. However, unlike conventional isoelectrical impurities, nitrogen may provide deep electronic trap centers in the column V element-based compound materials. From the point of view of electrical band spectroscopy, nitrogen is an isovalent atom for III-V compounds. Such impurities may produce bound states in the forbidden gap, binding a hole (or an electron). Both experimental data and theoretical prediction have suggested that this effect is very closely associated with the difference of electronegativities between the isovalent atom and its substituted atom[32,33]. It may bind a hole (electron) only if its electronegativity is smaller (larger) than that of the host atom it replaces. It is also found that only very large atoms or very small atoms produce bound states (isoelectronic traps). Typical examples have been observed in GaP[33], where Bi (or N) replaces P, giving rise to a weakly bound electron (or hole) and acting as a donor (acceptor). A similar effect would be expected in InP with the nitrogen isovalent impurity.

The electronegativity as a dimensionless constant is a measure of the capability of an atom to attract electrons to itself when forming a compound. Its variation depends strongly on the orbital states of valence electrons as well as the core electron configurations that determine the valence radial size of the atom. The elemental electronegativity of III-IV and V column atoms as well as their tetrahedral covalent radii are listed in Table 2.1, taken from Ref. 34. One finds that

Table 2.1. Electronegativities (in the first row) and covalent radii (in the second row) of nontransition elements in tetrahedral coordinated environments

Li	Be	B	C	N	O	F
1.00	1.50	2.00	2.50	3.00	3.50	4.00
	1.06	0.88	0.77	0.70	0.66	0.64
Na	Mg	Al	Si	P	S	Cl
0.72	0.95	1.18	1.41	1.64	1.87	2.10
	1.40	1.26	1.17	1.10	1.04	0.99
Cu	Zn	Ga	Ge	As	Se	Br
0.79	0.91	1.13	1.35	1.57	1.79	2.01
1.35	1.31	1.26	1.22	1.18	1.14	1.11
Ag	Cd	In	Sn	Sb	Te	I
0.57	0.83	0.99	1.15	1.31	1.47	1.63
1.52	1.48	1.44	1.40	1.36	1.32	1.28
Au	Hg	Tl	Pb	Bi		
0.64	0.79	0.94	1.09	1.24		
	1.48	1.47	1.46	1.45		

* The data were taken from Ref. 34.

the electronegativity of a nitrogen atom is much larger than that of other elements in the column V. When nitrogen substitutes for those column V elements in III-V compounds, the change of covalent bond length produces a lattice strain field. In turn, when the lattice relaxes, it produces an excess atomic pseudopotential that is short range but sufficiently strong. Thus, it attracts an extra valence electron to itself and becomes negatively charged. As a result, the Coulomb field of the negatively charged nitrogen atom can weakly bind a hole, and this hole can be ionized to make it available to carry current. One could imagine the additional electron as being very tightly bound to the nitrogen atom, while the additional hole circles around the impurity at a distance of several lattice constants. This makes nitrogen an isovalent acceptor in III-V compounds. In the case of nitrogen-ion-implanted InP, the implants induce the strain field in an as-implanted sample. After high temperature thermal annealing, the radiation-induced strain relaxes, and nitrogen occupies the phosphorous site in the host lattice and becomes ionized, thereby creating a deep acceptor acting as an electron trap. As a result, these electron traps compensate with the original dopants, reducing the electron carrier mobility and generating a high resistivity layer in the n-type InP substrate. This effect has also been demonstrated through carrier compensation in n-type GaAs resulting from nitrogen implantation[35], where it has been concluded that the observed compensation is due to a deep acceptor-like center associated with the nitrogen. We would expect that a similar effect may be present in other III-V compounds with nitrogen ion implantation as isovalent doping. Detailed calculation of the change of the pseudopotential band-structure induced by isovalent impurities[36] would be of great help to us for understanding this phenomenon, as well as extending this method to other systems.

2.5. Profiles of Ion-Radiation-Induced Lattice Strain

Radiation-induced lattice strain is an important and interesting subject because it is an indication of the structural property of the implanted layer. The lattice strain measurements with the XRC technique can also provide us with information to understand the phenomenon of radation damage production and amorphization in crystalline materials by MeV ion implantation. The XRC studies of ion-implanted Si, Ge, and several III-V compound semiconductors have been reported earlier[22,37,38]. The results of MeV ion implanted InP are presented here.

The XRCs shown in Figure 2.8 illustrate the build-up of radiation-induced strain in InP and GaAs single crystals, which have been implanted by 15 MeV chlorine ions at several doses. The postive angular shift of these strain peaks in InP samples (in the left-hand plot) indicates lattice spacing contraction has occurred in the plane parallel to the surface. It was also noticed that similar behaviour presented in (110) and (111) oriented InP crystals[39]. This is most suprising, as the result is opposite to the case of GaAs(100) (in the right-hand plot in Fig 2.8)

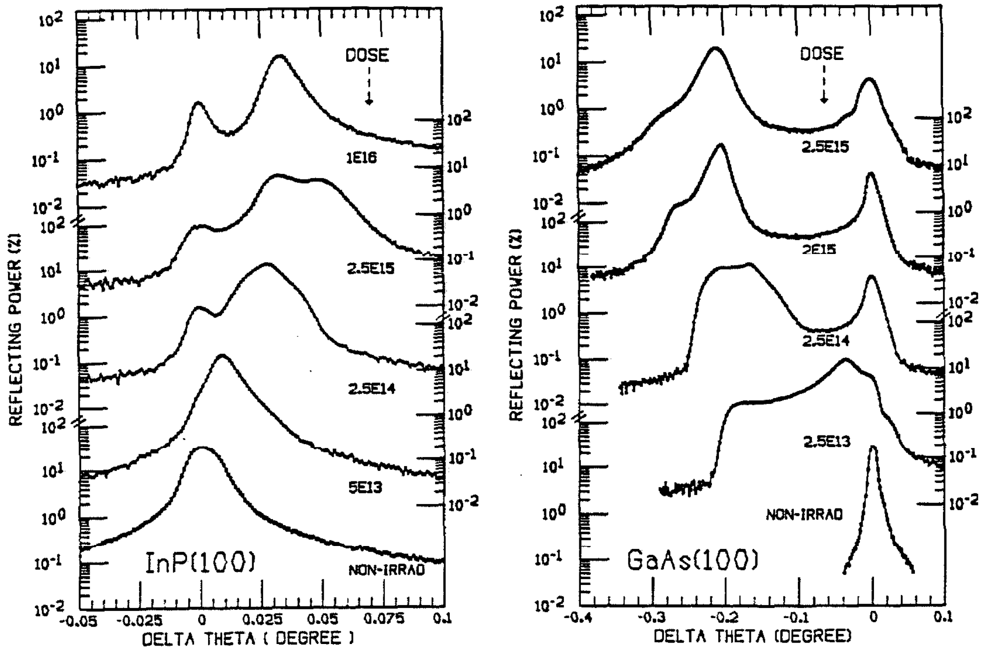

Figure 2.8 X-ray rocking curves of the 15 MeV-^{35}Cl-ion-implanted InP and GaAs from (400) symmetrical diffraction with respect to the substrate. The radiation-induced strain and the strain saturation are shown. See details in the text.

and other III-V compounds that have been studied in detail by Wie et al.[22]. The evolution of the lattice strain field as a function of the implant dose for 5 MeV nitrogen ion implanted samples is presented in Figure 2.9. It has been found that perpendicular lattice strain has been gradually induced in the surface and implanted layer (unamorphized) inside the crystal, with a saturation at the average perpendicular strain level of -0.060±0.002% when the implant dose is greater than 2×10^{15} ions/cm^2. This value is equal for the cases of 15-MeV-Cl[22] and 8-MeV-O[31] ion implanted InP (100) samples. Comparing with the results by CRBS and XTEM that will be presented in the next section, it can be concluded that due to the ion-induced lattice disordering and defect production, the Bragg diffraction angle broadening and lattice-strain production reveal the dose-dependent nature of the crystal damage and lattice parameter variation induced by implants and defects

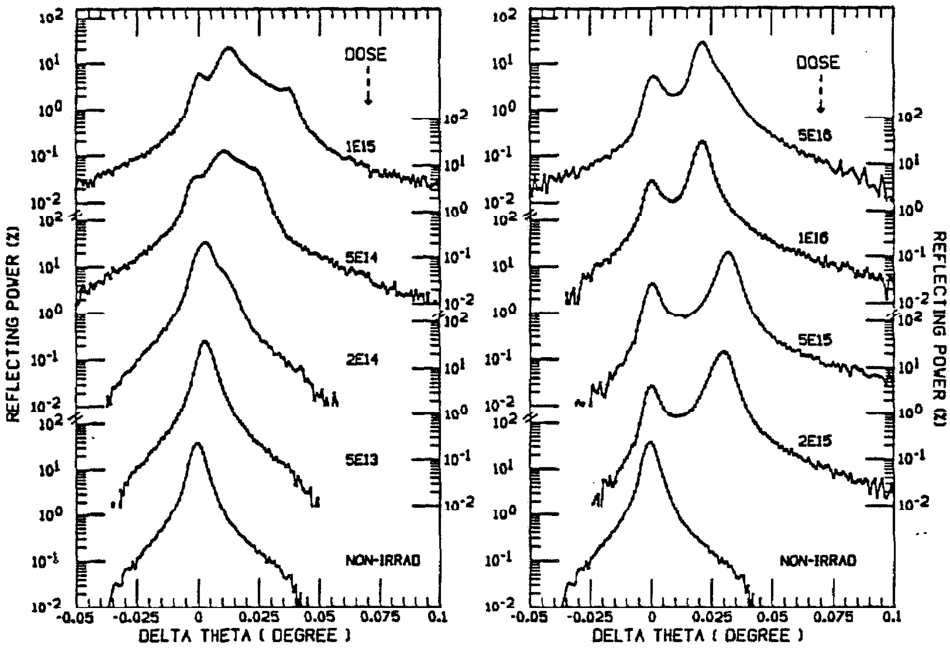

Figure 2.9 X-ray rocking curves of the 5MeV-^{15}N-ion-implanted InP from (400) symmetrical diffraction with respect to the InP substrate. The evolution of radiation-induced strain is shown. See details in the text.

during the implantation, and that the strain saturation indicates the occurrence of implantation-induced amorphization. In addition, one noticeable feature that can be clearly observed from the XRCs of those samples implanted with very high doses, is that the levels of saturated strain have decreased when the dose is over $1\times10^{16}/\text{cm}^2$. At those doses, as shown by CRBS and XTEM, the implantation-induced amorphous layer has already approached the top surface. Thus, the decrease might be a sign that in-situ annealing and recrystallization have occurred inside the sample during implantation. Asymmetric XRCs from implanted samples show no evidence in the build-up of parallel strain. A possible reason may be the coherent coupling of the surface layer to the substrate lattice and stronger constraint in the lateral dimension than in the vertical direction. Detailed damage and strain profiles can be extracted from the these XRCs by theoretical simulation and fitting with the x-ray dynamical diffraction theory[22]. The calculated results obtained for

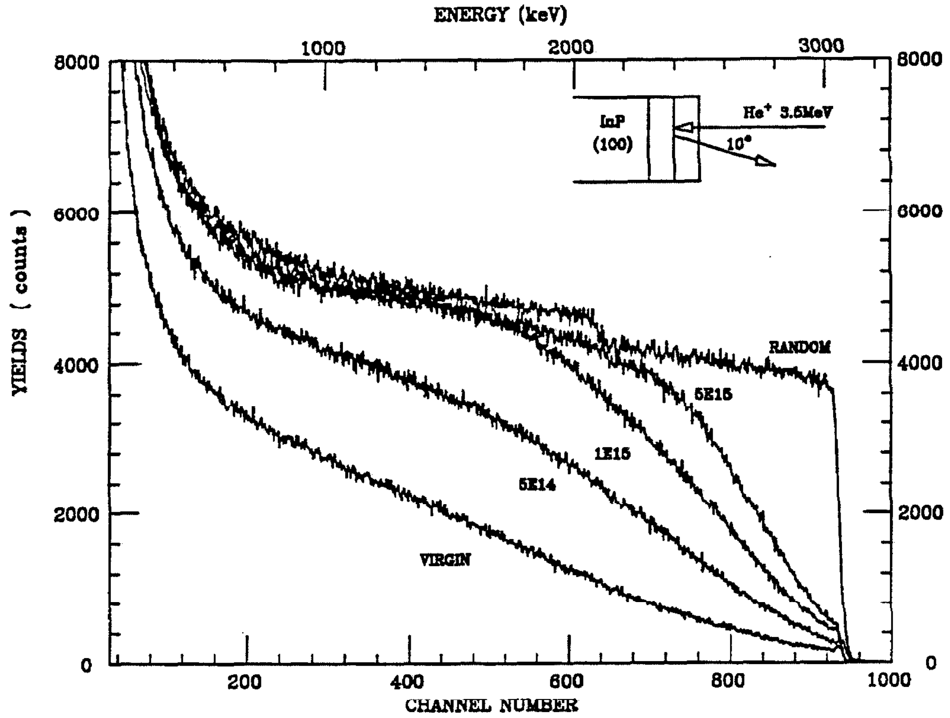

Figure 2.10 Channeling RBS spectra of InP crystals as-implanted with 5 MeV ^{15}N at room temperature with a sequence of doses as marked beside the curves.

InP are very similar to those for GaAs reported by Wie[22], except for the strain sign inversion.

The mechanisms on the radiation induced lattice strain in semiconductors will be discussed in detail in Chapter 4.

2.6. MeV Ion-Implantation-Induced Lattice Damage and Structural Phase Transitions

The processes of lattice damage and crystalline-to-amorphous (c-a) transition in InP by MeV ion implantation have been clearly revealed by the combination of CRBS and XTEM measurements.

The typical resulting spectra from the as-implanted samples are illustrated in

Figure 2.10. The lowest curve is a channeled RBS spectrum from the non-irradiated sample, showing a minimum dechanneling yield from the residual defects in the virgin crystal. The top curve is the random spectrum, indicating a backscattering yield from an amorphous-like InP. The curves in the middle are taken from the implanted sample with different doses as marked beside the curves. As shown in the spectra, the ^{4}He particles suffer more and more de-channeling in the irradiated sample as they go deeper inside, which illustrates the depth distributions of the damage in the InP crystals caused through the implantation. It is clearly observed that as the implant dose increases, the dechanneling yield dramatically increases. At a certain depth inside the samples it saturates at about 100% when the dose is over $1 \times 10^{15}/\mathrm{cm}^2$. This region gradually extends towards the sample surface with higher doses; this saturation is an indication of the formation of a buried amorphous layer established by the XTEM micrograph. Note that the spectrum from the as-implanted sample at the dose of $1{\times}10^{16}/\mathrm{cm}^2$ is not shown here, as it looks almost the same as the random spectrum except for a slight drop for a few hundred Å near the surface. This implies that at this dose an implantation-induced buried amorphous layer has formed from the end of the ion range to a shallow depth near the surface. These have been clearly observed through the XTEM analysis.

Micrographs in Figure 2.11 show the typical bright field XTEM views of the entire implanted region of a set of InP samples that were implanted with nitrogen ions at different doses. The sample surface lies on the left-hand side in the micrographs, with the arrows indicating the incident implant beam direction, which is normal to the sample surfaces. The region with irregular dark spots is found to be heavily damaged with a high density of point defect clusters induced by the ion implantation. The contrast-featureless band in the micrographs is the buried amorphous layer formed during implantation. Selected area diffraction patterns taken from those regions allow us to determine the structural phase, whether they are in the amorphous form or just heavily-damaged crystalline materials. In Fig. 2.11a, the sample was implanted with a dose of $5 \times 10^{14}/\mathrm{cm}^2$, where one can see

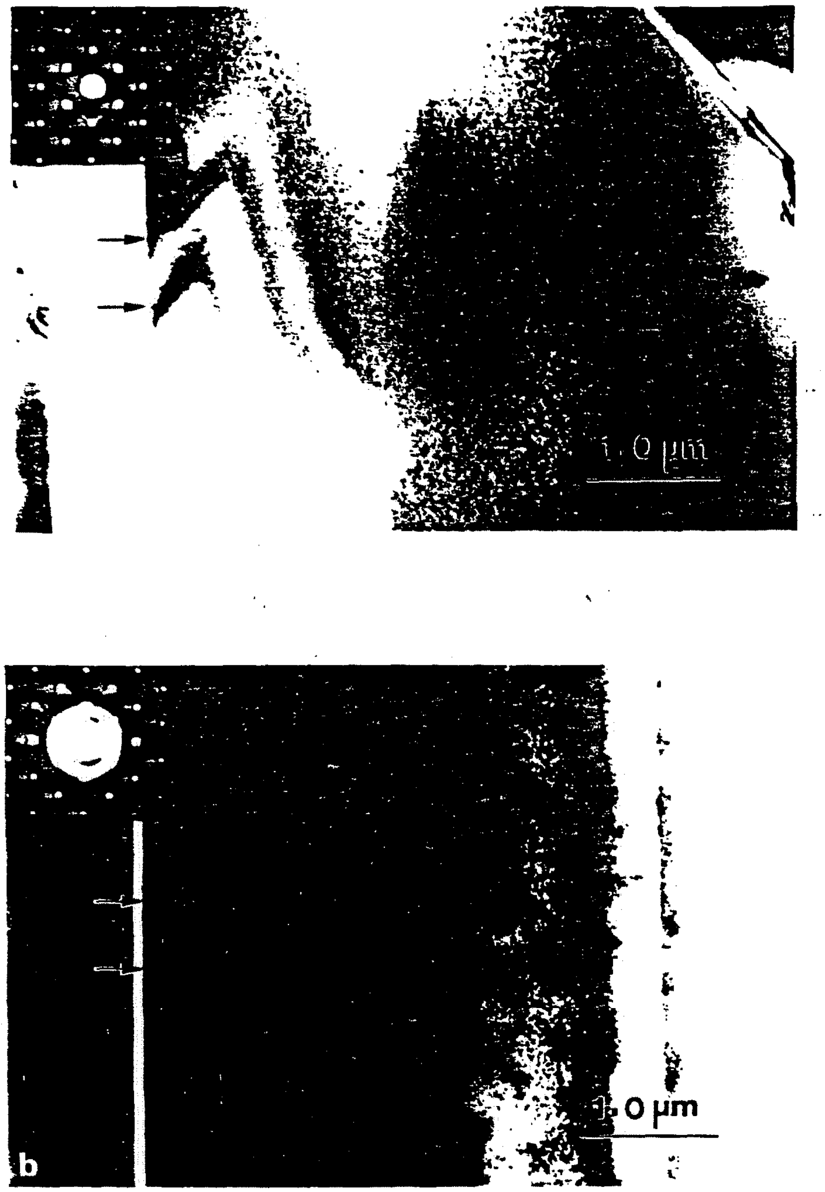

Figure 2.11 XTEM micrographs of 5 MeV nitrogen ion as-implanted InP and $< 110 >$ diffraction patterns of the buried implanted layers. The samples were implanted with a dose of a) $5\times10^{14}/\text{cm}^2$, b) $1\times10^{15}/\text{cm}^2$, c) $2\times10^{15}/\text{cm}^2$, and d) $1\times10^{16}/\text{cm}^2$. The sample surface lies at the left-hand side, the arrow indicates the incident beam direction. See the text for details.

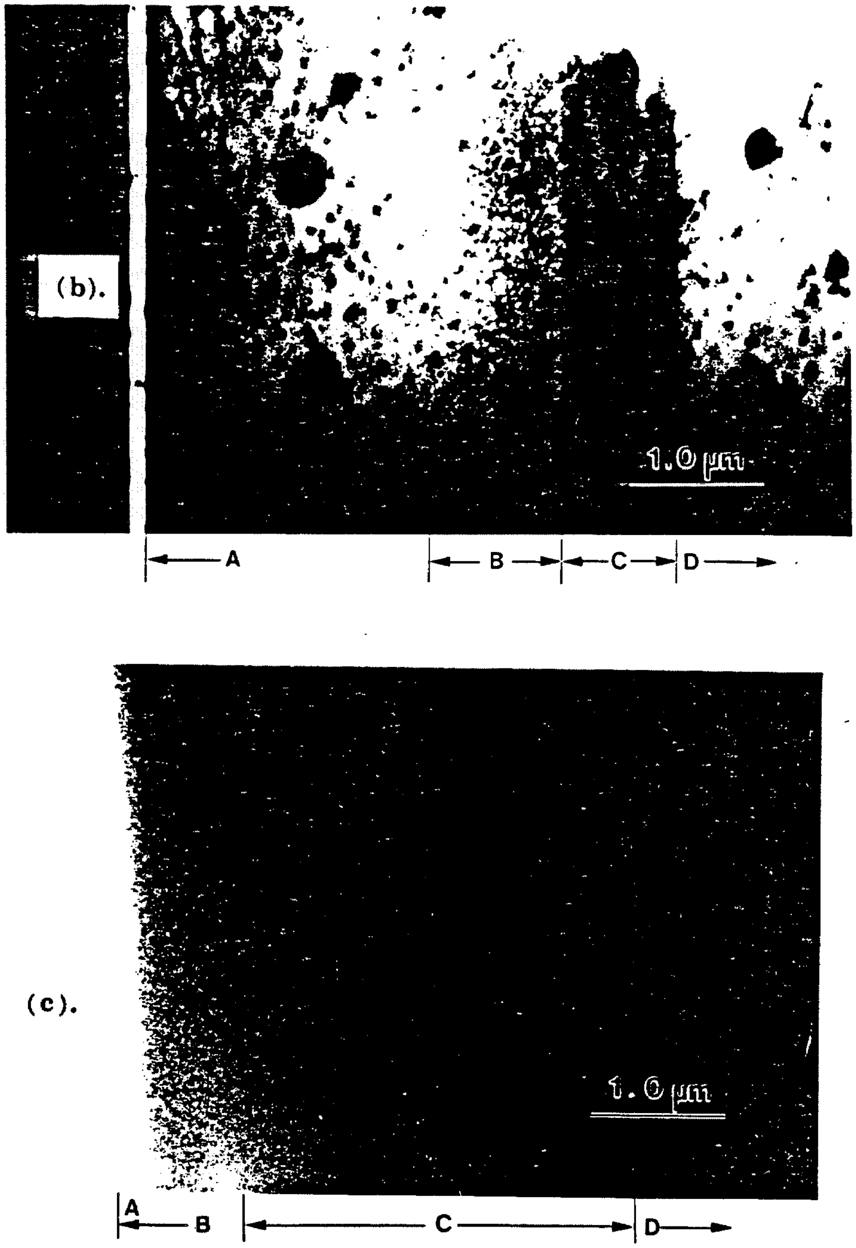

Figure 2.11 (continued)

only a heavily damaged region with a high density of point defects distributed in a gradient from the sample surface to the end of the ion range, around 4 μm deep. This follows a predicted pattern of damage shown in Fig. 2.5. The distribution of point defects in the damaged regions does not correlate directly with the implant depth distribution, but instead with the integrated ion energy loss due to nuclear stopping at each point. The diffraction pattern taken from this area shows its single crystalline structure. The streaks that appear indicate the presence of thin twins within {111} twinning planes. Presented in Fig. 2.11b is the sample implanted at a dose of $1 \times 10^{15}/\mathrm{cm}^2$. A buried continuous amorphous layer, appearing as a white band in the picture, has been created with the maximum depth at 4 μm. This amorphous structure has been identified by diffuse rings in the corresponding diffraction pattern. The maximum depth corresponds to the ion maximum range and is well defined statistically by the beam energy. Assuming that the concentration of damage-created defects increases linearly with the implant dose, then from the TRIM calculated damage profile as shown in Fig. 2.5 one can estimate that the critical defect density for the crystalline-to-amorphous transition is $10^{19}/\mathrm{cm}^3$. This is consistent with the NRRA implant profiles and the CRBS damage profiling data. Damaged regions appear on both sides of the amorphous band with a narrow defect-contained region preserved behind the amorphous layer and a widely spread region in front of the amorphous layer extending to the surface. XTEM micrographs of higher dose implanted samples are presented in Figs. 2.11c-d. They show that wider amorphous layers are created, about 1 μm in a $2\times10^{15}/\mathrm{cm}^2$ implanted sample (Fig. 2.111c) and 3 μm in a $1\times10^{16}/\mathrm{cm}^2$ implanted sample (Fig. 2.11d), with a heavily damaged top crystalline surface. In Fig. 2.11d, the micrograph contrast does not show very clearly the top damaged surface because this surface has also been highly disordered. However, this crystalline-amorphous layer interface becomes easily recognized after the sample is annealed at high temperature (see the micrograph in Fig. 2.16).

Through XTEM observation, it has been found that the critical dose for formation of a continuous buried amorphous layer is around $1\times10^{15}/\mathrm{cm}^2$ for nitrogen ion implanted InP; and the width of the amorphous layer broadens towards the sample surface as the implant dose increases. The implanted layer near the end of the ion range becomes amorphous due to direct heavy nuclear damage with a fixed maximum depth, independent of the implantation doses. The radiation-induced defects in the surface layer gradually accumulate until the density goes over a critical level at which the material transforms to the amorphous phase. This morphology has been shown by CRBS analysis for lattice damage profiling, and has also been deduced from the measurement of an implantation induced lattice strain profile with the x-ray rocking curve technique shown in the last section. It will be discussed in detail in Chapter 5.

A similar phenomenon is observed in chlorine ion implanted samples, where the critical dose for the crystalline-to-amorphous transition is a little lower ($5 \times 10^{14}/\mathrm{cm}^2$) than that for nitrogen ion implanted samples, which is consistent with the fact that heavier ions have higher efficiency for producing damage in the crystals. The correlation, extracted from XTEM measurements, between the width and the maximum depth of the buried amorphous layer and the implant dose in chlorine implanted InP samples is plotted in Fig. 2.12. It was found that the depth of the implanted layer is almost fixed at 6 μm, and is precisely determined by the ion energy. The width of the layer expands linearly with the logarithm of the implant dose, and approaches saturation when the dose is over $5 \times 10^{15}/\mathrm{cm}^2$, whereupon the formation of the amorphous state begins by relaxation of damaged crystalline matrix when the defect density reaches a critical value. However, it is noted that the relationship of the layer width to the implant dose is not uniquely controlled, and strongly depends on the implantation conditions, such as the beam flux and the substrate temperature.

The fine features of the structural transformation have been studied by HRTEM lattice imaging. HRTEM micrographs in Fig. 2.13 illustrate as-implanted samples from the regions near the interfaces. In a low dose implanted sample as

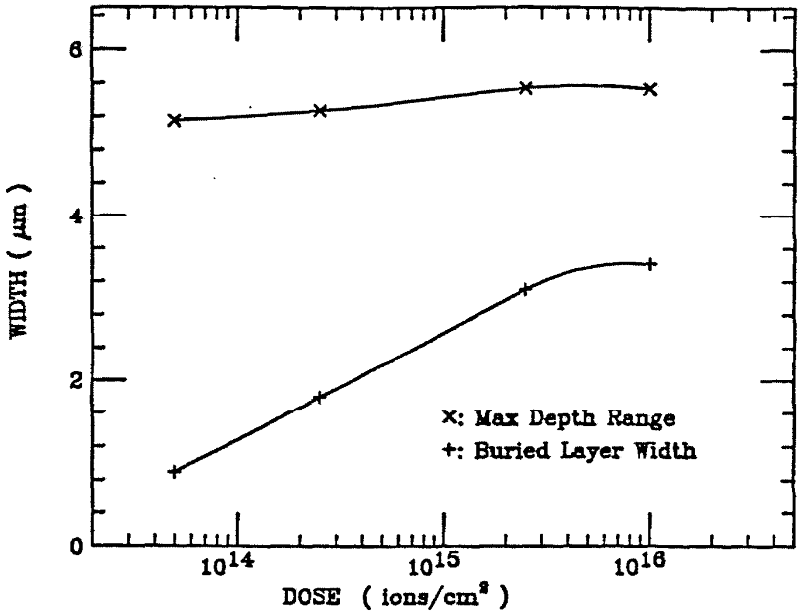

Figure 2.12 A plot of the width and the depth of the buried amorphous layer *versus* the implanted dose in 15 MeV Cl ion implanted InP(100) samples. The data are obtained from XTEM measurements.

shown in Fig.2.13a ($5\times10^{14}/cm^2$), only a high density of radiation-induced damage can be found. Most of the common defects in InP appear as point defect clusters, microtwins, stacking faults, and partial dislocations that lie in {111} planes. They may be associated with distributed implants but probably are due to channeled collision cascades, and determined by the binary nature of InP compound as will be discussed later. As the dose increases, the density of defects dramatically increases and the damage along ion tracks becomes more visible and more stable. As direct evidence, Figs. 2.13b-c present two HRTEM micrographs taken from the top and inner interfaces, respectively, of a sample implanted by Cl ions to a dose of $2.5\times10^{15}/cm^2$. In Fig. 2.13b, a great density of amorphous pockets is found to precipitate in the crystalline matrix. While in Fig. 2.13c, in addition to randomly distributed crystalline grains emerging in the implantation-induced amorphous region, a few individual amorphous clusters created along ion tracks due to the spike

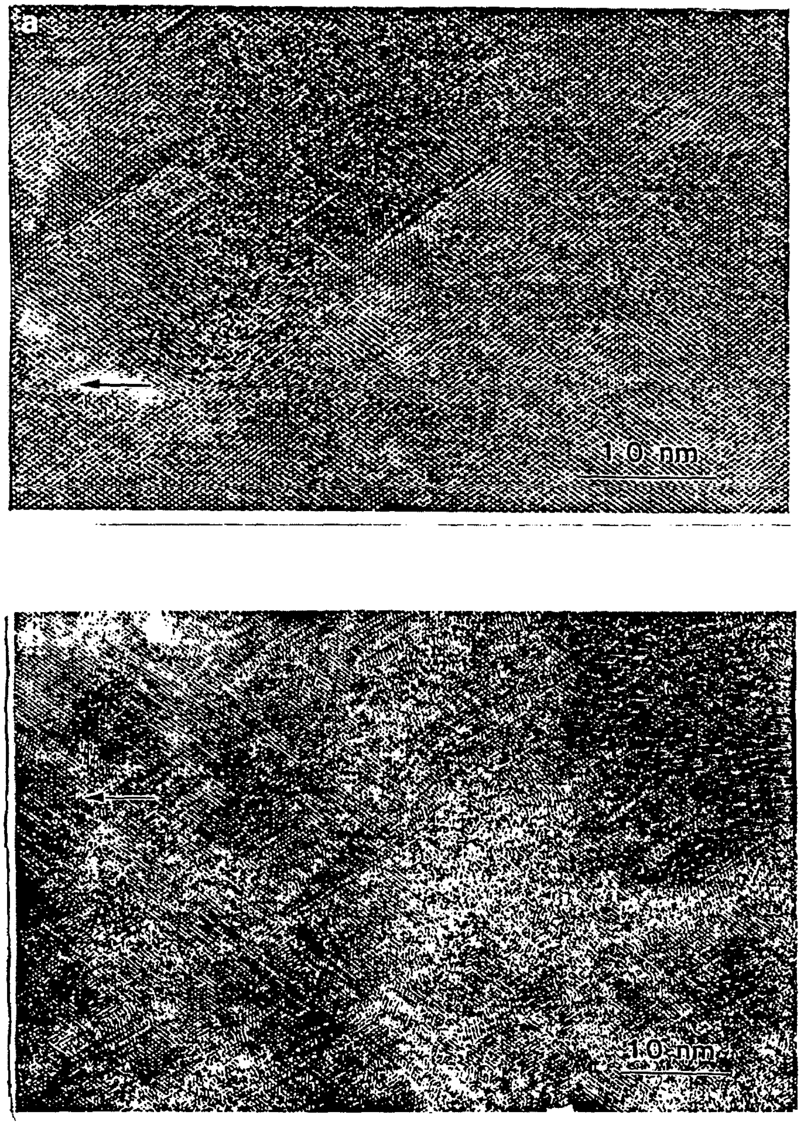

Figure 2.13 HRTEM micrographs of MeV ion as-implanted InP near interfaces, showing damage production and gradual crystalline-to-amorphous transition with increasing the implant dose. a) a dose of 1 $\times 10^{14} N/\mathrm{cm}^2$, in a heavily damaged area, a high density of lattice defects lying in $\{111\}$ planes; b) $2.5\times 10^{15} Cl/\mathrm{cm}^2$, around the top interface, an intimate mixture of individual amorphous and crystalline pockets;

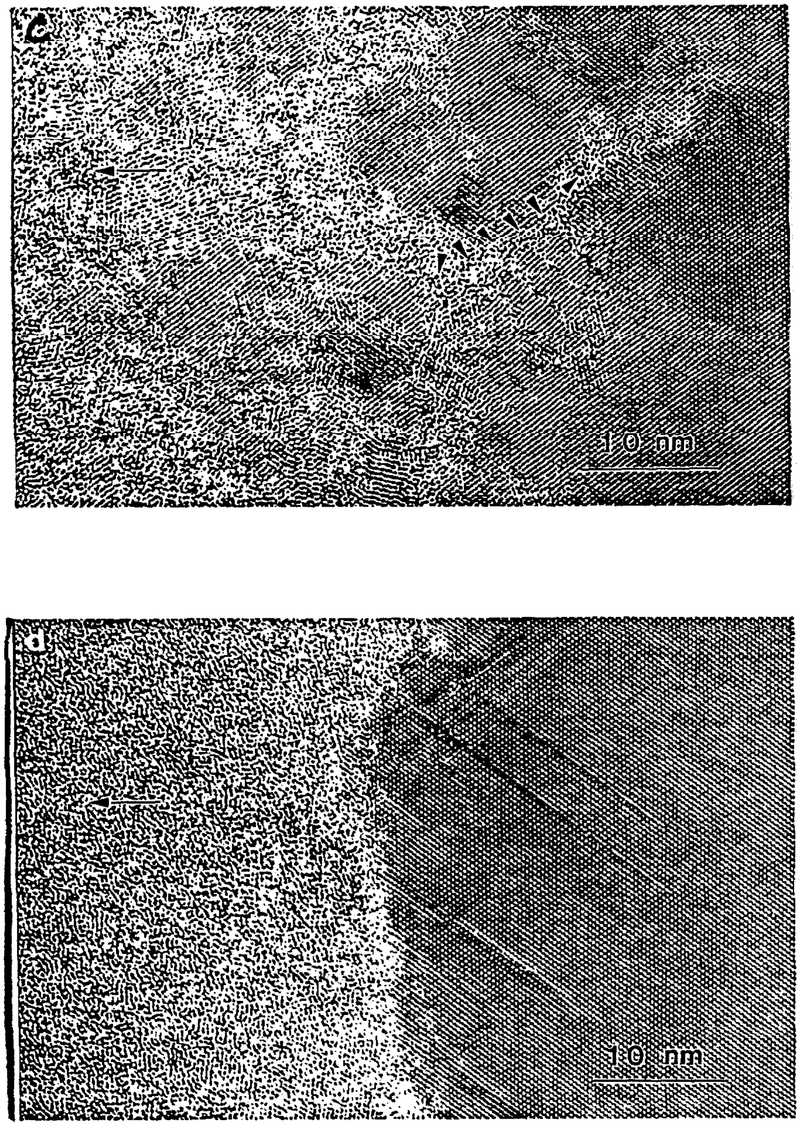

Figure 2.13 (continued) c) 2.5×$10^{15}$$Cl$/cm^2, around the inner interface, where the amorphous zone with crystalline inclusions, nuclear spike induced amorphous pockets in the ion tracks, and recoil nuclei tracks before the end of ion stopping points can be found, as indicated by small arrows; and d) 1 ×$10^{16}$$N^+$/cm^2, at the inner interface, sharp crystalline-to-amorphous transition boundary. (The arrow points to the sample surface.)

effect before the ions finally stop can be more clearly observed. They have a dimension of only a few lattice spacings wide and a few tens of angstroms long and are channneled along < 111 > directions. This may be visible evidence to explain why the defects lie most favoritely along < 111 >directions as shown in Fig. 2.13a. As the implant dose is increased, individual damage and amorphous zones spread and overlap to form a continuous amorphous layer, with a sharp crystalline-amorphous interface. This is clearly illustrated in Fig. 2.13d, where the sample was implanted with nitrogen ions at a dose of $1 \times 10^{16}/\mathrm{cm}^2$. The defects on the crystalline substrate side are thought to be due to channeling cascades and *in situ* annealing. It is important to notice that the boundaries between the buried layer and the substrate or the surface crystalline layer are sharp, which is different from what was observed on GaAs samples[40].

2.7. Annealing Behavior of Implanted Amorphous Layers and Lattice Damage

The study of the annealing behavior of implanted amorphous layer and surface lattice damage is also an important matter because it provides some additional information for understanding the properties of the implanted layer and the mechanisms of ion-induced damage and phase transition.

2.7.1. Room Temperature Annealing

First, the significant room temperature (RT) annealing effect has been observed when the implanted samples are stored in air at RT. Fig. 2.14 presents a set of XRCs taken at RT from a sample implanted by 2 MeV oxygen ions at 77K with a dose of $2\times10^{14}/\mathrm{cm}^2$. It shows clearly lattice strain relaxation at RT with evidence in XRCs through strain peak angular shift and reflecting power decreasing. Extracted from XRCs, evolution of average lattice strain at RT as a function of storage duration in air is plotted in Fig. 2.15. One sees that the average lattice strain relaxes nearly in an exponential way with the storage time, and gradually reaches a steady level.

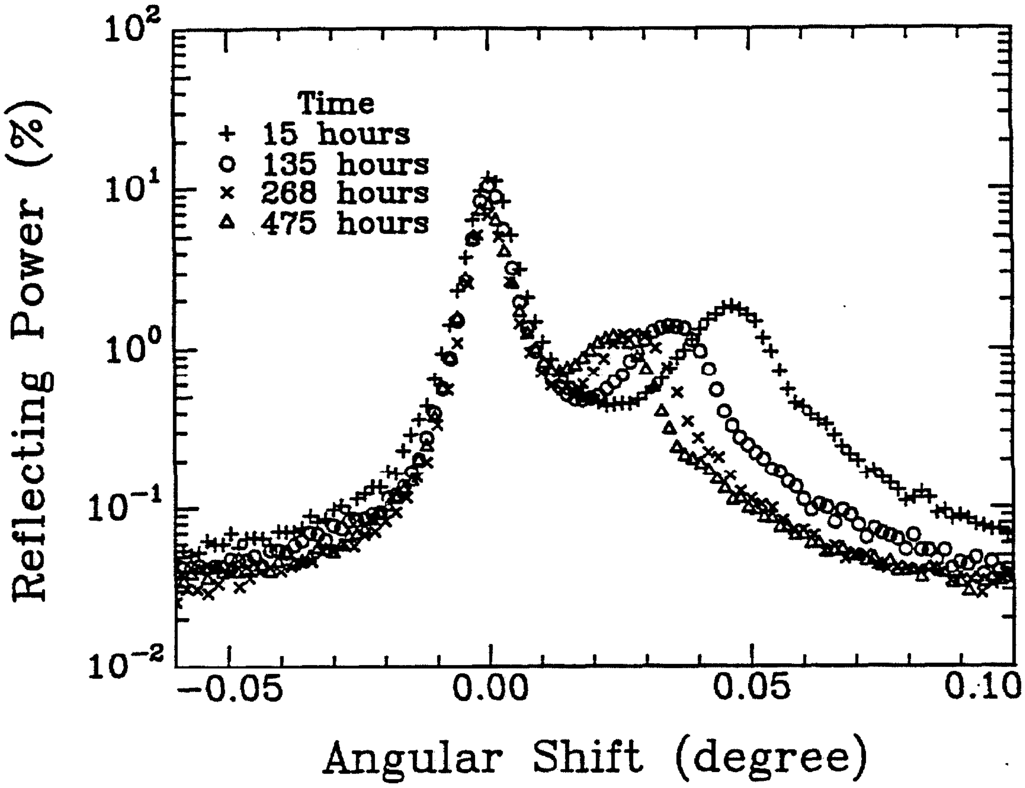

Figure 2.14 A set of XRCs taken at RT from an InP sample implanted by 2 MeV oxygen ions at 77K with a dose of $2\times10^{14}/\mathrm{cm}^2$, showing the RT annealing process in MeV ion implanted InP.

Strain relaxation at RT in air implies that implantation-induced lattice defects in InP are already very mobile near RT. Because this sample was implanted at LN_2 temperature, all defects produced were presumably “frozen-in” during implantation. When it was brought to air at RT, some types of defects can be activated. Processes of diffusion and recombination of these defects would occur; in turn, the implanted crystal relaxes with lattice strain decrease. The phenomena of RT annealing of implanted defects in III-V compound semiconductors has also been observed by Bai, et al. in the keV ion implanted GaAs[41]. Comparing with their results, it may be concluded that at RT, the time constant for radiation-induced lattice strain relaxation in InP is much larger than that of the first stage in GaAs. This indicates that in the InP system, a different type of implantation-induced defects

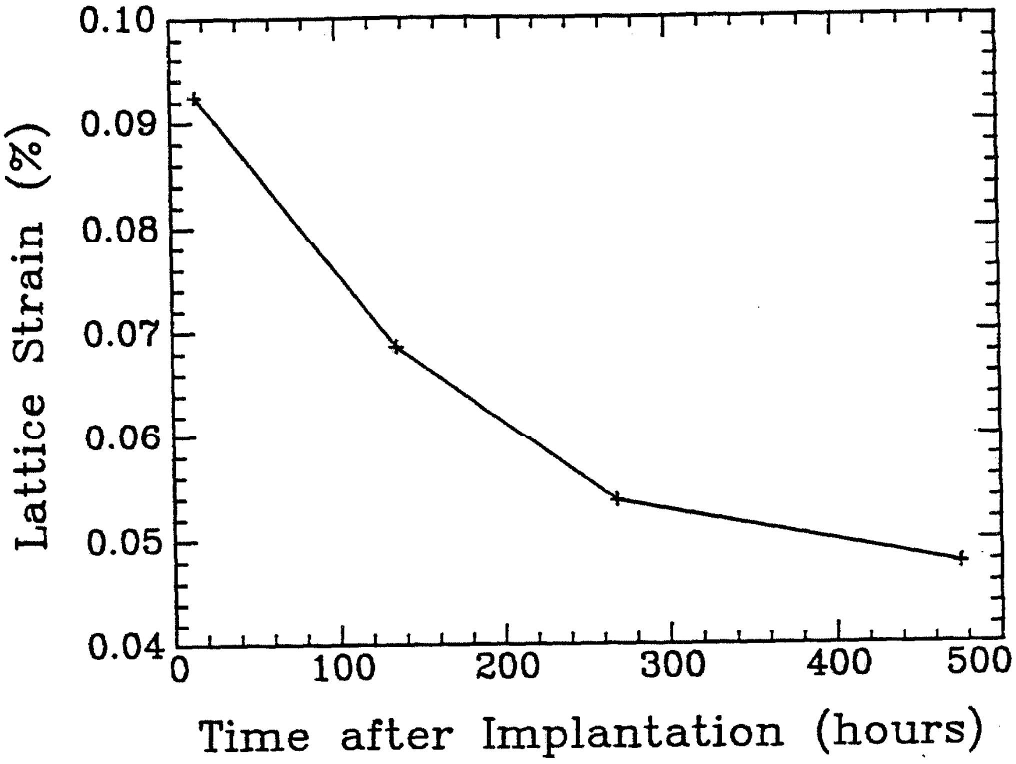

Figure 2.15 Evolution of relaxation of average lattice strain in MeV ion implanted InP. The data are reduced from Fig. 2.14.

exists and they go through distinct annealing processes with higher activation energy and smaller diffusion constants. It may also be suggested that due to deep implantation by MeV ions, lattice defects in the buried layer would take time to diffuse before being trapped at the surface or other sinks. The residual strain level implies the existence of "harder" annealed defects in the sample, which require a high temperature process.

2.7.2. High Temperature Annealing

After high temperature annealing (HT) at 500°C, no significant implant redistribution has been found by NRRA within its detection limit. Profiles of ^{15}N-implanted and HT-annealed samples are not presented here because they are very much the same as ones taken from as-implanted samples. The implant's peak is still centered at the same position as that in the as-implanted sample with a comparable width. This indicates that only very small migration and diffusion of the implanted ^{15}N in InP has occured during the thermal annealing. It is suspected that the nitrogen may be chemically bound in the implanted layer and not just trapped in the damaged zone caused by the implantation.

However, through thermal annealing, lattice structural re-ordering in the damaged regions and recrystallization in the buried amorphous layers have taken place. The density of defects in low dose implanted samples or in the regions on both sides of the buried amorphous layer has dramatically decreased. Meanwhile, recrystallization has also occurred in the buried amorphous layer. The XRC study on isochronically-annealed samples has given a result very similar to GaAs as was reported earlier[22]. Figure 2.16 presents the results taken from 15-MeV-Cl-ion-implanted samples in an isochronical annealing process. Gradual strain recovery was observed through annealing with a jump stage at 250°C-350°C; complete recovery of lattice strain occurred at 450°C. A well-shaped peak from the damage-recovered surface and the substrate appeared at the same position as the peak from the undamaged crystal, but the reflecting intensity dropped to about a half in magnitude and the width was doubled. This is believed to be due to the absorption and scattering by the buried disordered layer deep inside the crystal. Annealing behavior studied by Raman phonon energy shift in a 6-MeV-oxygen ion implanted InP sample has shown a similar result[38].

The CRBS measurement from the annealed samples, as presented in Fig. 2.17, shows a large decrease of the dechanneling yield in the shallow surface region, indicating the recovery of the surface damage and defects through a thermal process (see the spectrum for the dose $5\times10^{14}/\text{cm}^2$ and others in the regions near the surface). However, on higher dose-implanted samples, the backscattering yields from the buried amorphous regions still remain nearly as high as those of the random spectrum. These have been shown to correspond to the highly disordered or

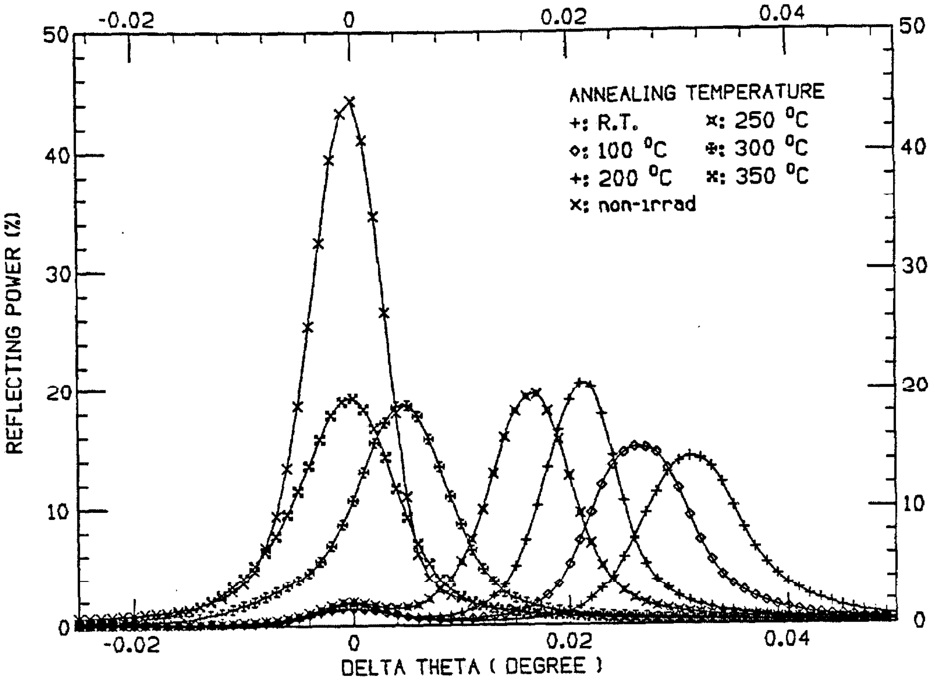

Figure 2.16 XRCs from isochromatically annealed InP, which was implanted with 15-MeV-Cl-ions.

polycrystalline regions, which are recrystallized from the original amorphous layer during high temperature annealing.

The recovery of the surface damage and defects and the formation of highly disordered crystalline structures inside through annealing have been confirmed by XTEM observations. Fig. 2.18 is a typical bright field XTEM micrograph from the sample implanted with 5 MeV nitrogen ions at a dose of $1\times10^{16}/\text{cm}^2$. Comparing with the micrograph of the as-implanted sample (Fig 2.11d), the thermal annealing effect is clearly seen. The surface damage and defects have been significantly annealed, and the point defect density was dramatically reduced. Recrystallization has emerged in the buried amorphous region. Nucleation has taken place in the center of the buried amorphous layer to form the polycrystalline structure in the

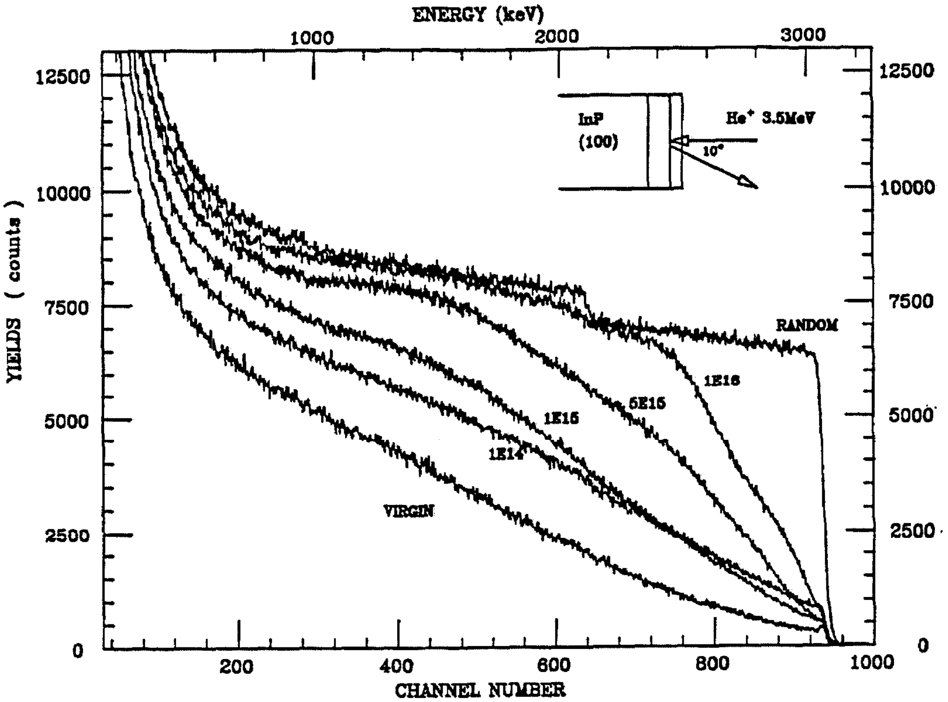

Figure 2.17 Channeling RBS spectra of InP crystals as-implanted with 5 MeV ^{15}N at room temperature with a sequence of doses as marked beside the curves.

center part. Solid phase epitaxial regrowth from two crystalline-amorphous interfaces was stimulated towards the center to form highly disordered structures within the buried band near the interfaces. This interpretation has been confirmed by selected area diffraction patterns taken on the individual regions.

These fine structural features have been observed in the HRTEM presented in Figure 2.19. Fig 2.19a shows the reduction of defect density in a low-dose-implanted and annealed sample (comparing with Fig 2.13a). In Fig 2.19b the inner interface structure in a high-dose-implanted and annealed sample is shown. A high density of long range microtwin clusters and stacking fault bundles grow along {111} directions, seeding from defects that originated during implantation on the amorphous-

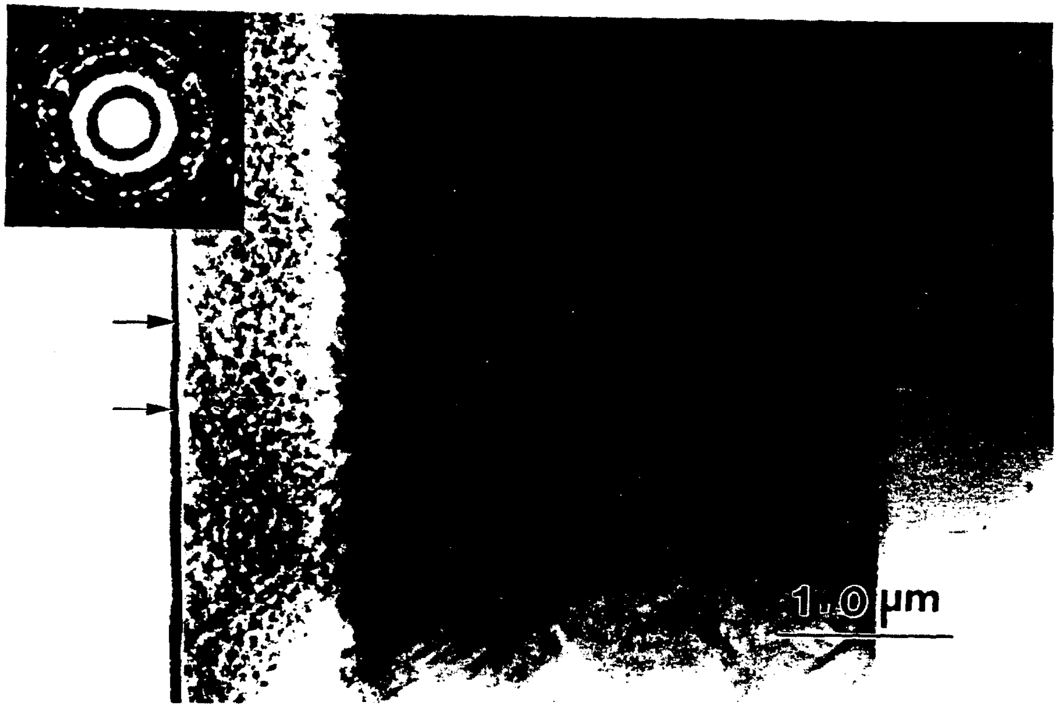

Figure 2.18 XTEM micrographs of the entire implanted regions in ^{15}N ion implanted and annealed (500°C) InP specimens with an implant dose of $1\times10^{16}/\text{cm}^2$. See details in the text.

crystalline interface (see Fig 2.13b). Fig 2.20 illustrates a high magnification view of the HRTEM micrograph of such stacking fautls and twinning structure in MeV nitrogen ion implanted and annealed InP sample as shown in Fig 2.19.

2.8. Summary Remarks

In summary, our studies of MeV-ion-implanted InP have given us a coherent picture of physical processes involve in MeV ion implantation into InP compound semiconductors. The experiments have clearly revealed substantial changes in electrical and structural properties as well as radiation-induced damage distributions and build-up with increasing the implantation dose in the ion implanted InP samples. Several interesting features in MeV-ion-implanted InP crystals and

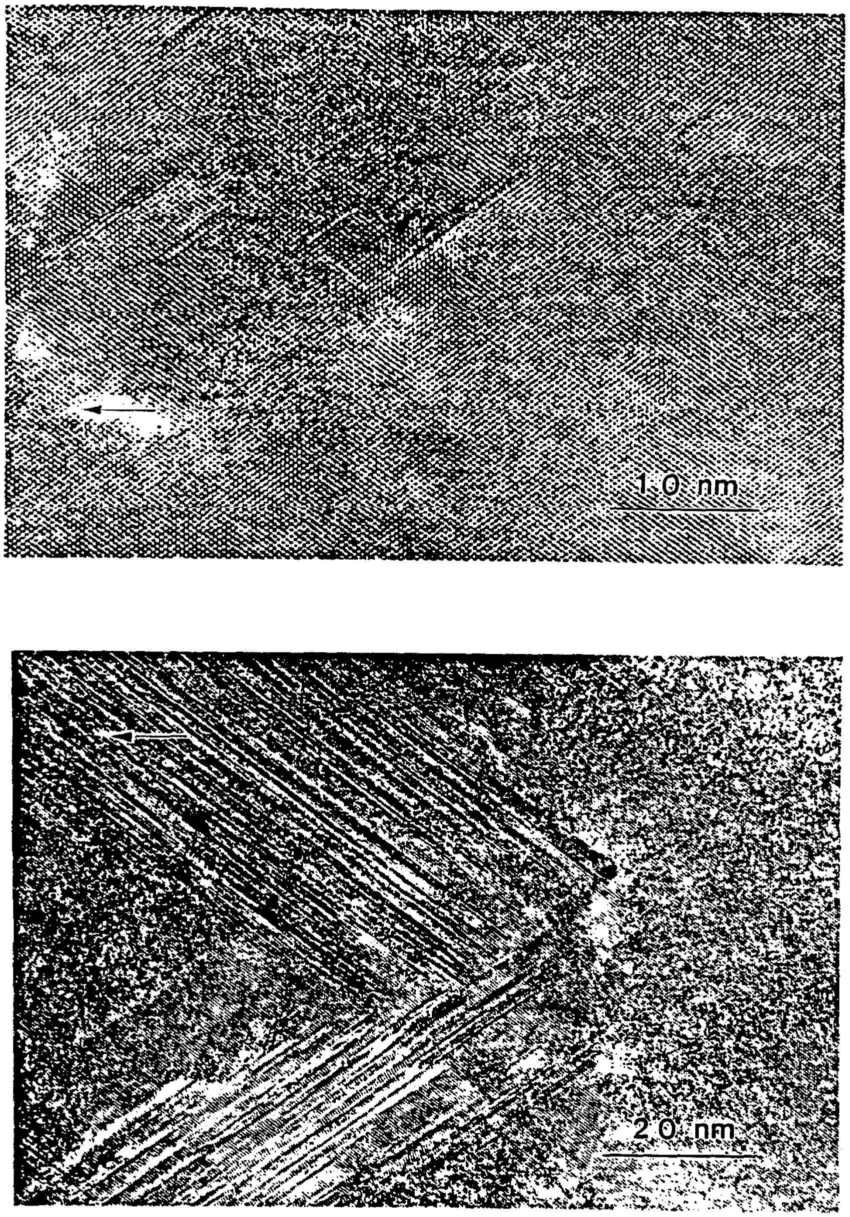

Figure 2.19 HRTEM micrographs of the radiation-induced damage region in thermally annealed (500°C) InP samples. a) low dose implanted, where the defect density has decreased dramatically and only a few stacking faults on {111} directions are presented; b) high dose implanted, where the thermal annealing structure through recrystallization in the original implantation-induced amorphous region is illustrated. A typical regrowth structure, bundles of stacking faults and microtwins are shown. (The arrow points to the sample surface.)

Figure 2.20 A high magnification view of the HRTEM micrograph of stacking faults and twinning structure in an MeV nitrogen ion implanted and annealed InP sample as shown in Fig 2.19.

the relationship between the distribution of implants, the radiation-induced damage profile and the amorphized region in the implanted sample as well as the influence of post-implantation annealing effects have been found. NRRA depth profiling precisely measures the depth range of implants and shows that they have a distorted Gaussian-like distribution with a tail extending towards the sample surface region. The combination of CRBS and XTEM shows the implantation-induced damage profile and the structure transition as well as the influence of subsequent thermal annealing. The damage was found to be distributed along the ion transport path. Starting from the heavily damaged region where the energetic incident ions stop through nuclear collisions, amorphization begins at a critical dose, which is lower than that required for GaAs materials. Formation of a buried continuous amorphous layer is due to overlapping of those initial amorphous zones and collapse of damaged crystalline regions when the accumulated lattice defects reach a critical density. As a result, the buried amorphous layer extends towards the sample surface as the implanted dose increases. Pronounced RT annealing indicates migration of ion implantation-induced defects at RT in air. Subsequent high temperature annealing causes the amorphous layer to recrystallize and the damaged layer to reorder through complex thermal processes, as shown by the CRBS and XTEM results. Recrystallization has been found in the buried amorphous layers through a solid phase epitaxial regrowth process, forming a highly disordered cystalline structure from the interfaces to the center of the layer. It might also go through a homogenous nucleation process in a random direction, initiating at the center region of the amorphous layer and resulting in a polycrystalline structure. The XRC sensitively measures the implantation-induced lattice strain, which is due to the generation of lattice defects. The observed strain saturation is closely correlated to the occurrence of the amorphization. The different strain polarity, compared with the effect in GaAs, has given us an interesting puzzle, which will be discussed in Chapter 5.

We have also demonstrated that MeV nitrogen ion implantation in InP crystals creates deeply buried semiinsulating layers in n-type materials after post-implantation high temperature annealing. High resistivity of up to 10^6 ohm-cm with a breakdown bias larger than 20 volts has been obtained with a minimum dose of about $5\times10^{14}/cm^2$. This layer has also exhibited high thermal stability and reproducibility, which ensures its applicability for device fabrication, in particular in a high-temperature and long-period LPE crystal growth processing. Although the mechanism of isolation is not fully understood at present, the isolation behavior is not directly due to residual ion implantation-induced lattice damage, but rather to highly disordered regrowth structures that require the presence of nitrogen. It is closely associated with substitution of nitrogen atoms into phosphrous sublattices, creating the acceptor-like deep levels that efficiently trap electrical charge carriers. This technique can be used to generate an SOI structure in an InP substrate, or to introduce isolation in the desired region of a device with a better lateral control than that obtainable with proton bombardment. The application to InP laser fabrication is proposed in Chapter 6.

This experiment has also demonstrated the complementary nature of the analytical techniques used for the investigation of the processes involved in high-energy heavy-ion implantation, and led to a good understanding of the mechanism of the interactions between MeV ions and lattice atoms in III-V compound semiconductors.

2.9. References

1. D. C. Ingram, Nucl. Instr. and Methods, B12 (1985) 161, and references therein.
2. F. Eisen, C. Kirkpatrick, and P. Asbeck, in *GaAs FET Principles and Technology*, ed. J. V. Dilorenzo and D. D. Khandelwal (Artech House, Inc., 1982) p.117-p.144; and references therein.
3. Hidetoshi Nishi, Nucl. Instr. and Methods, B7/8 (1985) 395.
4. See Mat. Res. Soc. Symp. Proc., Vol. 53 (1986) and Vol. 107 (1988).
5. A. G. Foyt, W. T. Lindley, C. M. Wolfe, and J. P. Donnelly, Solid State Electronics, 12 (1969) 209.
6. K. Steeples, I. J. Saunders, and J.G. Smith, IEEE Electronic Device Letter, EDL-1 No. 5 (1980) 72.
7. P. N. Favennec, J. Appl. Phys. 47 (1976) 2532.
8. H. Beneking, N. Grote, and Krautle, Solid State Electronics, 22 (1979) 1039.
9. J. M. Blum, J. C. McGroddy, P. G. McMullin, K. K. Shih, A. W. Smith, and J. F. Ziegler, IEEE, J. Quant. Elect., QE-11 (1975) 413.
10. J. C. Dyment and G. Smith, IEEE J. Quant. Elect., QE-17 (1981) 750.
11. F. Xiong, T. A. Tombrello, H. Wang, T. R. Chen, H. Morkoç, and A. Yariv, App. Phys. Lett. 54(8) (1989) 730; and Mat. Res. Soc. Symp. Proc. Vol. 144 (1989) 367.

12. J. D. Sright, et al., Inst. Phys. Conf. Ser., No 33a (1977) 275.
13. J. P. Donnelly and C. E. Hurwritz, Solid State Electronics, 20 (1977) 727.
14. M. W. Focht and B. Schwartz, Appl. Phys. Lett., 42(11) (1983) 970-972.
15. J. P. Donnelly and C. E. Hurwitz, Solid State Electronics, Vol. 21 (1978) 475-478.
16. D. P. Wilt, B. Schwartz, B. Tell, E. D. Beebe, and R. Nilson, Appl. Phys. Lett., 44(3) (1984) 290.
17. F. Xiong, T. A. Tombrello, T. R. Chen, H. Wang, Y. H. Zhuang, and A. Yariv, Nucl. Instr. and Methods, B39 (1989) 487.
18. Fulin Xiong, F. Rauch, Chengru Shi, Zhuying Zhou, R. P. Livi, and T. A. Tombrello, Nucl. Instr. and Methods, B27 (1987) 432.
19. H. H. Andersen and J. F. Ziegler, *Hydrogen Stopping Powers and Ranges in All Elements*, in *The stopping and Ranges of the Ions in Matter,* Vol. 3, ed. J. F. Ziegler (Pergamon Press Inc., 1977).
20. V. S. Speriosu, J. Appl. Phys. 52(10) (1981) 6094.
21. T. Vreeland Jr. and B. M. Paine, J. Vac. Sci. Technol. A 4(6) (1986) 3153.
22. C. R. Wie, T. Vreeland, Jr., and T. A. Tombrello, Nucl. Instr. and Methods, B16 (1986) 44; Phys. Rev. B33 (1986) 4083; J. Appl. Phys. 59 (1986) 3743.
23. W. K. Chu, J. W. Mayer, and M-A Nicolet, *Backscattering Spectrometry* (Academic Press, New York) (1978).
24. L. C. Feldman, J. W. Mayer, S. T. Picraux, *Materials Analysis by Ion Channeling* (Academic Press, New York) (1982).
25. P. Hirsch, A. Howie, R. B. Nicholdon, D. W. Pashley, and M. J. Whelan, *Electron Microscopy of Thin Crystals* (Robert Krieger Publishing Company, Florida) (1977).
26. G. Thomas, in *Diffraction and Imaging Techniques in Material Science,* Vol. 1, ed. by S. Amelinckx, R. Gevers, and J. Van Landuyt; (North-Holland, New York) (1978) p. 217.
27. J. C. Bravman and R. Schinclair, J. Electron Microscope Tech. 1 (1984) 53.
28. N. G. Chew and A. G. Cullis, Appl. Phys. Lett. 44(1) (1984) 142.

29. See discussions in Secion 3.1 in ref. 18 and references therein.

30. J. F. Ziegler, J. P. Biersack, and U. Littmark, *The Stopping and Range of Ions in Solids,* Vol. 1 (Pergammon Press) (1985).

31. Fulin Xiong, Tandem Lab Report, Caltech (1987), unpublished.

32. J. C. Phillips, *Bonds and Bands in semiconductors* (Academic Press, New York) (1973), p. 240.

33. A. Baldereschi and J. J. Hopfield, Phys. Rev. Lett. Vol. 28(3), 171 (1972).

34. J. C. Phillips, *Bonds and Bands in semiconductors* (Academic Press, New York) (1973), p. 227.

35. W. M. Duncan and S. Matteson, J. of Appl. Phys., 56(4) (1984) 1059.

36. R. A. Faulkner, Phys. Rev. 175, 991 (1968).

37. V. S. Speriosu, B. M. Paine, M-A. Nicolet, and H. L. Glass, Appl. Phys. Letts., 40 (1982) 604.

38. C. R. Wie, T. Vreeland Jr., and T. A. Tombrello, Nucl. Instr. and Methods, B9, (1985) 25.

39. C. R. Wie, T. Jones, T. A. Tombrello, T. Vreeland, F. Xiong, Z. Zhou, G. Burns, and F. H. Dacol, Mat. Res. Soc. Symp. Proc., Vol. 74 (1987) 517.

40. T. T. Bardin, J. G. Pronko, F. A. Junga, W. A. Opyd, A. J. Mardinly, F. Xiong, and T. A. Tombrello, Nucl. Instr. and Methods, B24/25 (1987) 548.

41. G. Bai, D. N. Jamieson, M. A. Nicolet, and T. Vreeland Jr., Mat. Res. Soc. Symp. Proc. Vol. 93 (1987) 67.

Chapter 3

MeV ION IMPLANTATION INTO GaAs-AlAs SYSTEMS

3.1 Introduction

GaAs is a very important material among III-V compound semiconductors used in high speed logic, microwave, and optoelectronic devices. Ion beam processing in the keV energy range for property modification of GaAs has been extensively studied. MeV ion implantation offers an extension of this process with a high degree of application potential in integrated circuits and 3-dimensional device technology. At Caltech, Wie, et al. first undertook an investigation of MeV-ion-implantation-induced lattice strain in the GaAs system[1]. Later on, we also performed studies of the changes in electrical properties and crystalline structure in GaAs due to MeV ion implants[2]. The preliminary results have revealed defect generation and annealing, and phase transitions by MeV ion implantation and subsequent high temperature annealing processes. One can also find elsewhere a number of reports on MeV-ion-implantation-induced effects, especially the electrical carrier activation, in GaAs. However, many aspects in the fundamental study of mechanisms of radiation-induced damage and activation processes for the practical control of implantation and annealing conditions are still not well understood. The experimental studies to be presented in this chapter emphasize MeV ion induced resistivity change and the influence of target temperature on phase transition during MeV ion implantation. The results of an investigation of MeV-oxygen-ion-implantation-induced compositional intermixing in GaAs/AlAs superlattices are also presented.

3.2 MeV-Oxygen-Ion-Implantation-Induced Electrical Isolation in GaAs

Oxygen ion implantation as a means of creating semi-insulating layers in GaAs was first reported by Favennec et al.[3,4]. It showed that oxygen implantation by chemical doping results in a stable semi-insulating GaAs layer. Recently Bryan et al.[5] have shown that oxygen ion-implantation-created semi-insulating layers in GaAs are thermally stable to at least 850°C. From the point of view of practical utilization, we investigated the electrical resistivity changes with the implant dose and the beam energy in MeV-oxygen-ion-implanted GaAs. By the *in situ* measurement of sheet resistivity during implantation, we found that in as-implanted GaAs samples, there exists a threshold at a dose of about $5 \times 10^{11} ions/cm^2$ for rapid resistivity change, and the sheet resistivity can reach to $10^9 \Omega/\Box$ in a 2 μm thick layer. We have also found that selective carrier compensation exists in oxygen-ion-implanted GaAs, because implantation-induced resistivity in p-type GaAs would disappear after annealed at temperatures above 600°C, while it is sustained in n-type GaAs. This provides some flexibility for practical application.

3.2.1. In situ Measurement of Electrical Resistivity Change in GaAs during Implantation

In situ measurement of high resistivity in MeV-oxygen-ion-implanted GaAs has been performed in order to monitor the resistivity change as a function of the ion dose during implantation.

The experimental set-up is shown in Fig. 3.1. The sample used in this study was grown by MBE with a 2 μm thick n-type GaAs layer on the semi-insulating (Cr doped) GaAs(100) substrate. The surface layer was doped with Si at an electrical carrier concentration level of about 1×10^{17} /cm^2. In each experiment, the sample was cut into a size of about 20 × 3 mm^2. The ohmic contacts with 100 Å Au-Ge alloy and then 1100 Å Au on the top were placed at the two ends of the sample faces 1.6 cm apart, with two electrodes leading to outside the vacuum chamber. Implantation

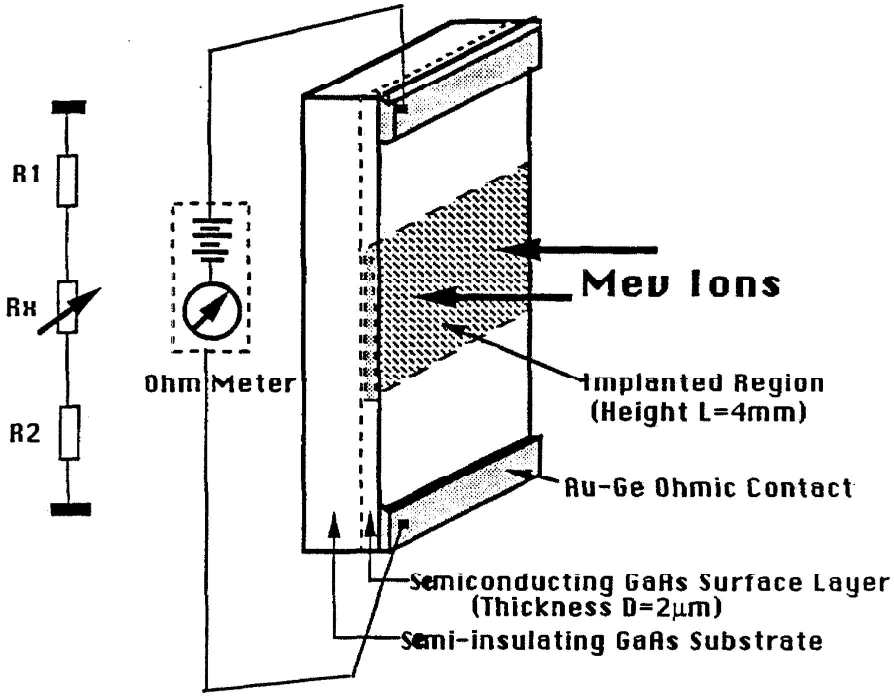

Figure 3.1 A schematic view of the experimental set-up for *in situ* resistivity measurement during ion implantation. On the left, an analogue view of resistances in an implanted sample is shown.

was conducted with an oxygen ion beam at several different energies. The beam was defocused and projected normally on the central region of the sample, as shown in Fig. 3.1, through a collimator of 4 × 6 mm^2. During implantation, the beam was frequently interrupted at a required dose for *in situ* resistivity measurement with Keithley 614 Electrometer. An I-V curve tracer was also occasionally used to ensure the lineality of the I-V characteristic curve.

In an n-type semiconductor, the sample resistance can be estimated with the sample geometry (L×W×D), doping concentration (n), and electron mobility (μ_e) by the formula[6]

$$R = \rho \frac{L}{DW} = \frac{1}{en\mu_e} \frac{L}{DW}. \tag{3.1}$$

In turn, the sheet resistivity can be expressed as

$$\rho_s = \frac{\rho}{D} = R\frac{W}{L}. \tag{3.2}$$

Table 3.1 lists both estimated and measured resistances of unimplanted samples. They are quite consistent with each other, when errors from geometric measurement are considered. After implantation, the sample is divided into three regions, an implanted region in the center and two unimplanted parts at two ends. The resistance in the implanted region (R_x) changes and becomes much higher than that of unimplanted parts (R1 and R2, see Fig. 3.1), then $R \simeq R_x$.

Table 3.1 A list of the samples used in the *in situ* resistivity measurement in oxygen-ion-implanted GaAs.

Sample	Geometry	R(Ω)(unimpl.)		Ion	Depth Range
	L × W (mm^2)	(estimated)	(measured)	Energy	of Ions (μm)
#1	16.0×3	192.8	188	3 MeV	2.27±0.67
#2	15.8×2.7	211.2	208	5 MeV	3.23±0.73
#3	16.0×2.6	225.3	226	8 MeV	4.58±0.80

Fig. 3.2 presents the experimental data of the resistivity change as a function of the implant dose as well as the ion energy. One can first see that the resistivity in as-implanted GaAs can reach above $10^8\Omega/\square$. A dose threshold for the rapid resistivity change takes place at about 5×10^{11}ions/cm^2, varying with the beam energy. The higher the beam energy is, the higher dose is required. Following Eq. 3.1, it may be concluded that this high resistivity change originates either from carrier concentration compensation by implanted oxygen ions, or from a decrease of

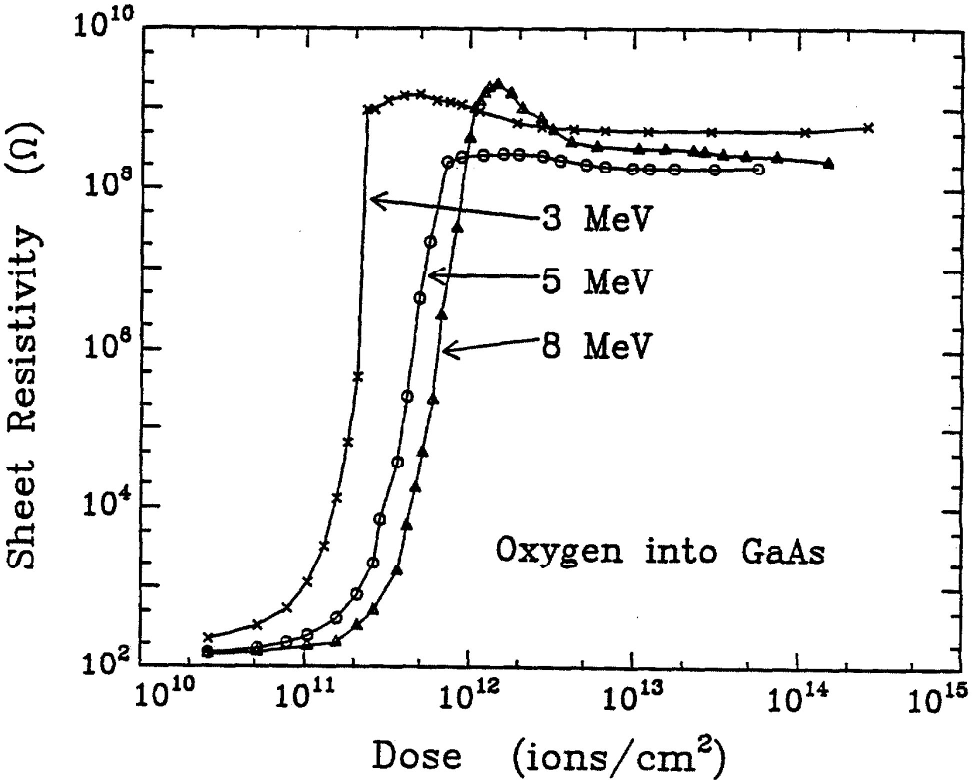

Figure 3.2 Experimental measurement of sheet resistivity changes as a function of the ion dose in MeV-oxygen-ion-implanted GaAs.

electrical carrier mobility through an electron trapping process by ion-implantation-induced lattice damage and deep levels. However, we should notice here that at this moment during implantation, most resistivity is due to lattice structural damage and instant electronic damage. As we will discuss later, MeV ion implantation involves two major damage processes — the electronic spike in most of the surface region and the nuclear spike at the EOR of ions. Due to their different damage effects to the crystal, the nuclear spike is more efficient than the electronic spike in terms of high resistivity generation. In the cases presented here, as estimated (see Table 3.1), depending on the ion incident energy, ions may stop within or beyond the 2 μm thick surface semiconducting layer. Thus, as the beam energy is varied from 3 MeV to 8 MeV, the dominant damage process in the surface layer shifts from nuclear spike to electronic spike. As a result, the mechanisms for the sheet resistivity change in GaAs varies from direct carrier compensation to carrier mobility decrease.

3.2.2 Selective Carrier Compensation in Oxygen-Implanted GaAs

It is believed that in oxygen ion implanted GaAs, when a chemical doping effect is dominant, the electrical isolation is mainly due to oxygen-associated deep levels in GaAs, which trap electrons but not holes[4]. We have experimentally confirmed this effect of selective carrier compensation. The n^+-type (Si doped) and p^+-type (B doped) GaAs samples were implanted with 1 MeV oxygen ions at a dose of $2\times10^{14}/cm^2$. After being annealed at temperatures under 600 °C, both samples remained insulating, which is perhaps due to residual radiation damage. The result was different after they were annealed above 600°C. Fig. 3.3 presents the I-V characteristic curves of implanted GaAs samples that were annealed at 650°C. It illustrates the conducting behavior in the p-type material (curve a) and the insulating behavior in n-type material (curve b).

With this selective electrical carrier compensation in GaAs, the requirements on the mask build-up and ion beam energy selection could be more flexible when using implantation for device fabrication. Thus, one can easily tailor the device structures by varying the ion energy and the implant dose. An example of application in device fabrication will be presented in Chapter 6.

3.3. Influence of Target Temperature on MeV-Ion-Implantation-Induced Lattice Damage and Phase Transition

The knowledge of the connection between the implantation conditions and the radiation-induced defect structure and distribution is of high scientific and technological interest because electrical and structural properties of implanted samples

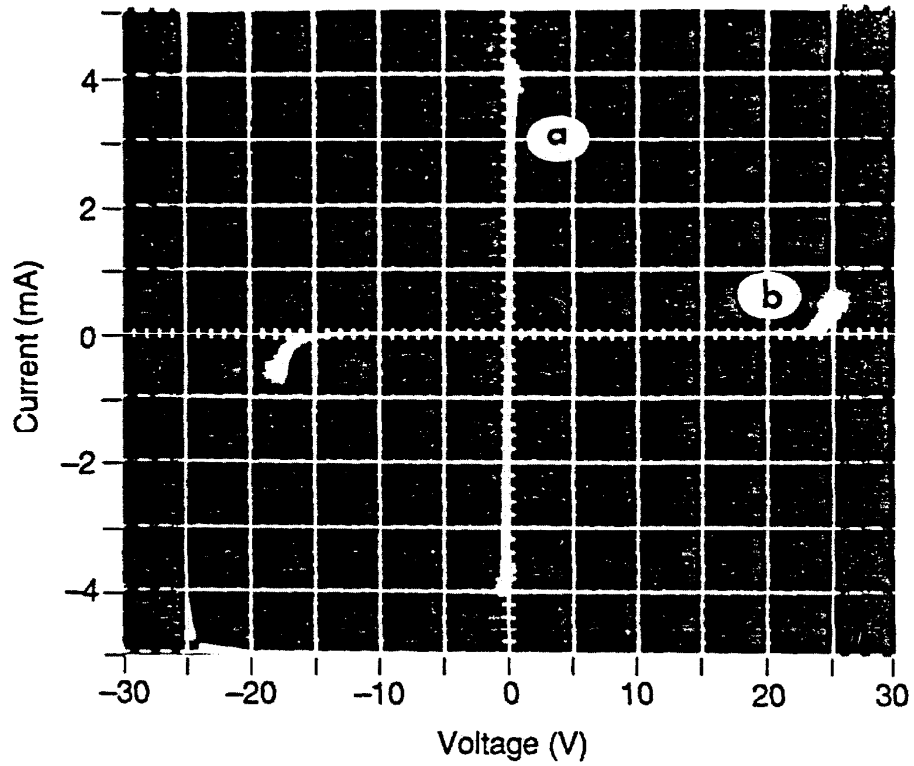

Figure 3.3 I-V characteristic curves of oxygen ion implanted and annealed (650°C) GaAs single crystals: (a) p-type GaAs, conducting; (b) n-type GaAs, insulating.

as well as post-implantation processes necessary for damage annealing and dopant activation are highly influenced by the degree of lattice disorder and damage. This is much more pronounced in III-V compound semiconductors. Among many influences on the defect production and annihilation during ion implantation, the substrate temperature is one of the most important. Many studies of the GaAs system have been made in the keV range of the temperature influence on the critical amorphization dose and electrical property in implanted samples[7]. A remarkable *in situ* annealing process has been found to be invloved during the implantation at RT and above. Similar phenomena has been noticed in MeV ion implantation[8].

The present study of the influence of the target temperature on the radiation-induced strain field and phase transition in MeV oxygen ion implanted GaAs crystals has been made using the techniques of XRC, CRBS, and SIMS. The results have shown a strong *in-situ* dynamic annealing process involved in the implantation at RT with a moderate beam current. This causes implant diffusion and defect migration, resulting in lattice strain build-up and saturation. Implantation in LN_2 temperature (LNT) introduces a so-called "freeze in" effect. It prevents initial radiation-created lattice damage and defects from recombination and diffusion, and in turn drives more efficiently the c-a transition during implantation. The amorphous layer formed provides a region for strain relaxation.

3.3.1 Experimental Aspects

The n-type GaAs(100) single crystalline wafer, doped with Si at a carrier concentration of $5\times10^{18}/\text{cm}^3$ was used in this study. Oxygen ions with energy 2 MeV were implanted into GaAs with doses ranging from $5\times10^{13}/\text{cm}^2$ to $2\times10^{16}/\text{cm}^2$. The implantation was carried out either at ambient RT or at LNT. The beam current density in all cases was maintained constantly at $\sim 5 \times 10^{11} ions/sec/cm^2$ in order to obtain comparable results.

Charaterization of both RT and LNT implanted samples was done at RT. The implant distribution was profiled by SIMS with 16 keV Ar ions as a primary source. Crystalline damage profiling was taken by CRBS with $^4He^+$ beam of 4 MeV. The XRC technique was utilized in symmetrical (400) diffraction for perpendicular lattice strain profiling. In the data analysis, the dynamical diffraction model was employed due to deep implantation. The behavior of profiles of lattice strain was first proposed, based on implant distribution established by SIMS and the distribution of implantation-induced vacancies by TRIM simulation. Then, the proposed strain profiles were modified until the calculated XRCs best fit to the experimental ones.

3.3.2 Results and Discussions

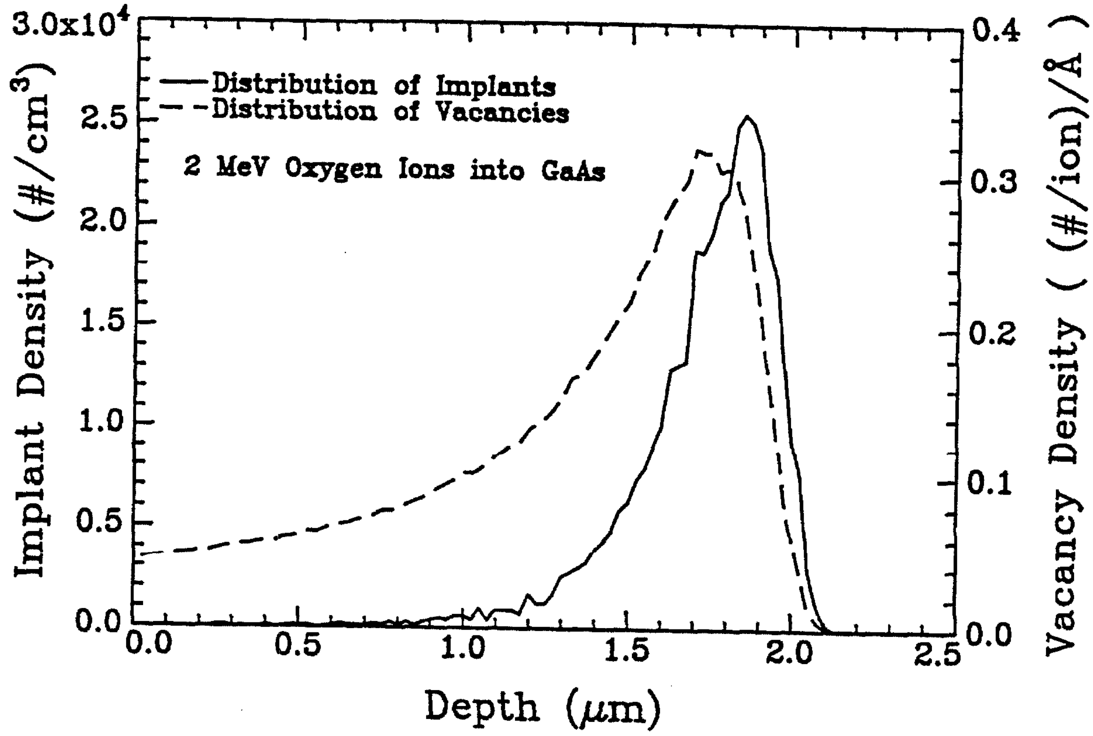

Figure 3.4 Distributions of 2 MeV oxygen ion implants and implantation-created vacancies in GaAs, calculated by TRIM code.

Fig. 3.4 shows a TRIM simulation result that has given us a preliminary insight of the implant distribution and the damage profile for 2 MeV oxygen ions in GaAs. It predicts that the implants would follow a distorted Gaussian distribution with an average range at a depth of 1.72 μm and standard deviation of 0.23 μm (FWHM=0.23×2.36 μm). The profile of implantation-generated vancancies has a slight shift towards the surface with respect to the implant distribution, a damage tail extending into the surface region. Because the TRIM calculation is based on Monte Carlo simulation of energetic ion transport in a randomly oriented material, no information about crystalline structure and defect overlapping and annihilation has been taken into account.

The SIMS profiles of oxgen in both RT and LNT implanted GaAs samples are

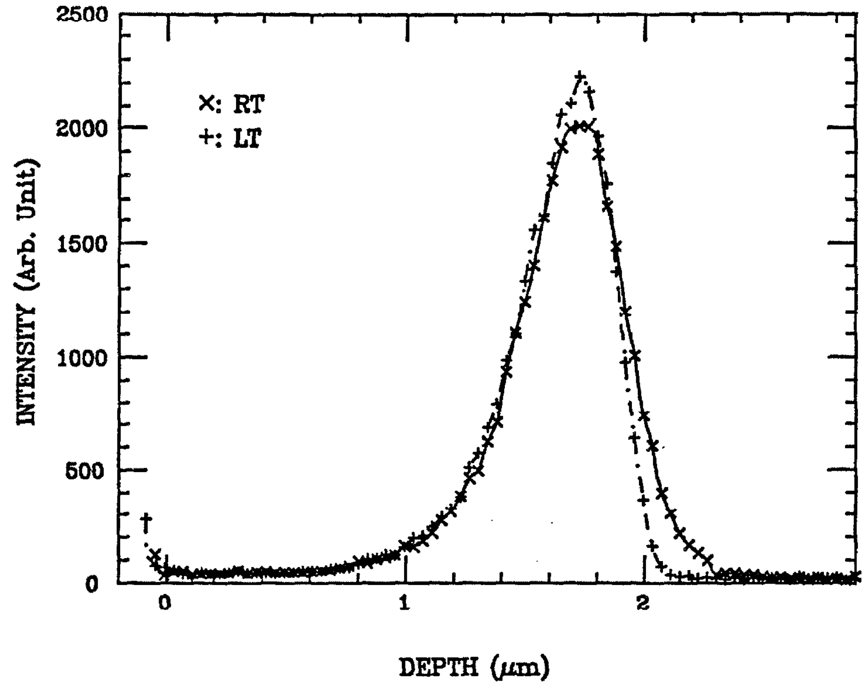

Figure 3.5 SIMS oxygen profiles in GaAs implanted by 2 MeV oxygen ions (a) at RT (× points) and (b) at LNT (+ points).

shown in Figure 3.5. The data have been normalized by setting the integration yield equal to a unit. The profiles indicate a distorted Gaussian-like distribution with the peak at 1.85μm and the FWHM of 0.55μm. No significant difference between the profiles of these two samples has been found, except a slight broadening in the RT implanted sample.

However, the extraordinary difference of the influence of implantation temperature on defect production and damage profiles has been revealed by CRBS and XRC measurements. Two sets of CRBS spectra from RT and LNT implanted samples in Figure 3.6 illustrate clearly the evolution of lattice damage as a function of the implant dose. In the LNT implanted samples, the lattice damage increases remarkably with the implant dose. The heavily damaged regions peak around 1.75

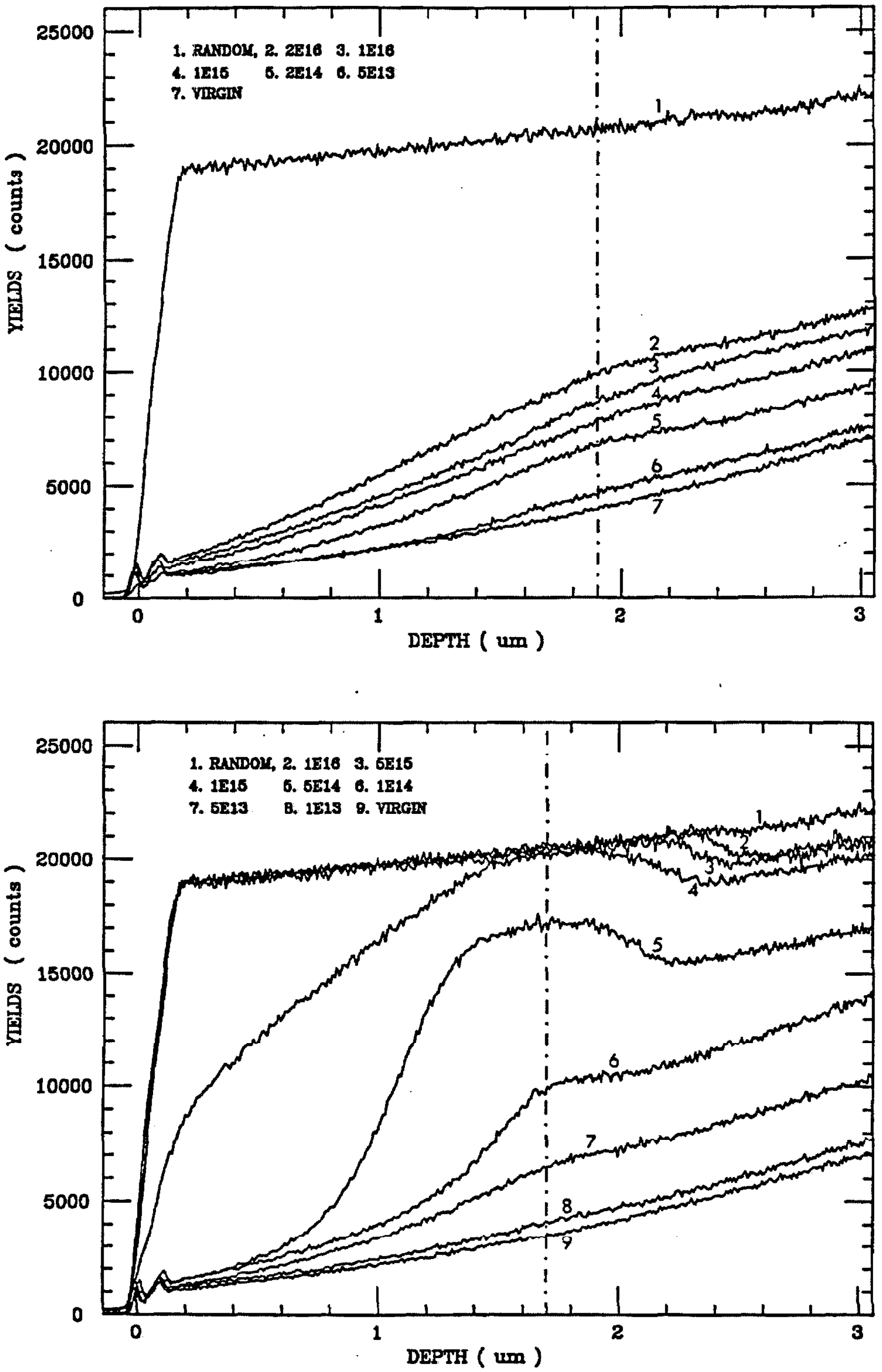

Figure 3.6 CRBS stpectra of 2-MeV-oxygen-ion-implanted GaAs, showing the different evolution of lattice damage as a function of the implant dose. (a) RT implanted, (b) LNT implanted.

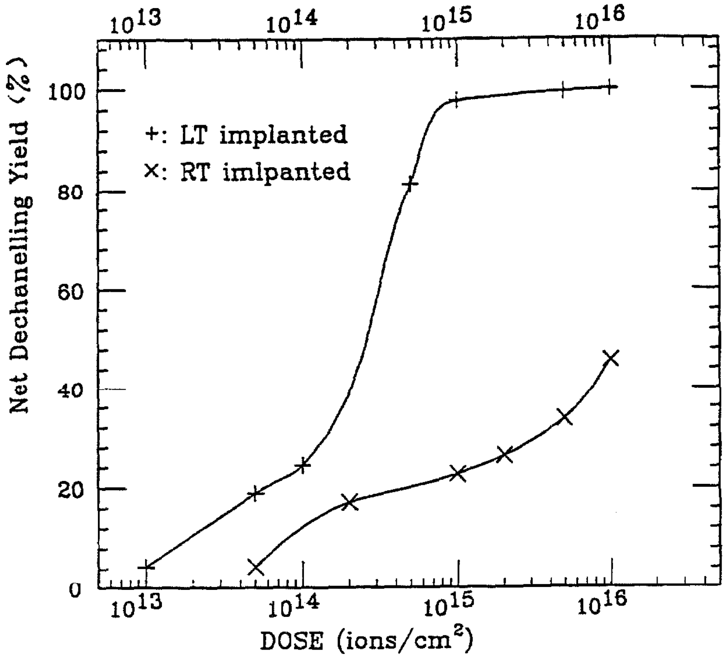

Figure 3.7 The net dechanneling ratio at the heavily damaged region as a function of the implanted dose in 2-MeV-oxygen-ion-implanted GaAs. The data are reduced from Figure 3.6.

μm, consistent with the profiles from TRIM simulation and SIMS measurement. Figure 3.7 shows the net dechanneling ratio at these points as a function of the dose. It is recognized that the threshold dose for completed c-a phase transition takes place at $1\times10^{15}/\mathrm{cm}^2$. In the surface region, lattice damage accumulates very slowly at low doses; the c-a phase transition occurs at high doses when the lattice disorder reaches a critical level and the lattice suddenly collapses. In the RT implanted samples, it is found that the lattice damage is much less pronounced. The heavily damaged region lies a little deeper than that in LNT implanted samples. The behavior of lattice damage at this point as a function of the dose as plotted in Figure 3.7, gives a distinct comparison with the case of RT implantation. It indicates clearly that substantial in situ dynamic annealing is involved during implantation, and only a small amount of lattice disorder can remain after implantation.

In another aspect, the XRC measurement has revealed the temperature influence on lattice damage nucleation and strain build-up. Figures 3.8 and 3.9 present, respectively, the XRCs of these two sets of samples. The cross-symbol points are direct experimental data. The solid curves are the calculated XRCs by the dynamical model with the profiles of strain (solid line) and damage (dot line) given beside each XRC plot. In the RT implanted samples, the maximum damage region is found at around 2 μm, deeper than that simulation result by TRIM. The lattice strain builds up at low doses, following the vacancy distribution simulated by TRIM, then quickly saturates to a level of 0.4%, originating from the heavily damaged region and extending towards the surface as the dose increases until a constant strain field is distributed over the surface. The lattice damage parameter slowly increases and then remains in an equilibrium level with a maximum of 0.15 Å. No evidence shows the amorphization taking place in the samples up to a dose of $2\times10^{16}/\mathrm{cm}^2$, which is consistent with CRBS results and gives another strong indication of the in situ dynamic annealing effect. In the LNT implanted samples, the center of the heavily damaged region is located with a maximum depth around 1.8μm, close to the TRIM prediction.. The lattice strain closely follows the vacancy distribution pattern from TRIM calculation, which indicates a “freeze-in” process taking place during ion implantation. The strain persists until a buried amorphous layer forms when the vacancy concentration reaches a critical level. The amorphous region extends to the surface as the dose increases. The mean atomic displacement in the amorphous layer is around 0.6Å, a large fraction of the interatomic distance in the lattice. One interesting point that should be noticed is that the XRC simulation gives us a strain-free surface in both LT and RT implanted samples. This can be understood by the concept of defect diffusion that the surface acts as a sink for diffused-in vacancies.

In simpliest form, the lattice damage processes involved in ion implantation can also be classified into two main categories: 1) defect generation by collision

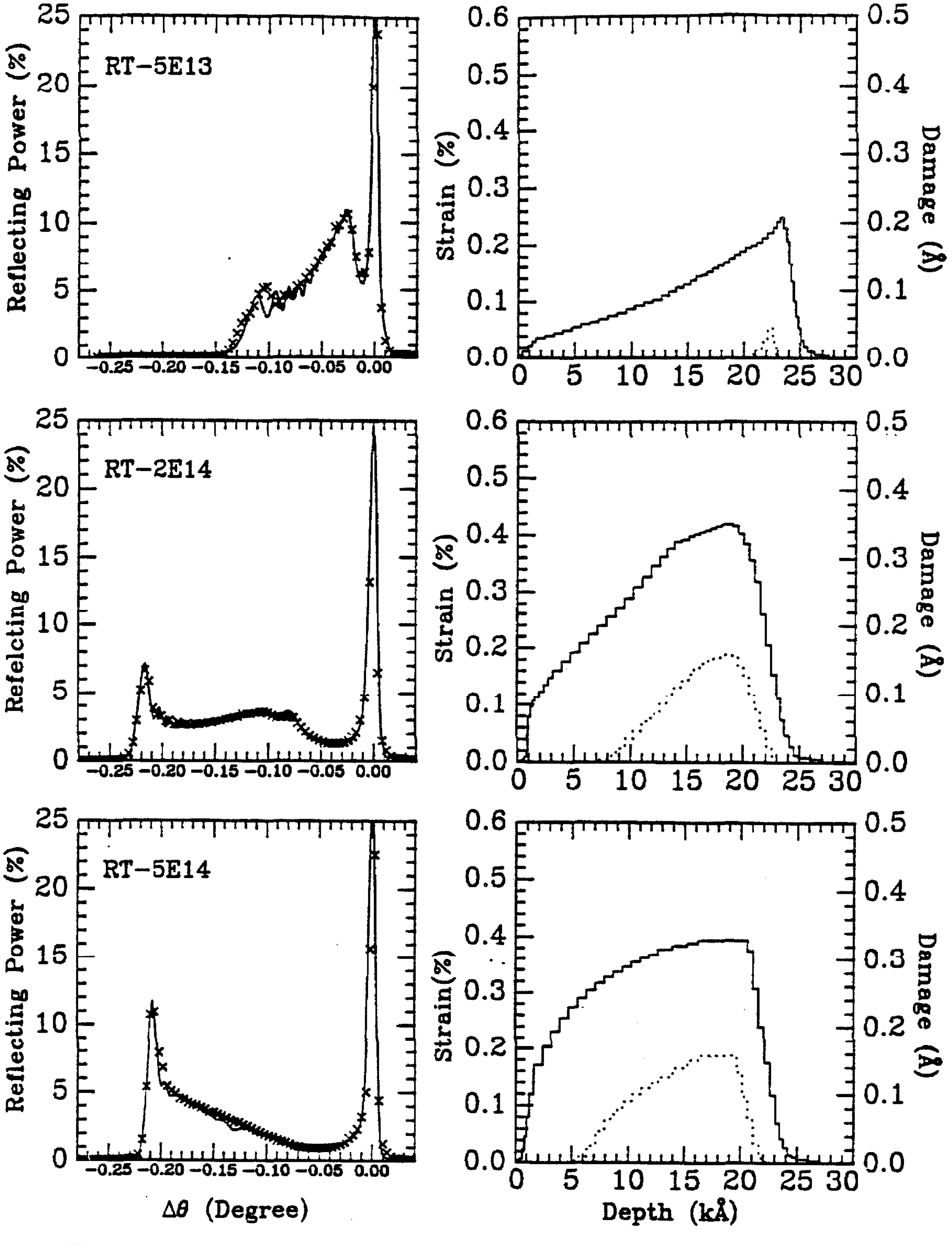

Figure 3.8 XRCs of 2-MeV-oxygen-ion-RT-implanted GaAs. The corresponding implant doses are marked in the figure. The crosses show the experimental data, and the solid curves are the simulation by the dynamical model. The strain (solid curves) and damage (dotted curve) profiles as a result of simulation are plotted beside each XRC.

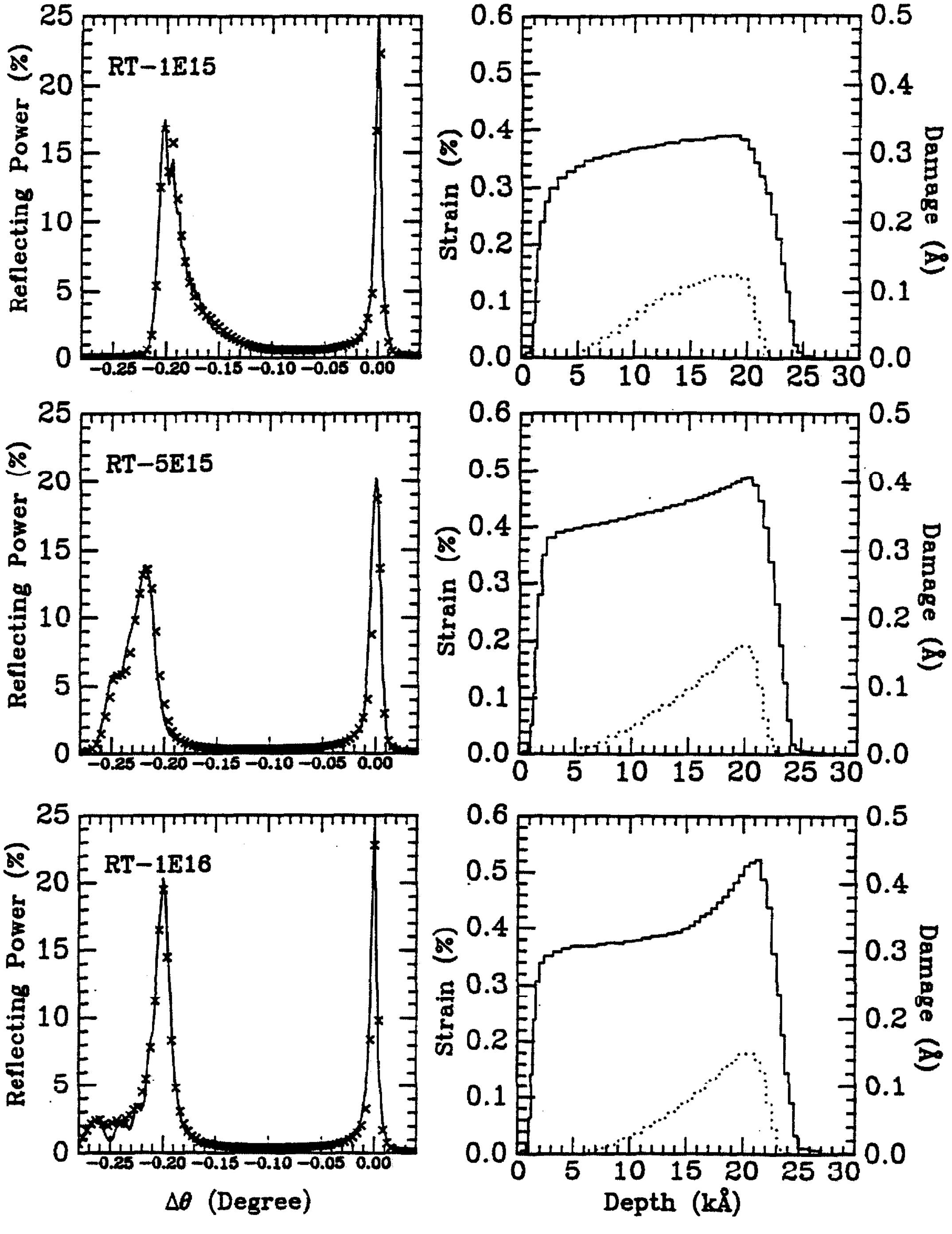

Figure 3.8 (continued)

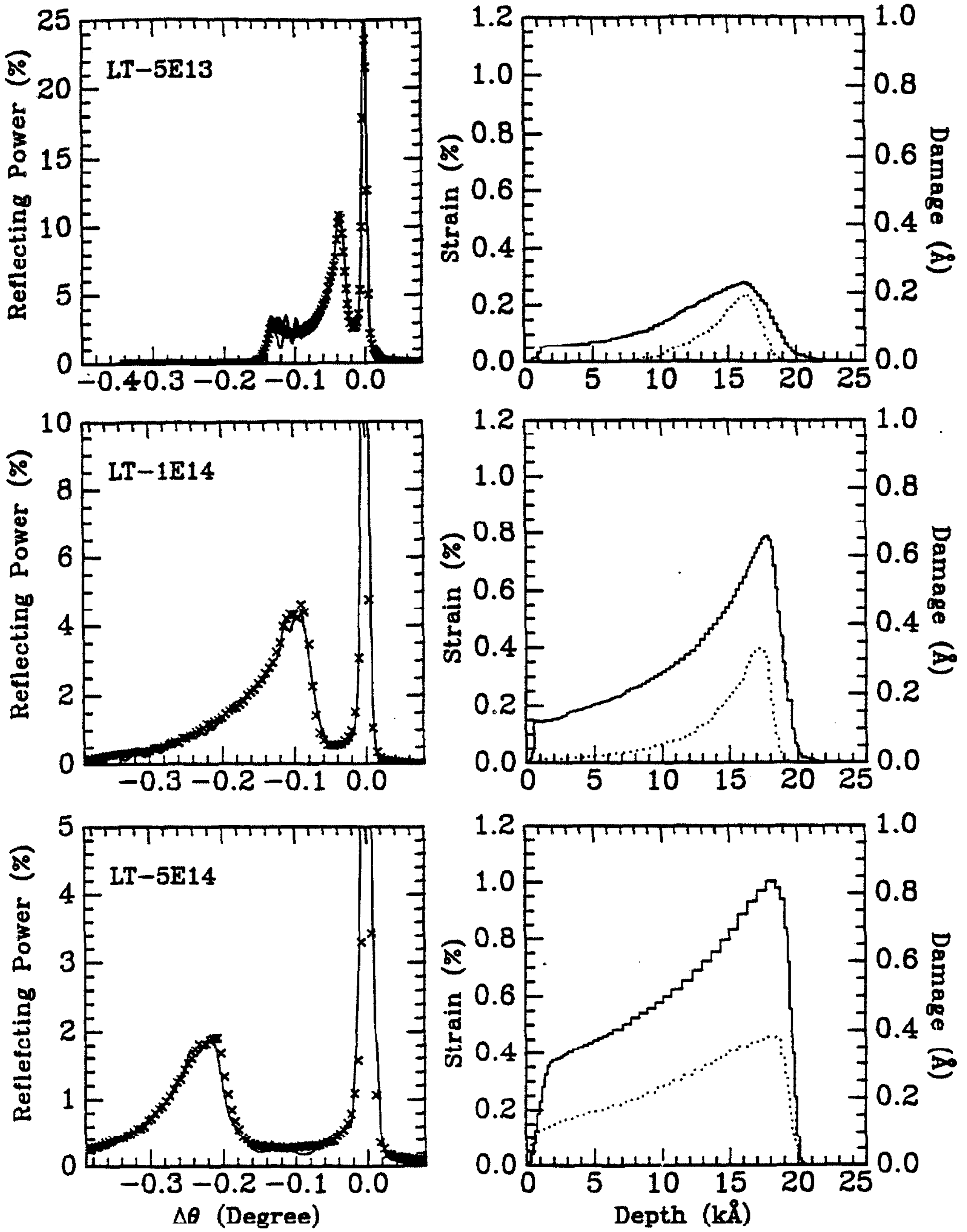

Figure 3.9 XRCs of 2-MeV-oxygen-ion-LT-implanted GaAs. The corresponding implant doses are marked in the figure. The cross sign points are the experimental data, and the solid curves are the simulation by the dynamical model. The strain (solid curves) and damage (dot curves) profiles as a result of simulation are plotted aside each XRC.

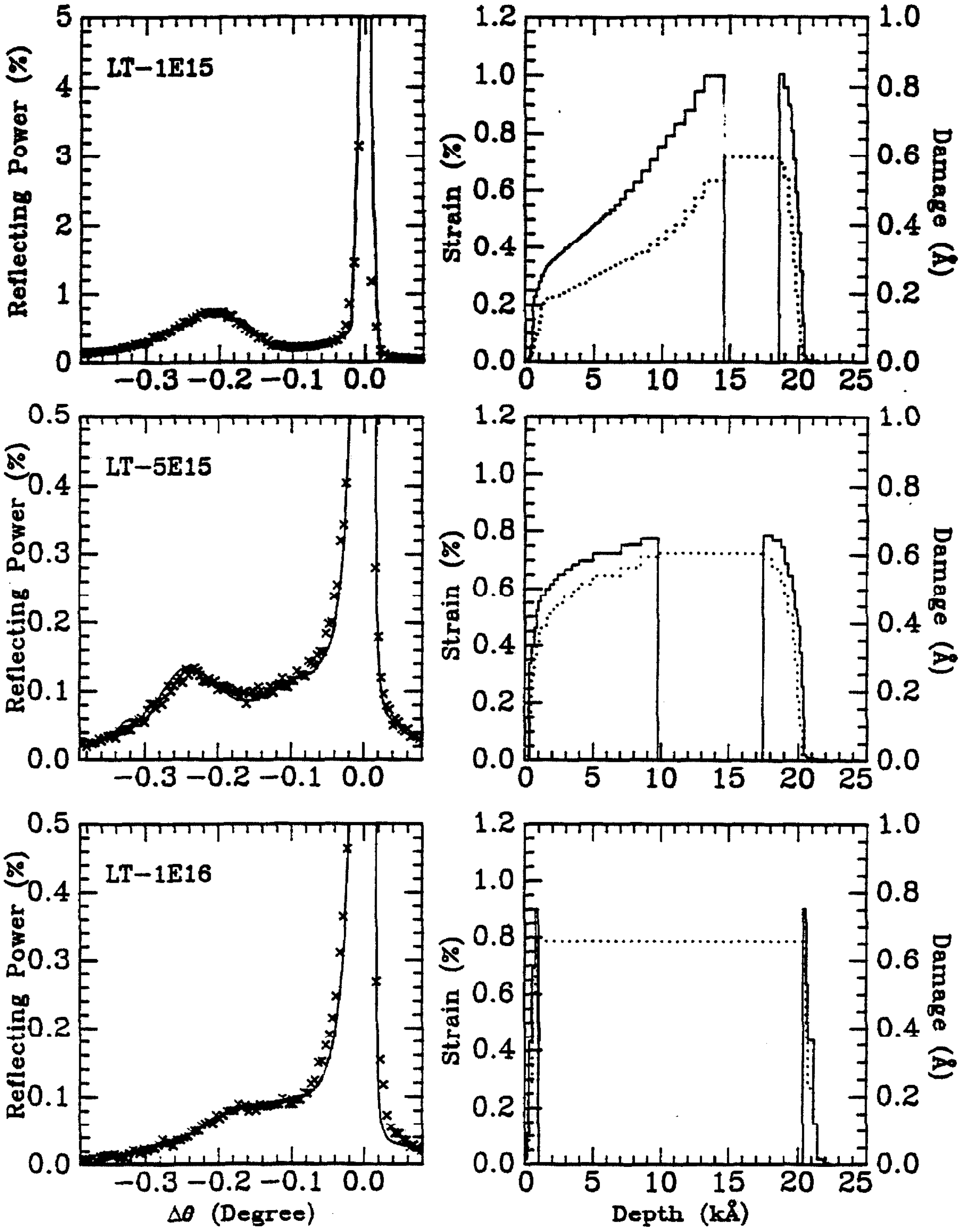

Figure 3.9 (continued)

cascades, and 2) defect migration and recombination due to associated thermal effects. The final state in the implanted region after implantation is just the result of competition between these two processes. In low temperature implantation, the first process may dominate the second one, and then amorphization can take place; while in high temperature implantation, the later process may overcome the first one. In this case the strong in situ annealing is present and sufficient lattice disorder can not be sustained to form an amorphous zone in the sample after implantation. The RT implantation can be either of these cases, dependent upon the material properties and other implantation parameters such as the beam flux density. The case discussed above may fall into the HT implantation category, which may be due to the high diffusivity of implantation-created complex defects in GaAs and beam-induced local instant sample heating. Lattice strain represents a degree of lattice disordering. Its saturation in RT implanted samples indicates an equilibrium between generation and annealing of radiation-induced defects. In LT implantation, lattice strain quickly builds up at first and collapses when the disordered region undergoes a c-a transition.

3.4. Oxygen-Implantation-induced Compositional Disordering in GaAs/AlAs Superlattices

Ion implantation-induced compositional disordering or intermixing of III-V compound semiconductor superlattice (SL) structures has attracted increasing interest because of its application potential for microfabrication of unique optical and electronic devices. In contrast with dopant-diffusion-induced SL intermixing, ion implantation offers the versatility to have the disordering at a required depth with the desired electrical activation and high reproducibility. In the GaAs/AlAs system, it has been reported[9] that compositional disordering can be realized through ion implantation either with the electrically active implants, such as Zn and Si, or with electrically inactive implants, such as Kr, B, and F, or with lattice constituents, Ga, Al, and As. Oxygen ions are another type of promising species for the GaAs/AlAs system. As was shown earlier, oxygen ion implantation can induce semi-insulating effects in GaAs, and AlGaAs[10] as well. Recently, Bryan et al.[5] have demonstrated that oxygen ion implantation can simutaneously induce compositional disordering in AlAs/GaAs SLs. They have also found that a dose around $1\times10^{17}/cm^2$ is required for disordering to take place in 1 MeV oxygen ion implantation at room temperature. They noted that oxygen-implantation-induced disordering is not dependent on fast diffusion of the implants during the anneal, as is the case for Si implantation. Rather, the atomic mixing processing (*i.e.,* ion beam mixing and radiation-induced diffusion) occurring during implantation allows sufficient disruption of the disorder to produce partial disordering. In addition, there exists a sensitive temperature dependence during implantation as evidence is found that implantation at RT has more extensive disordering than that at elevated temperature.

Commonly, the LEIM (a few hundred keV range) has been utilized for the disordering process, in which the mechanisms are mainly due to implantation-induced lattice damage and defect diffusion. However, as we discussed at the beginning of the thesis, the HEIM (in MeV range) can provide many additional advantages, such as deep implantation, minimized surface damage, and electronic-ionization-correlated secondary effects. We present in the next section an investigation of compositional intermixing in AlAs/GaAs superlattices through MeV ion implantation at low temperature. It shows that, in addition to the direct lattice damage effect by nuclear collisions present at EOR of ions, the MeV-ion-induced electronic effect can also induce lattice intermixing.

3.4.1 Experimental Aspects

The sample examined in this study was a 1 μm-thick SLs grown by MBE on Cr-doped semiinsulating GaAs substrate. The superlattices are composed of 25 periods of AlAs(150Å)/GaAs(250Å) layers. Implantation was conducted with oxygen ion beams of 0.5 MeV and 2 MeV at a dose of $1\times10^{16} ions/cm^2$ with the target holder maintained at LNT. Subsequent annealing was at 650°C for 30 min on a graphite hot plate with the proximity covering format with an Argon gas flow. The

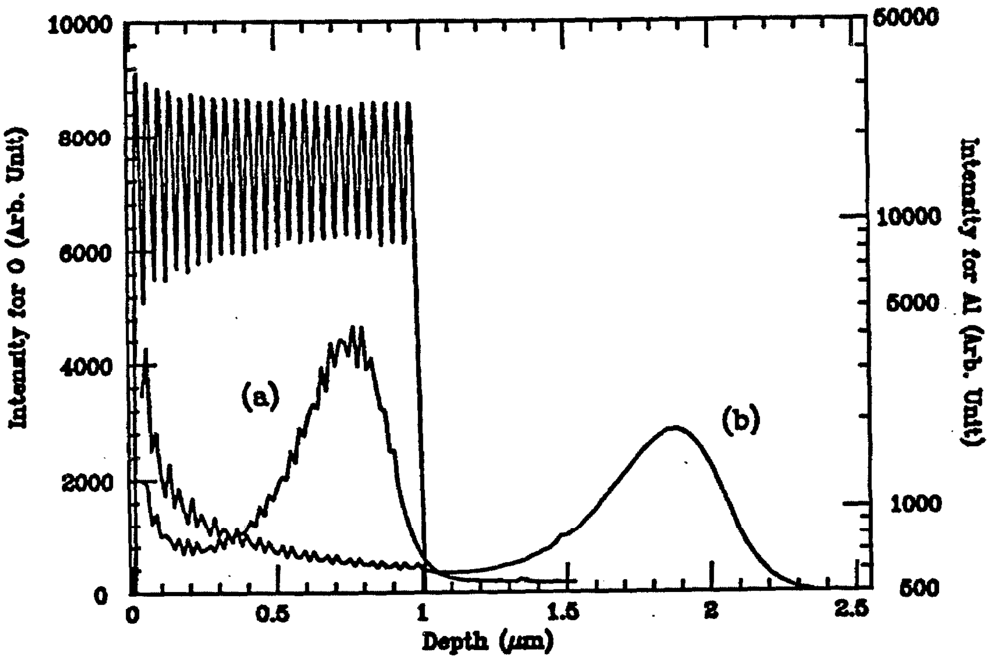

Figure 3.10 Al oscillations in AlAs/GaAs superlattices and oxygen profiles in (a) 0.5 MeV and (b) 2 MeV oxygen-ion-implanted AlAs/GaAs superlattices.

oxygen distribution and the degree of Al interdiffusion and layer intermixing were examined with SIMS at Bellcore Laboratory. 8 keV Cesium ions were employed as primary ions for oxygen profiling with a beam current of 100 nA, the scan width of 0.5mm, and a scan speed of 10 s/frame. For Al profiling, 15 keV oxygen ions were utilized with a beam current of 300 nA, the scan width of 0.5mm, and a scan speed of 4 s/frame.

3.4.2 Experimental Results

The SIMS profiles of ^{27}Al in the unimplanted sample and ^{16}O implants in implanted samples are shown in Fig 3.10. The oscillations of the Al signal with the peak-to-valley ratio of about 4.5 in the Al profiles represent the regular AlAs/GaAs superlattice structure. After being annealed at 650°C, the Al profile in an unimplanted sample (the SIMS profile is not plotted here) showed no difference. The irregular oscillation in oxygen depth profiles is due to the matrix effect in the SIMS measurement. Oxygen profiles mark the depth range of about 0.65 μm with FWHM of .3 μm for 0.5 MeV ions and of 1.65 μm and .5μm for 2 MeV ions. One should realize that 0.5 MeV oxygen ions are deposited within the SL layers, while 2 MeV oxygen ions are peaked at a place deep beyond the SLs. Thus, in the low energy case, the energy deposition and lattice damage in the SLs are controlled by the nuclear collision (nuclear spike) process; while in the high energy case, electronic ionization and excitation (electronic spike) is the dominant process during implantation.

The Al SIMS profiles of both as-implanted samples and implanted and annealed samples are monitored. In as-implanted samples, a slight Al interdiffusion was observed. The regular Al oscillation remains with the peak-to-valley ratio down to 4. Al interdiffusion at this stage is probably due mainly to nuclear knock-on induced lattice displacement during implantation, because the other diffusion processes have been minimized at LNT. The strong Al interdiffusion has been enhanced after high temperature annealing. The corresponding SIMS Al profiles are illustrated in Figure 3.11. There exist significant differences in these two samples. In the low energy implanted sample, the amplitude of Al oscillation has dramatically decreased with the peak-to-valley ratio down to 1.4, which indicates intermixing of AlAs and GaAs SL layers. Near the surface region the oscillation amplitude is nearly constant. However, in the region near the end of the SL layers, the peak value of Al oscillation has dropped further. This region, ranging from the 20th peak to the end, corresponds to the region where the implanted oxygen ions are deposited (comparing to the oxygen depth profile shown in Fig 3.10). This decrease indicates the significant impurity-related Al diffusion in this region due to the existence of implanted oxygen. In the high-energy-implanted sample, the peak-to-valley ratio of Al

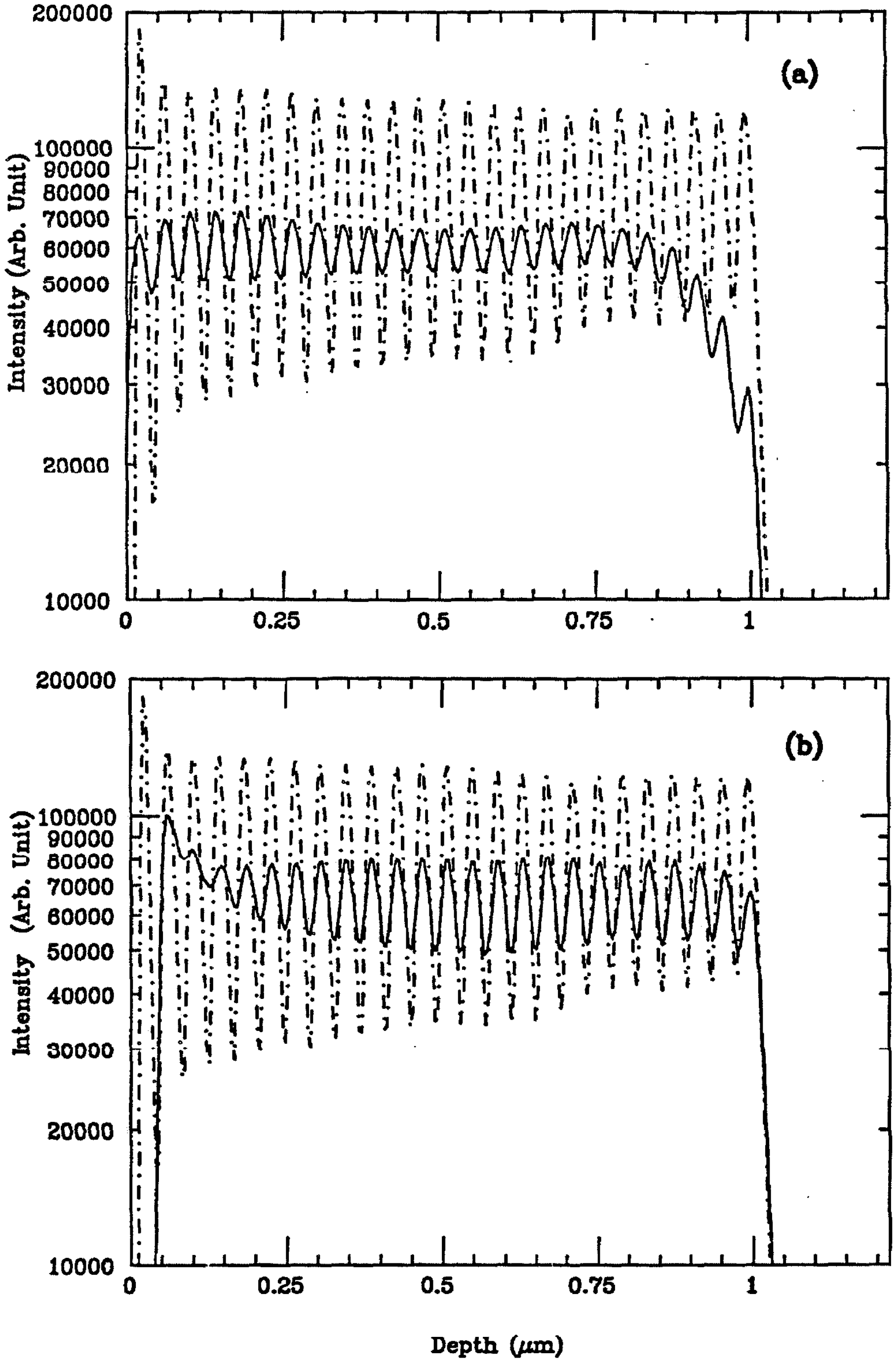

Figure 3.11 Al depth profiles in oxygen-ion-implanted and subsequently annealed AlAs/GaAs superlattices. a) 0.5 MeV, and b) 2MeV. The Al profile of the unimplanted sample is ploted in a dotted line for comparison.

oscillations decreases to 1.6, slightly higher than that in the low-energy-implanted sample. However, the amplitude remains very much steadier over SL layers, except for the anomalous distortion in a few layers at the top surface, which is due to the presence of surface oxygen introduced during the uncapped annealing process.

In brief, we have found that Al interdiffusion in AlAs/GaAs superlattices has taken place in both low and high energy implanted samples with subsequent high temperature annealing. Both the nuclear spike and the electronic spike can contribute to this process. In low energy implantation, the nuclear spike dominates and gives direct atomic displacement at the EOR of implants, which efficiently stimulates the Al interdiffusion. The electronic spike induces electronic ionization and distorts the lattice electronic configuration, which in turn enhances migration and diffusion of defects and displaced atoms, as well as Al atoms. In addition, low temperature implantation can be of help to this process by the freeze-in of lattice damage and minimizing the probability of in situ annealing.

3.5 References

1. C. Y. Wie, PhD thesis, Caltech (1985) unpublished.
2. T. T. Bardin, J. G. Pronko, F. A. Junga W. G. Opyd, A. J. Marinly, F. Xiong, and T. A. Tombrello, Nucl. Instr. Methods, B24/25 (1987) 548.
3. P. N. Favennec, G. P. Pelous, M. Bib-net, and P. Baudet, in *Ion Implantation in Semiconductors and Other Materials,* ed. B. L. Crowder (Plenum, New York) (1973), p. 621.
4. P. N. Favennec, J. App. Phys. 47, (1976) 2532.
5. R. P. Bryan, M, E. Givens, J. L. Klatt, R. S. Averback, and J. J. Coleman, J. Elect. Mat. 18(1) (1989) 39.
6. S. M. Sze, *Physics of Semiconductor Devices*, 2nd edition (John Wiley & Sons, New York) (1981), p. 31.
7. W. Wesch, E. Wendler, G. Gotz, and N. P. Kekelidse, J. Appl. Phys. 65(2) (1989) 519, and references therein.

8. O. W. Holland, M. K. El-Ghor, and C. W. White, Appl. Phys. Lett., 53 (1988) 1282.
9. Y. Hirayama, Y. Suzuki, and H. Okamoto, Jap. J. Appl. Phys. 11(1985) 1498. And also see ref. 5 and references therein.
10. S. J. Pearton, M. P. Iannuzzi, C. L. Reynolds Jr., and L. Peticolas, Appl. Phys. Lett. 52 (1988) 395.

Chapter 4

RADIATION-INDUCED DEFECTS AND STRAIN IN III-V COMPOUND SEMICONDUCTORS

4.1 Introduction

As was shown in the last two chapters, radiation-induced lattice strain in semiconductor crystals is a highly interesting and important subject in the study of ion damage in ion implanted semiconductors — especially binary compounds. The phenomenon of lattice expansion by ion implantation in many semiconductor crystals was first observed over 30 years ago. In 1957, Gonser and Okkerse[1] noticed lattice parameter expansion in GaSb and InSb induced by MeV deuteron irradiation. Later, Kleitman and Yearcian[2] comfirmed this result by x-ray diffraction. A small lattice expansion was also observed in 9 MeV deuteron-implanted germanium at low temperature by Vook and Balluffi[3] and by Simmons[4]. Whan and Arnold[5] noticed lattice expansion in 400-keV Xe ion-implanted GaAs and Si crystals. Using the sensitive x-ray rocking curve technique, similar results have been observed in keV proton- or argon- ion-implanted GaAs, Si and Ge crystals[6], and MeV-Cl, -O, or -C-ion-implanted GaAs, GaP, and GaInAs.[7–9] The magnitude of this kind of strain is usually very small, one percent or less. It is believed that ion-lattice collisions induce point defects that are responsible for the lattice strain generation. Wie and his co-workers[8] have given a model of single ion-lattice collisions, and concluded that the surface lattice strain saturation induced in MeV ion implanted GaAs was due to generation of an equilibrium population of antisite defects by a combination of collision damage and electronic ionization. However, in order to get a better understanding of radiation-induced strain in crystalline semiconductor materials, we have extended this work to InP, AlGaAs, CdTe, and LiF crystalline systems. In the case of InP, we have observed negative strain induced in MeV-ion-implanted crystals, which was presented in Chapter 2. In all the other cases, even in keV ion implanted InP, positive strain appears after implantation. Most recently, Ascheron et al.[10] have reported that in InP crystals, there is a tendency for the high energy proton irradiation (1.2 MeV used) to produce a negative volume change, which differs from a positive volume change produced by low energy protons (300 keV). This gives us an interesting puzzle, because InP is a typical III-V compound crystal. Based on the experimental results we obtained and by considering the character of the defects, we suggest that it is the different mechanism of generation and relaxation of primary point defects during ion implantation that induces the lattice strain and determines its sign and magnitude.

In this chapter, the general configuration and migration of point lattice defects in binary compound semiconductors will be described first. A model for the generation, recombination, and diffusion of the primary defects in the crystals by ion-lattice collisions as well as by defect interaction processes is then presented. This model predicts the defect population and saturation behaviour for high dose ion irradiation. Based on the experimental results we presented earlier as well as those reported by others, a possible mechanism for lattice strain generation and saturation in III-V compound semiconductors obtained from this model is proposed and discussed in Section 4.4.

4.2 Characteristics of Ion Implantation Induced Defects in III-V Compound Semiconductors

4.2.1 Configurations of Point Defects

Defects in a semiconductor crystal have important effects on the electronic, optical, and mechanical properties of the material. Defects are defined by their chemical natures and their geometrical configurations. Primary point defects can be vacancies, interstitials, and substitutional impurities. Various kinds of defect complexes are formed by the association of these primary defects, such as a Frenkel pair when a vacancy is closely associated with a self-interstitial, a high-order vacancy cluster where two or more vacancies occupy closest neighboring lattice sites, and substitutional-vacancy complexes. In compound semiconductors, all the lattice sites are not equivalent, and a large variety of defects can exist. In binary compound semiconductors, there are two different sublattices where each can have its own primary defect types. An antisite defect is formed by an atom of one sublattice placed in the other sublattice site. Complexes of intrinsic defects, impurities, and high order vacancies can also be envisaged. Two-dimensional schematic representations of these various types of point defects in compound crystals are illustrated in Figure 4.1.

In a tetrahedral coordinated III-V compound semiconductor lattice, four heteropolar A^{III}-B^{V} bonds are broken in order to create a vacancy-interstitial pair (see Fig. 4.2a). The undistorred "ideal" monovacancy has four dangling bonds centrally directed into the vacancy. Depending on the charge occupancies on these sp^3 hybrid dangling bonds, they can form new bonds, leading to lattice relaxation and distortion and preserving the high local symmetry[11]. For example, when there is one electron per dangling bond (i.e., for the neutral vacancy V^o), by electron pairing two nearest neighbour dangling bonds pull together. They form two new saturated bonds leading to local distortion (see Fig 4.2b). When an electron is missing (i.e., for the positive vacancy V^+), one of these two bonds is weakened since it contains only one electron. The distortion is thus different from that in the case of V^o (Fig. 4.2c). There may exist another particular case for a possible distortion, called a "split-vacancy" configuration (Fig. 4.2d), where one neighbour of the vacancy is displaced halfway between its original position and the center of the vacancy.

The "ideal" interstitial has also four sp^3 hybrid dangling bonds pointing out of the center of the interstitial with all surrounding atoms at their perfect positions

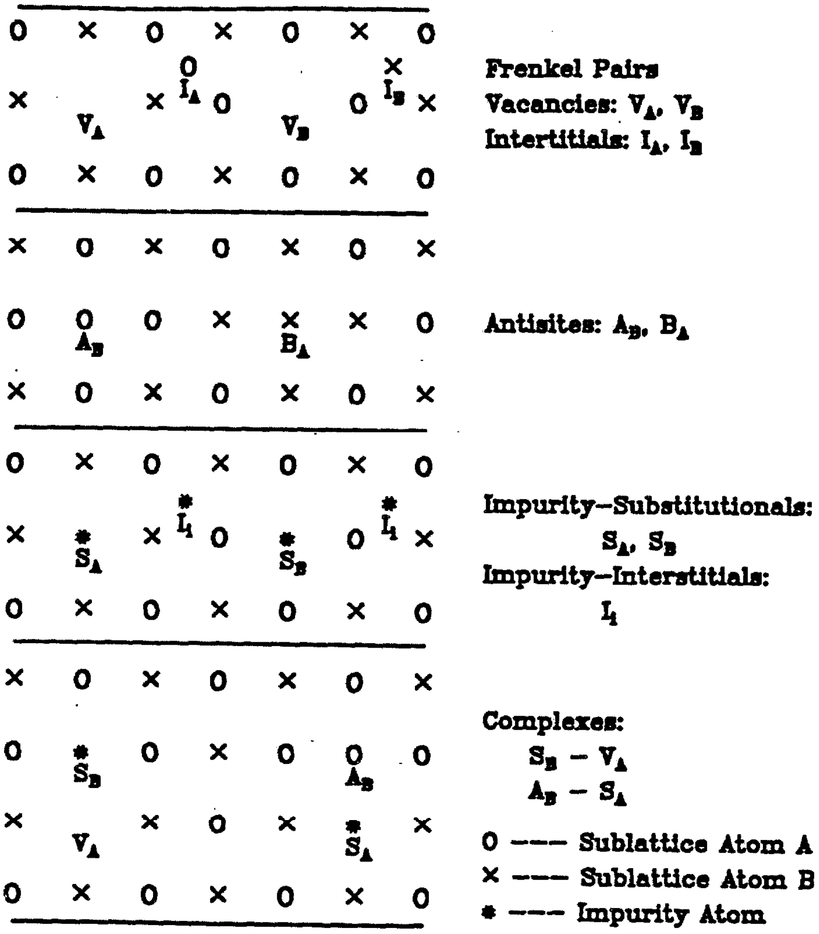

Figure 4.1 Schematic of a two-dimensional representation of some point defects and complex defects in a binary compound semiconductor.

in saturated bonding. So it is impossible to decided a *priori* what are the stable sites for an interstitial atom. However, if an interstitial exists, its total energy with all surrounding atoms will be in an extremum. It is thus reasonable to consider that some of these highly symmetric sites are stable interstitial positions. Because of the symmetry of the lattice, there may be several equivalent position per unit cell. The "bond-centered" configuration as shown in Fig 4.3a is one possible highly symmetric structure for interstitials, where one original sp^3 bond is broken and and interstitial

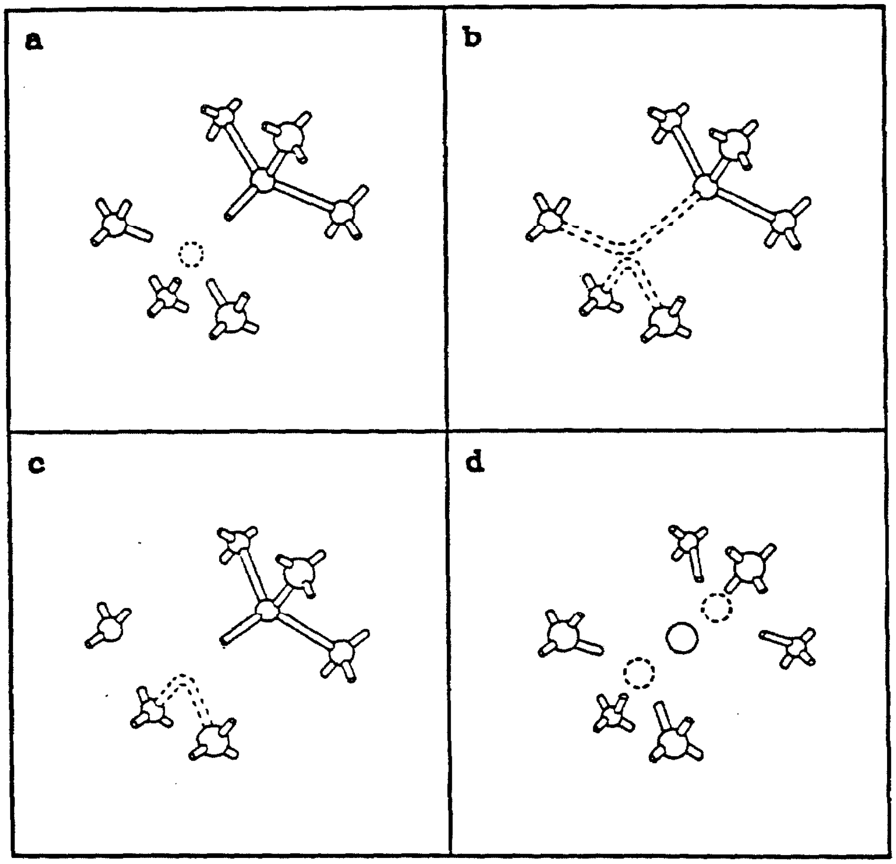

Figure 4.2 The vacancy in tetrahedral coordinated crystalline lattice. (a) As-created vacancy with four sp^3 dangling bonds; (b) Neutral vacancy V^0 with one electron per dangling bond, two new bonds are formed leading to local distortion; (c) Positive vacancy V^+, missing one electron, one of these new bonds is weakened since it contains only one electron. The distortion is thus different from that in the case of V^0; and (d) Split vacancy, where one neighbour of the vacancy is displaced half way between its original position and the center of the vacancy. (Taken from ref. 11.)

is inserted in the center to form two new bonds. The hexagonal and tetrahedral sites depicted in Fig. 4.3 are the sites of highest symmetry in the III-V compound crystalline lattice, where an interstitial sits at the center of the lattice with weak bond-like connections to the neighbour lattice atoms. Once again, as in the case of

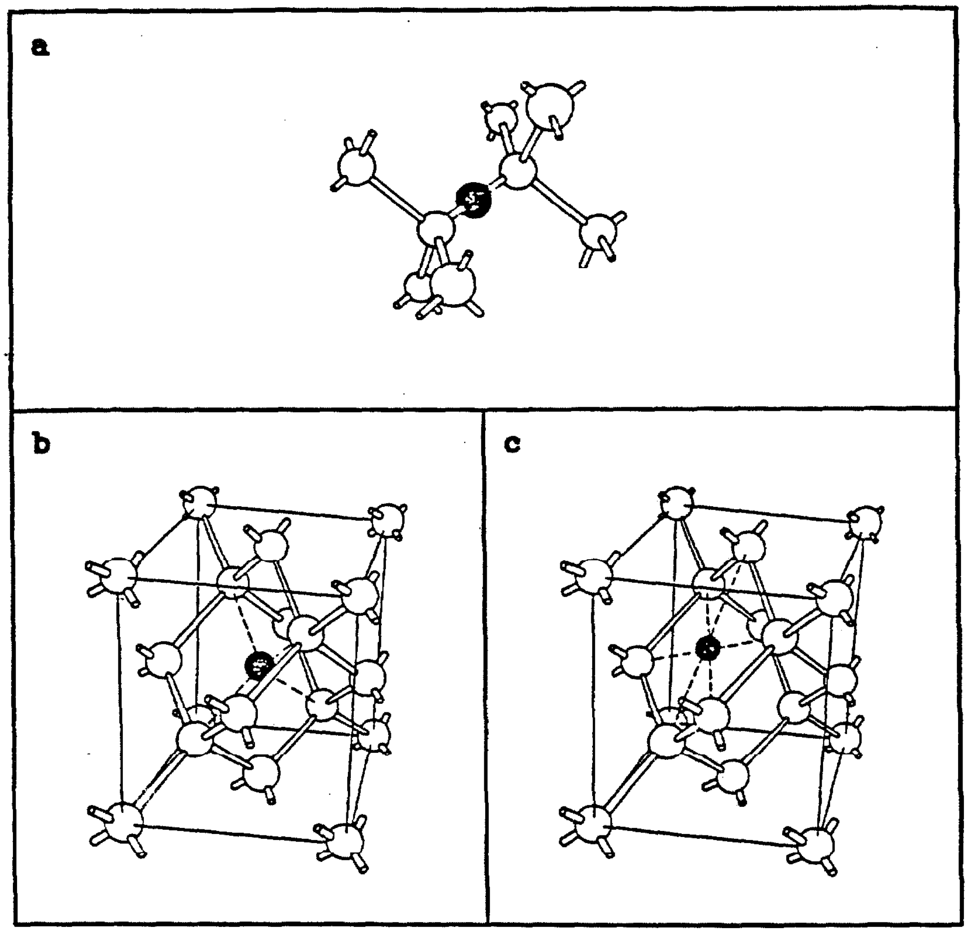

Figure 4.3 The possible highly symmetric configurations for interstitials in a tetrahetral coordinated lattice: (a) bond-centered, (b) tetrahedral, and (c) hexagonal. (Taken from ref. 11.)

a vacancy, the introduction of an interstitial induces a relaxation and distortion of the lattice surrounding it. The type of configuration that the interstitial chooses depends upon its ability to make bonds with its neighbours and therefore can change dramatically with its charge state.

In an antisite defect, four heteropolar bonds (A-B) are replaced by four homopolar bonds (A-A or B-B). The strength of the new bond formation relies on the change of atomic size (geometry), electronegativity (chemical binding) and the

Table 4.1. Enthalpies of antisite defect formation in III-V compound semiconductors (the unit in eV).
E(A_B) in the first row and E(B_A) in the second row.

$A^{III}B^{V}$	P	As	Sb
Al	0.60	0.30	0.02
	0.50	0.45	0.36
Ga	0.68	0.35	0.08
	0.38	0.35	0.32
In	0.89	0.52	0.27
	0.42	0.33	0.27

* The data were taken from Ref. 12.

charge state (electrical) of two sublattice atoms. Table 4.1 lists enthalpies of antisite defect formation in III-V compound semicondictors[12]. Comparing with the data on atomic size and electronegativity listed in Table 2.1, one realizes that they are closely associated with each other. As the ratio of the atomic size of element A to element B increases, E(A_B) tends to increase, and E(B_A) decreases. For GaAs and InSb, E(A_B) is the same as E(B_A) because the atomic sizes and electronegativities for element A^{III} and element B^{V} in these compounds are quite close. InP has the largest value of E(A_B) because it has the largest value in atomic size ratio and the largest electronegativity difference, which implies that it is harder to form A_B antisite in InP than is the case in other III-V compounds. Taking the charge state of antisite defects into account, the enthalpies of antisite defect formation would be much higher when the charge state goes to neutral. Dobson and Wager[13] have given calculated values. Small distortion would also be associated with antisite defects when they relax. Similar to vacancies or interstitials, the direction depends on the change of bond strength. In the defect complexes, the configurations are just the combinations of primary point defects. The same is true for the lattice relaxation.

4.2.2 Defect Interaction and Migration

Defect migration is also an important feature for defect stability. It has been shown in many theoretical studies and by experimental results that the point defects, especially interstitials, in Si and Ge elemental semiconductors are very mobile at temperatures even below room temperature. It is expected that this would be more pronounced in III-V compound semiconductors due to the weaker binding and the binary nature in the compound system. It is the defect migration process that enhances the interaction of defects (intrinsic and extrinsic), giving rise to more complex defects as well as correct sites through recombination. For instance, a mobile vacancy can be trapped by the the doping impurity to form a vacancy-impurity complex center. It may tend to aggregate, as temperature increases to form divacancies, trivacancies, and so on. The interstitial can be mobile and trapped at grain boundaries, plastic zones, and extended defect complexes. When the number of defects in a complex is large, they tend to arrange themselves into high-dimensional defects (lines, rings, or platelets). In III-V compound semiconductors, due to the binary nature, many more spacially complex defects can be formed. An antisite defect is the simplest kind of complex of defect interaction that results, where a "wrong" recombination occurs. Due to rearrangement of lattice atoms in a complex defect or the change of sublattice atomic type in antisite defects, lattice relaxation and distortion may also be introduced in the lattice structure.

There are several mechanisms for point defect diffusion through a lattice, depending on the characteristics of the defects. Generally speaking, in order to move through the lattice they have to pass through some kind of potential barrier, the corresponding energy of which is normally described as the activation energy ΔE. The diffusion probability is thus proportional to $\exp(-\Delta E/kT)$. An interstitial (self or impurity) migrates by hopping directly from its original interstitial site to

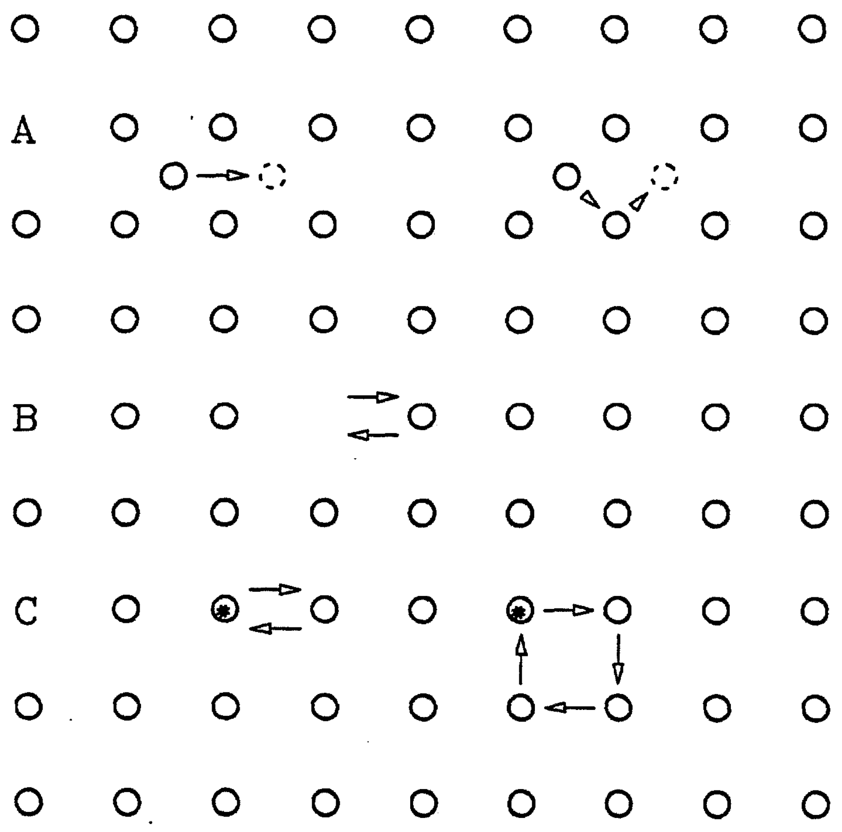

Figure 4.4 Schematic illustration for defect diffusion mechanisms. (a) Interstitials, (b) Vacancies, (c) Impurity substitutionals.

a neighbouring equivalent one, or exchanging with a lattice atom that is, in turn, displaced into a new interstitial site. These are illustrated in Fig. 4.4a. The later process has involved two actions — breaking old bonds and forming new bonds, so its activation energy is a sum of the energies, while the first process of the migration only requires a jump over a barrier existing between two neighbouring equavilent interstitial sites without breaking any bonds. Thus, the first process is most likely and is commonly referred to as the interstitial mechanism for defect diffusion. For a vacancy, an easy way for the migration to occur is to exchange with one of the nearest neighbouring site atoms, called the vacancy mechanism (Fig. 4.4b). This is actually a combination of the vacancy creation and the defect recombination processes. In a single elemental semiconductor crystal it just switches the defect site without creating a new defect; while in a compound crystal, it results in the formation of a new antisite defect and a new vacancy. It is probable that the activation energy for defect diffusion in the vacancy mechanism is thus much higher than that in the interstitial mechanism. Substitutional defects can migrate by hopping from the original site to a neighbouring substitutional site through a direct exchange or through an indirect exchange, as illustrated in Fig. 4.4c. Because the substitutional defect is originally in a very stable state, its migration is less probable even than the vacancy mechanism. It is also noted that the charge state of the defect is one of the main factors that can play an important role in defect migration processes (for instance, ionization enhanced defect migration in ion implanted crystals).

4.2.3 Defect Relaxation and Lattice Strain Build-up

As we have already mentioned in Section 4.2.1, the introduction of a point defect in a crystalline material induces displacements of the lattice atoms that surround it. When the symmetry of the lattice is conserved, these displacements are said to result in a relaxation. When the symmetry is reduced the induced displacements are referred to as distortion. For the radiation damage in III-V compound semiconductor, due to the complex nature of the defects, both relaxation and distortion can be involved. With respect to their short-range order property a significant displacement will only affect the first few nearest neighbour atomic shells on a small scale with the strength decaying exponentially. However, such small displacements of the neighbour atoms of a defect can direct inward or outward, depending on the character of defects. Figure 4.5 gives a sketch in a two-dimensional view of imaginable force fields and the relaxed state for *isolated* vacancy and interstitial systems, respectively. In a vacancy, one atom is missing, leaving an empty atomic space with four dangling bonds on the surrounding neighbour atoms. There exists a highly attractive force field, called the negative-U potential[14,15]. As a consequence, the surrounding atoms of the vacancy move towards the center. They are

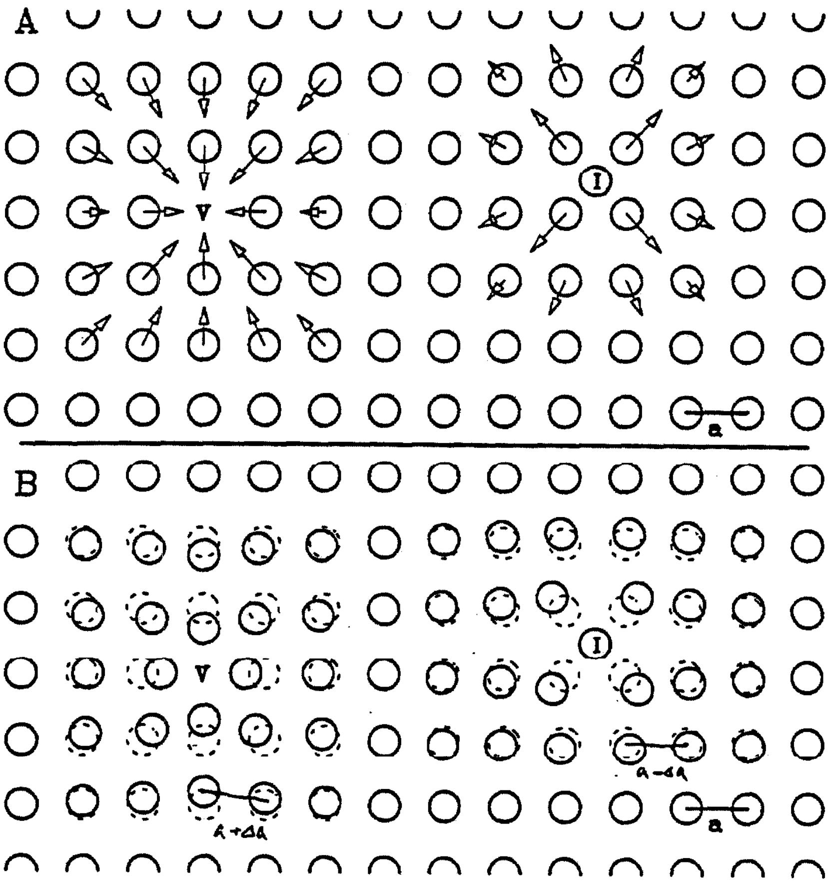

Figure 4.5 A two dimensional view of (A) imaginable force fields and (B) relaxed metastable states for a vacancy (left-hand side) and an interstitial (right-hand side), respectively.

pulled together in pairs, a distortion tending to rebond the four dangling bonds into two unbroken ones with regard to the charge state of the vacancy. These can be envisaged in many different configurations of vacancies (e.g., V^0, V^+, and the split vacancies), which are shown in Fig. 4.2. In an interstitital defect system, one extra atom is jammed into the perfectly bonded lattice with four dangling bonds, creating a highly repulsive potential (the positive-U potential[16]) in the lattice and thus it is in an unstable state. The surrounding neighbour atoms repel the interstitial atoms and push outwards to balance this potential until a metastable state is reached. These can be imagined in the configuration shown in Fig. 4.3. In either of these two cases the lattice spacing changes, but the volume conserves, which is called the Jahn-Teller effect[11]. Similar effects are expected to occur in antisite defects and impurity-substitutionals, where the direction and magnitude of displacements depend on the differences in atomic size and electronegativity of the substitutional atoms, as well as the charge state of the defect. For instance, in InP crystals, the In antisite (In atom takes P site) may induce outward displacement on first neighbouring In atoms, because an In atom has a larger radius size and smaller electronegativity than the original P atom in the site. In GaAs, antisites may not give significant distortion to the lattice because Ga and As have similar atomic sizes and electronegativities. Combinations of all the effects can appear in complex defect systems.

Coherent relaxation in a damaged crystal leads to the build-up of lattice strain to the point where it is detectable, and changes the volume of the implanted layer as well. As was discussed above, the sign of the lattice strain and therefore this volume change is closely associated with the lattice defects and their population in the damaged crystal. If the population of vacancy-type defects is predominant over the others, the lattice relaxation leads to inward displacement of the atoms in the neighbourhood of the defect, causing the lattice spacings to be extended. Thus, the coherent strain appears positive. In contrast, if interstitial-type defects dominate, the outward displacement in lattice distortion around the defect will cause the lattice spacing to shorten, and lattice strain appears with the negative sign (see Figs. 4.4 and 4.5). In certain cases the lattice strain can lead to volume changes on a microscopic scale, but they are not expected to be associated fully with each other, because the lattice relaxation and distortion may originate from different effects and different lattice defects. Strain can occur without volume changes of the strained layer, e.g., by elongations of lattice atoms around vacancies due to the Jahn-Teller effect as we disscused before. Changes in volume can occur without increases in mean interplanar spacing, e.g., by changes of the lattice coordination number, which changes the density of the crystal.

4.3 A Model for Point Defect Generation in Ion Implanted III-V Compound Semiconductors

Defects or impurities are introduced into semiconductors, intentionally or unintentionally, during the growth process or during the following heat treatment. Ion irradiation is another efficient way for impurity introduction and defect creation, where the concentration, the distribution, and (to some extent) the nature of defects can be under precise control. Point defects generated during ion irradiation in compound semiconductors are of interest to us as they are an indication of lattice damage and a parameter for phase transformation.

As we will discuss in the next chapter, during ion implantation the ion-lattice interaction involvs two major processes: electronic ionization at high energies after the energetic ions enter in the target (electronic spike) and the nuclear displacement collision cascade at the low energies before the ions stop (nuclear spike). Electronic ionization changes the lattice charge states without causing direct effects to lattice structures. Direct nuclear collisions cause recoil of lattice atoms, resulting in the creation of Frenkel pairs of self-interstitials (N_I) and vacancies (N_V) from the two types of sublattice sites (a and b), thus giving direct lattice damage to the target crystal. One can imagine that for a defect being produced by an energetic ion, the atom is removed from the lattice site with an excess momentum, and vacancies are surrounded by instability zones within which the knocked-out atom cannot be stabilized. If the momentum of the recoil atom is somewhat higher, the atom may depart from its site to a distance of several lattice spacings, forming isolated vacancies and interstitials. Because ion-lattice interaction often results in cascade collisions, defect clusters are usually nucleated. Defect migration and interaction can also be simultaneously enhanced by the ionization process during irradiation. As a result of defect interaction, there are the "self" recombinations of an interstitial and a vacancy from the same type sublattices to reform the correct sites (N_C), and the formation of antisite defects (N_A) by the possible "wrong" recombination of an interstitial of one element type with a vacancy of another type. Due to local stoichiometrical distortion and electrical charge state change throughout ionizations, the implantation-induced interstitials can keep diffusing away until trapped by defect sinks at the surface, grain boundaries, and the amorphous zone. Taking all these possibilities into account, we consider a unit volume in which ion-lattice displacement collisions, defect interaction, and defect diffusion are taking place; then we may write a chemical rate equation describing the defect production as well as changes of correct lattice sites with the implant dose (D). Let $X = N_V/N_0, Y = N_I/N_0, U = N_A/N_0, W = N_C/N_0$, and $t = D/N_0$, where N_0 is the total number of sublattice sites in the crystal, and use letters a, b, C, and A for subscripts for A and B sublattices, correct sites and antisites, respectively. The rate equation can be written as:

$$\frac{dX_a}{dt} = \overbrace{g_{Ca}W_a + g_{Aa}U_a}^{\textbf{generation}} \overbrace{- \gamma_{Ca}X_aY_a - \gamma_{Aa}X_aY_b}^{\textbf{recombination}} \overbrace{- \alpha_a X_a}^{\textbf{diffusion}}; \tag{1.1}$$

$$\frac{dX_b}{dt} = g_{Cb}W_b + g_{Ab}U_b - \gamma_{Cb}X_bY_b - \gamma_{Ab}X_bY_a - \alpha_b X_b; \tag{1.2}$$

$$\frac{dY_a}{dt} = g_{Ca}W_a + g_{Ab}U_b - \gamma_{Ca}X_aY_a - \gamma_{Ab}X_bY_a - \beta_a Y_a; \tag{1.3}$$

$$\frac{dY_b}{dt} = g_{Cb}W_b + g_{Aa}U_a - \gamma_{Cb}X_bY_b - \gamma_{Aa}X_aY_b - \beta_b Y_b; \tag{1.4}$$

$$\frac{dU_a}{dt} = -g_{Aa}U_a + \gamma_{Aa}X_aY_b + \alpha_a X_a; \tag{1.5}$$

$$\frac{dU_b}{dt} = -g_{Ab}U_b + \gamma_{Ab}X_bY_a + \alpha_a X_b; \tag{1.6}$$

$$\frac{dW_a}{dt} = -g_{Ca}W_a + \gamma_{Ca}X_aY_a; \tag{1.7}$$

$$\frac{dW_b}{dt} = -g_{Cb}W_b + \gamma_{Cb}X_bY_b. \tag{1.8}$$

In equations 1.1 - 1.4, the first two terms describe the defect generation from correct sites and antisites, where the $g_{(C,A)(a,b)}$ are the defect generation coefficients for sublattices (A and B), which correspond to the interaction cross section between implants and sublattice atoms A and B. The next two terms in the equations account for defect recombination to correct sites and antisites, the recombination coefficients $\gamma_{(C,A)(a,b)}$ being the corresponding defect interaction cross sections. The last term was introduced for defect diffusion with different diffusion coefficients α and β, for interstitials and vacancies, respectively. As we discussed in the last section, interstitial diffusion mainly follows the interstitial diffusion mechanism. Interstitials diffuse out of the implant-lattice interaction region, giving no contribution to the new defect generation, while vacancies follow the vacancy diffusion mechanism, giving a contribution to antisite defect population. This has been taken into account in equations 1.5 and 1.6. In the damaged region, the total number of atoms is not conserved due to the diffusion of defects. However, the conservation of the total number of sublattice sites holds, giving:

$$X + U + W = 1; \tag{1.9}$$

$$\frac{dX}{dt} + \frac{dU}{dt} + \frac{dW}{dt} = 1. \tag{1.10}$$

Taking a special example we first consider the GaAs system. Because two sublattice atoms (As and Ga) are very close in atomic number, atomic mass, and chemical binding energy, we neglect the difference between antisite and correct site sublattices; thus, all coefficients for atom A are equal to those for atom B. This limiting case is just the same as for a single element crystal. Then, the group of equations (eqs. 1.1—1.8) can be simplified to:

$$\frac{dX}{dt} = g(U + W) - (\gamma_C + \gamma_A)XY - \alpha X, \tag{2.1}$$

$$\frac{dY}{dt} = g(U + W) - (\gamma_C + \gamma_A)XY - \beta Y, \tag{2.2}$$

$$\frac{dU}{dt} = -gU + \gamma_A XY + \alpha X, \tag{2.3}$$

$$\frac{dW}{dt} = -gW + \gamma_C XY. \tag{2.4}$$

Setting $U+W = Z$ (which represents the filled sites) and $\gamma_C+\gamma_A = \gamma$, the equations can be rewritten as:

$$\frac{dX}{dt} = g(1-X) - \gamma XY - \alpha X; \tag{3.1}$$

$$\frac{dY}{dt} = g(1-X) - \gamma XY - \beta Y; \tag{3.2}$$

$$Z = 1 - X. \tag{3.3}$$

This is a set of second-order, nonlinear differential equations for the variables X and Y. Comparing to the model proposed by Wie et al., one can see that additional diffusion terms have been introduced in our model that play a major role in determining the predomination of primary defects and the lattice strain sign in radiation damaged crystals.

Consider a simple case, where $\alpha = \beta$, which implies that interstitials and vacancies have the same diffusivities. Then, $X = Y$ under the initial conditions $X(0) = Y(0) = 0$. Thus, one needs only to solve for X from the equation

$$\begin{aligned}\frac{dX}{dt} &= g - (g+\alpha)X - \gamma X^2,\\ &= \gamma\left[\frac{(g+\alpha)^2 + 4\gamma g}{4\gamma^2} - \left(X + \frac{g+\alpha}{2\gamma}\right)^2\right].\end{aligned} \tag{4}$$

By drawing a phase diagram, as shown in Figure 4.5, we can immediately find the limiting behavior of the defect population fraction of interstitials and vacancies. At low dose ($X \to 0$), $\frac{dX}{dt} \to g$; then

$$X \simeq gt. \tag{5.1}$$

At high dose, the X goes to a saturation state ($\frac{dX}{dt} = 0$), then

$$X_{max} = \frac{[(g+\alpha)^2 + 4g\gamma]^{1/2} - (g+\alpha)}{2\gamma} \tag{5.2}$$

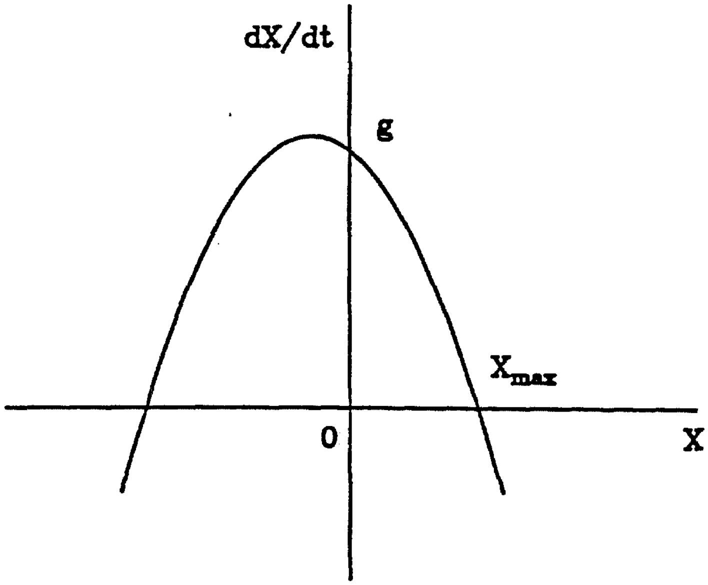

Figure 4.6 Phase diagram for point defect production by ion implantation in GaAs, according to equ. 4.

For $0 \leq X \leq 1$ and $X(0) = 0$, we can give the solution for equ. 4 as:

$$X(t) = X_{max}\left\{1 - \frac{2 + \frac{g+\alpha}{\gamma X_{max}}}{\left(1 + \frac{g+\alpha}{\gamma X_{max}}\right)e^{(g+\alpha)t} + 1}\right\}. \tag{5.3}$$

Its limitation indeed gives the results of (5.1) and (5.2).

For $\alpha \neq \beta$, we can draw a solution for the limiting cases. At the very low dose case,

$$X \simeq Y \rightarrow gt. \tag{6.1}$$

At the saturation case, by setting $\frac{dX}{dt} = \frac{dY}{dt} = 0$, we obtain

$$Y = \frac{g+\alpha}{2\gamma}\left\{\left[1 + \frac{g\gamma\alpha}{\beta(g+\alpha)^2}\right]^{\frac{1}{2}} - 1\right\}, \tag{6.2}$$

$$X = \frac{\beta}{\alpha}Y = \frac{\beta}{\alpha}\frac{g+\alpha}{2\gamma}\left\{\left[1 + \frac{g\gamma\alpha}{\beta(g+\alpha)^2}\right]^{\frac{1}{2}} - 1\right\}. \tag{6.3}$$

Therefore, for $\beta > \alpha$, we arrive at a conclusion that $X > Y$. This implies that the vacancy population is greater than the interstitial population in the materials where the interstitial diffusion mechanism dominates, which is true in most practical cases. This has also told us that implantation generates defects with a rate of g, but the point defect diffusion controls the defect population fraction in the damaged region, and in turn it may determine the radiation-induced lattice strain.

In general, such as in the InP system, the sublattices are different. The characters of the correct sites and antisites are not the same. Then, the case described by equations 1.1 - 1.10 is more complicated. Solving this set of equations is rather difficult, however, with the initial conditions of X=Y=U=0 and W=1 at t=0, we can find limiting cases for defect generation. In a low-dose limit, one finds that:

$$\frac{dX_a}{dt} = \frac{dY_b}{dt} = -\frac{dW_a}{dt} = g_{C_a}; \tag{7.1}$$

$$\frac{dX_b}{dt} = \frac{dY_a}{dt} = -\frac{dW_b}{dt} = g_{C_b}. \tag{7.2}$$

These imply that:

$$X_a = Y_b = g_{C_a}t; \tag{8.1}$$

$$X_b = Y_a = g_{C_b}t; \tag{8.2}$$

$$W_a = 1 - g_{C_a}t; \tag{8.3}$$

$$W_b = 1 - g_{C_b}t. \tag{8.4}$$

For the population of antisite defects, the second order dependence on t has to be considered. By the results in eqs. 3.1 to 3.4, from eqs. 1.5-1.6, one obtains

$$U_a = \frac{1}{2}\alpha_a g_{C_a} t^2, \tag{3.5}$$

$$U_b = \frac{1}{2}\alpha_b g_{C_b} t^2. \tag{3.6}$$

It shows that the antisite population is closely associated with defect creation from correct sites and vacancy diffusion. In a high-dose limit, all of the defect production rates approach zero. One can solve the corresponding algebraic equations to get the defect population fraction for the saturation state.

4.4 Mechanism of Lattice Strain Generation in Semiconductors by MeV Ion Implantation

In this section, the mechanism for lattice strain generation in MeV ion implanted compound semiconductors is proposed, based on the characteristics of lattice defects and the model of defect generation by ion implantation, presented in the previous two sections.

Several models proposed early for the mechanism of ion irradiation induced lattice strain in semiconductors can be found. Based on the observation, by x-ray diffraction, of radiation damage in GaSb, which was bombarded with 12 MeV deutrons at liquid nitrogen temperature, Gonser and Okkerse[1] suggested that by thermal spikes introduced under ion irradiation the damaged region is present in a liquid-like lattice coordination —markedly different from the matrix configuration. With the appearance of the spikes, Frenkel pairs are generated in the matrix material, resulting in an expansion of the lattice, but the crystal as a whole, which includes the high density spikes, decreases in volume. Vook and Balluffi[3] proposed several models for the structural configuration in 10.2 MeV deuteron-irradiated Ge crystals. They eliminated isolated vacancies and interstitials distributed homogeneously throughout the entire volume as the sole effect produced by irradiation and indicated that randomly distributed and finely mixed interstitial and vacancy clusters as well as displacement-spike-induced different phase transformed structures are mostly responsible. Interstitial and vacancy clusters could be produced directly up on ion bombardment, or could be formed by the grouping together of defects by diffusive motion after bombardment. The damaged region may be constructed by atomic rearrangement and the addition or substraction of mass, thereby causing a relatively uniform strain. Speriosu et al.[5] has found in keV ion implanted Si and Ge that the radiation induced strain increases linearly with dose upto the amorphization threshold, which closely corresponds to the linearity of point defect generation up on the ion dose. Nonlinearity of strain generation in GaAs consists of the creation of extended defects along with a transition from elastic to plastic behaviour. The results clearly indicate the different nature of ion damage in compound semiconductors from the case of single element crystals. Detailed studies of MeV ion implanted GaAs by Wie et al. have been made with x-ray rocking curve analysis. The model they present based up on the experimental results describes phenomenologically the connection of surface lattice strain with ion nuclear stopping power and electronic stopping power at the sample surfaces. Briefly summarized, all these models have given phenomenologically a close connection between ion-implantation-generated defects and the lattice strain or volume changes in the damaged regions. However, the interpretation for strain sign and its profile with depth remains unclear.

As we discussed in the sections above, ion bombardment of crystalline semiconductors creates lattice defects (point or cluster) by ion-lattice displacement collisions and induces the crystalline-to-amorphous phase transition when the dose threshold is reached. Defect interaction and diffusion control the redistribution of defect population as we predicted. Defect complexes and high dimensional defects can also be formed. To reach a steady state, the defects relax, causing the displacement of atoms around defects. The displacement direction depends up on the characteristics of the defects. Coherent distortion and lattice displacements lead to lattice strain build-up on a macroscopic scale. Thus, by taking the detailed features of each type defect into account and following the model of defect generation in ion irradiated crystals as well as the experimental results, we propose here that the lattice strain in ion implanted crystals is due to implantation-created lattice defects in the damaged region. The sign and depth profiles of the lattice strain are determined by distribution of the dominant defects. If vacancy-like defects dominate, the crystal is under expansion, and positive strain appears. When the crystal is filled with interstitial-like defects as the majority, negative strain would occur. The strain magnitude is controlled by the degree of lattice damage and the material's elastic properties. In the lightly damaged region the strain builds up as the defect density increases. Assume that, at the depth, x, the defect concentration of the ith kind defect is $f_i(x)$, then the local lattice strain, $\epsilon(x)$, induced by the defects can be described as:

$$\epsilon(x) = \Sigma k_i f_i(x),$$

where k_i is the strain induction coefficient for defects of the ith kind. Its sign and magnitude are determind by characteristics of the defects, as we discussed above. The profile of the defects, $f_i(x)$, is directly associated with the nuclear energy deposition of incident ions with the maximium depth, x_{max}, determined by the ion stopping range. Hence, before the defect concentration reaches the phase transformation level, the integrated strain is the same as the surface swelling, and is expressed as:

$$\triangle X = \int_0^{x_{max}} \Sigma k_i f_i(x) dx.$$

In the phase transformed region (crystalline to amorphous, or elastic to plastic), the lattice symmetry and crystallinity are totally destroyed, providing a plastic region to trap the incoming diffused defects. At the boundary of this region, both defect diffusion and defect relaxation reach an equilibrium state; thus, the strain saturation appears when a uniform amorphous layer forms. In this case, the surface swelling may not be equal to the total integrated strain.

There may exist a distinction between implantation by keV ions and MeV ions. MeV implants can be placed a few microns deep in the sample, while keV ions damage the crystal surface to a depth of a few thousand angstroms, providing a short length for defect diffusion. Thus, in keV ion implanted samples, due to the fast diffusion of interstitials leaving vacancies behind in the crystal, positive strain always appears. In MeV ion implantation, nuclear spikes and collision cascades cause the structural damage directly, while electronic spikes and ionization enhance the defect diffusion and interaction. These make the process much more complicated and significantly different from the case of keV ion implantation where the nuclear damage is the sole process involved.

In single element crystals like Si and Ge, interstitials and vacancies along with their complexes are the major types of defects introduced by ion implantation.

Primary point defects of interstitials and vacancies are created at the same rate, but their diffusion behavior is quite different. It has been comfirmed that interstitials can be mobile even below room temperature. Both theoretical calculations and experimental results have shown that the activation energy for interstitial diffusion is about a few hundred meV, but the activation energy for vacancy diffusion varies around 3-5 eV.[10] Especially in the electronic stopping damaged region, interstitial diffusion and interaction with vacancies would be enhanced by electronic ionization. It is imaginable that up on ion implantation, the knocked-out lattice atoms (interstitials) keep migrating until these reach some stable or metalstable states by recombining with vacancies to form new correct sites, or being trapped at the sample surface, at boundary of extended defects, and in plastic amorphous zones. Thus, in the implanted layer there exists an excess population of vacancies, causing lattice spacing expansion and positive strain build-up. Due to the homogeneous atomic distribution and strong covalent binding in single element crystals, this strain is only of a very small magnitude, which has been observed in all of the experiments, both with keV ions and MeV ions[6−7].

In III-V compound semiconductor crystals, their binary nature makes the damage process during ion implantation much more complicated. The different physical properties of two sublattice atoms (mass, atomic number, atomic size, and electronic negativity, etc.) imply that the ion-lattice collision cross section, defect generation rate, maximum energy transfer, and range distribution of recoil atoms for each type of sublattices may be vastly different. The variation in irradiation effects would also be affected by chemical binding, constitutient dissociation and atom migration. As the result of defect interaction and diffusion, a great number of antisite defects would be formed, which may or may not cause lattice strain after relaxation and distortion. However, creation and diffusion of interstitials of both sublattices are still major control processes that play an important role in the determination of the sign as well as in the magnitude of the lattice strain. In most III-V compound crystals, such as GaAs, the collision and interaction cross sections for the two sublattices may only have small differences. Self diffusion of both III and V sublattice atoms (e.g., Ga and As interstitials) is high. One of the effects is that a great number of antisite defects are created in the region near the surface, which have little contribution to lattice strain generation. The most pronounced result is to cause an excess of vacancies remaining in the crystal as the interstitials diffuse away and are trapped in the surface or some plastic zone. It leads to atomic density decreasing and lattice spacing expansion with building-up of positive lattice strain. However, in InP crystals, indium and phosphorus have a large mass ratio (3.71) as well as great differences in ionic radius and electronic negativity (see Table 2.1). According to atomic collision kinetics, indium has a much higher displacement cross section than that of phosphorus, but the recoiling velocity that indium atoms gain is limited due to its large mass. Thus, the total number of indium interstitials produced per unit volume is actually greater than that of phosphorus interstitials, and a greater fraction of indium recoils per unit volume produced are stopped. Hence, it results in an excess of the net indium interstitial population. Indium interstitials either recombine with indium vacancies to form correct sites, or with phosphorus vacancies to form antisites, or they stay in metastable states. As a consequence, relaxing indium interstitials and their associated defects cause lattice spacing contraction, which is a case observed in MeV ion implanted InP. However, in keV ion implantation, where the indium interstitial diffusion range is comparable with the depth of ion damaged region (a few thousand angstroms), indium interstitials can reach to the surface, leaving a large number of vacancies in the crystal, and cause the positive strain. Once, negative strain was observed in keV ion implanted InP[17]. In this instance, it might be due to an ion channeling effect, which results in a much greater stopping range of the ions.

The different characteristics of defect diffusion in MeV-ion-implanted GaAs and InP have been manifested by CRBS measurements, which were presented in the last two chapters. In GaAs samples implanted at room temperature, the dechanneling yields from implanted layers and surfaces remain at a very low level, even with doses up to 2 $\times 10^{16}/\mathrm{cm}^2$. This indicates a minimum of lattice damage or disordering. However, it may also imply that there exists, instead of displaced lattice atoms (i.e., interstitials), a large population of vacancies and antisites, which do not cause ion dechanneling. In this case, however, a large positive lattice strain field would be associated. In low-temperature-implanted GaAs, the "freeze-in" effect slows down interstitial diffusion. Ion dechanneling becomes much more pronounced due to the remaining interstitials and lattice disorder in the crystal. Correspondingly, XRCs have also shown a remarkable decrease of reflecting intensity by the positive strain field. However, in the InP sample ion dechanneling yields dramatically increase with the implantation dose, and the saturation extends towards the surface as the dose increases. This behavior reveals an increase of the excess interstitial population with the dose and interstitial diffusion towards the surface. This is manifested by a negative strain field shown in the corresponding XRCs.

4.5 Conclusions

By examining characteristics of primary lattice defects created through ion implantation, we have found that the lattice strain is closely associated with defect relaxation and lattice distortion. The sign and magnitude of radiation-induced strain are determined by the dominant population of certain types of defects, which, in turn, are controlled by the process of defect generation and diffusion. The model presented here has described kinematically the interactions of ion-lattice, defect-lattice, and defect-defect and predicts the defect population predomination. These help us to understand the phenomenon of lattice strain in III-V compounds produced by ion implantation. In GaAs implanted with MeV ions, due to fast diffusion of interstitials, vacancies become the dominant defect type, which induces the positive strain in the ion damaged surface layer and the implanted layer before it reaches phase transition point. In InP under MeV ion implantation, due to the high generation rate and the slow migration speed of indium interstitials, there exists an excess population of interstitial-type defects that givea negative strain to the damaged crystal. By a similar argurment, we expect that a negative strain effect under

MeV ion implantation may appear in AlSb among the III-V compounds, and in CdS among II-VI compounds.

It is worthwhile to note that the special effect of negative strain in InP induced by MeV ion implantation is centainly related closely to the crystalline properties of InP. InP has the largest values among III-V compounds, in atomic mass ratio, ionic radius, and electronic negativity for two sublattice atoms, and the largest ionicity for the crystal. A complementary effect of all these properties determines the effect of radiation-induced negative strain in InP. Once, it was suspected that the sign of the radiation-induced lattice strain may closely associate with the crystalline ionicity, which is determined by the lattice chemical binding strength. As the crystalline binding varies from the pure covalent bond in elemental crystals to the mixture of covalence and ionic bonds in compound semiconductors, then to the pure ionic bond in ionic crystals, the crystalline ionicity increases, and the radiation-induced lattice strain may change from positive to negative at some critical level. InP has the ionicity of 4.1, highest among III-V compound, and the experiments have shown it has a unique negative strain effect under ion irradiation. However, CdTe has a much higher ionicity (6.2) than InP, but it has a positive strain effect under the MeV ion implantation[18]. A similar effect of the radiation induced positive strain appeared in LiF, which is a good ionic crystal[18].

4.6 References:

1. U. Gonser and B. Okkerse, Physics Rev. 105 (1957) 757; 109 (1958) 663.
2. D. Kleitman and H. J. Yearian, Phy. Rev. 108 (1957) 901.
3. F. L. Vook and R. W. Balluffi, Phys. Rev. 113 (1959) 62; 113 (1959) 72.
4. R. O. Simmons, Phys. Rev. 113 (1959) 70.
5. R. E. Whan and G. W. Arnold, Appl. Phys. Lett., 17(9) (1970) 378.
6. V. S. Speriosu, B. M. Paine, and M-A. Nicolet, Appl. Phys. Lett. 40(7) (1982) 604.
7. C. R. Wie, PhD thesis, Caltech (1985) unpublished.

8. C. R. Wie, T. A. Tombrello, and T. Vreeland Jr., Phys. Rev. B33(6) (1986) 4083.
9. C. R. Wie, Nucl. Instr. and Methods, B37/38 (1989) 965.
10. C. Ascheron, A. Schindler, R. Flagmeyeer and G. Otto, Nuclear Instruments and Methods B36, (1989) 163.
11. M. Lannoo and J. Bourgoin, *Point Defects in Semiconductors,* vol. I and II. (Springer Series, Berlin) (1981).
12. A. Van Vechten, in *Handbook on Semiconductors, Vol. 3,* ed. S. P. Keller, (North-Holland Publishing Company) (1980), Chapter 1.
13. T. W. Dobson and J. F. Wager, J. Appl. Phys. 66(5) (1989) 1997.
14. G. A. Baraff, E. O. Kane, and M. Schluter, Phys. Rev. B21(12) (1980) 5662.
15. P. W. Anderson, Phys. Rev. Lett. 34(15) (1975) 953.
16. S. R. Elliott, *Physics of Amorphous Materials,* (John Willey & Sons, New York) (1988), p. 247.
17. T. Vreeland and M-A. Nicolet, private communication.
18. F. Xiong, Lab notes, Tandem Lab., Caltech (1988) unpublished.

Chapter 5

ON MECHANISMS OF LATTICE DAMAGE AND PHASE TRANSITIONS IN MeV ION-IMPLANTED III-V COMPOUND SEMICONDUCTORS

5.1 Introduction

The mechanism responsible for radiation-induced lattice damage and structural phase transitions is an important issue in the study of ion implantation from the basic theoretic interest to its practical application. In the case of keV ion implantation, much knowledge has been gained in many aspects of this subject, especially in Si. However, extending the ion energy to the MeV range not only causes deeper implantation, but also changes the lattice damage mechanism, which differs from that in keV ion implantation. Moreover, the physical processes involved in MeV ion implantation into III-V compounds are also much more complex than in single element materials (e.g., Si and Ge), because primary defect formation in a binary compound is much more complicated as discussed in the last chapter, and threshold energies for damage production, crystalline regrowth, and nucleation are lower.

In Chapters 2 and 3, we have presented the experimental results of our study on MeV ion implanted InP and GaAs. They have given us a clear picture of radiation damage profiles and structural changes in III-V compounds under MeV ion implantation and thermal annealing. It is the object of this chapter to give an overview of the physical processes involved in MeV ion implantation into III-V compound semiconductors. Drawing from the experimental results presented in Chapters 2 and 3, a spike model to describe the mechanism for MeV-ion-implantation-induced lattice damage and the structural phase transition in III-V compounds is proposed, along with a phenomenological discussion of the mechanism for defect annealing and recrystallization of implanted layers through thermal annealing.

5.2. Spike Damage — Mechanism of MeV-Ion-Implantation-Induced Lattice Damage and Phase Transition

During ion implantation, interactions between incident energetic ions and the lattice atoms while the ions penetrate the sample lead to a transfer of energy to the lattice, which in turn causes lattice damage as well as many other associated effects to the crystal. Various models have been proposed to describe the radiation-induced lattice damage and the crystalline-amorphous (c-a) transition in ion implanted semiconductor and metal crystals, such as early studies by Seitz[1] and Brinkman[2]on the concept of the thermal spike effect in semiconductors and metals, and the recent review by Sadana[3] on the work in III-V compound semiconductors. However, many aspects of the role of the physical processes involved still remain controversial, especially for compound semiconductors and in high energy implantation.

Initially, much attention was given to the production of Frenkel defects because it was believed that the primary effect of ion implantation on a crystal is to produce knocked-on atoms as a result of elastic or inelastic collisions with an energy transfer. The knocked-on atoms that receive an energy greater than a threshold amount will be displaced from their lattice sites and persist as permanent interstitials, leaving original lattice sites open as vacancies. Seitz[1] introduced the idea of "thermal spikes" to describe the process involved. He described that the thermal spike was generated along the tracks of incident ions and knocked-on atoms due to energy transfer, and it could heat the lattice locally to a very high temperature of

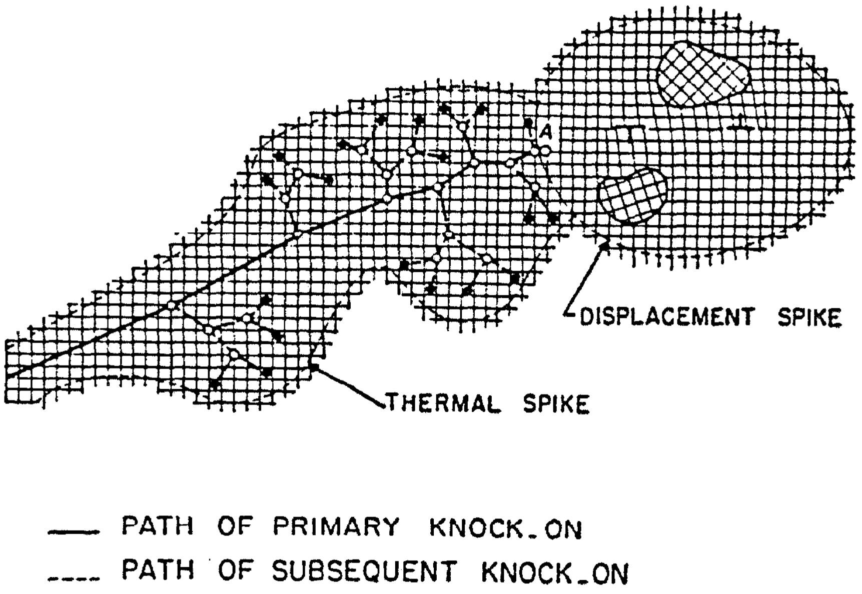

Figure 5.1 Schematic representation of a displacement spike in a two-dimensional lattice (after Brinkman [2]).

the order of 10^4 °C. Such spikes would stimulate any of the effects that high temperature would, such as promoting diffusion and producing lattice disorder. It was also pointed out that the typical spike would be exceedingly transient, lasting only for a time of the order of 10^{-11} sec, and the heated lattice would quench rapidly to ambient temperature. Brinkman[2] extended the model of the thermal spike to the case in which the incident ions displaced a number of atoms in succession. He described that along the path of a high energy primary knocked-on atom, there exist two separate regions, each containing a different form of damage. As depicted in Fig. 5.1, along the path of a knocked-on atom, the high energy region to the left of point A will retain all of the displaced atoms produced there as interstitial-vacancy pairs, and there will be no appreciable atomic interchange among the remainder of the atoms. On the other hand, the low energy region to the right of point A, near the end of the displacement path, undergoes melting and resolidification. Dislocations are nucleated as a result of the spatial separation of interstitials and vacancies in the collision. It was estimated that it may possess a linear dimension of the order of 50 Å. He termed such a highly chaotic region the "displacement spike." Its difference from the thermal spike discribed by Seitz is that the entire volume of a displacement spike is required to have been melted and resolidified, thus giving it well-defined boundaries, while the thermal spike does not, as Brinkman believed, reach a temperature at which atomic interchange can occur. However, there was no much direct experimental evidence to support these models. Later on, Gonser and Okkerse[4] performed an experiment on one of the III-V compound semiconductors, GaSb. The results suggested very strongly that thermal spikes had been introduced under MeV deuteron irradiation. They had some of the general properties of the displacement spikes described by Brinkman. In these spike regions, the materials would be present in a liquid-like lattice configuration, markedly different from the matrix configuration.

There are several other modified versions of the model by Seeger[5], Beeler and Besao[6], and Chadderton and Eisen[7] to explain the size and nature of damage production. Sadana[3] has reviewed those models with an emphasis on phase transitions in view of the HRTEM results. He summarized the model for eventual amorphization into two categories: 1) a heterogeneous model that suggests that individual damage clusters are amorphous and complete amorphization occurs as a result of accumulation and merging of individual damage clusters; and 2) a homogeneous model that suggests that when the defect concentration reaches some critical value in a single crystal, the crystal becomes unstable and transforms to an amorphous state. The first mechanism is generally believed to operate for heavy ions whereas the second occurs for light ions. However, the cases discussed are all for keV ion implantation. Most recently, Holland et al.[8] have reported that the damage in Si implanted with MeV ions was shown to be consistent with the homogeneous model, and in Ge by the heterogeneous nucleation model.

We have undertaken an investigation of MeV ion implantation in III-V compounds. The samples were implanted at ambient temperature or at LN_2 temperature. The results of sample charaterization by many analytical techniques for structural changes presented earlier have led us to propose the following model for the lattice damage and amorphization in MeV-ion-implanted III-V compound semiconductors. We classify the primary effect of ion-lattice interaction in the crystal during MeV ion implantation into two major catagories — electronic spike and nuclear spike. These two types of spikes are closely correlated with the electronic energy loss and the nuclear energy loss of the incident ions, which was shown in Fig. 1.1. The electronic spike originates from the cascade collisions between highly energetic ions and target electrons. It induces electronic excitation and ionization of target atoms and causes electronic damage to the crystal in the region near the surface. By this process the incident ions lose most of their kinetic energy and slow down. The nuclear spike is produced along ion tracks in the low energy range (a few keV or less) just before the end-of-range (EOR) of the ion due to nuclear collision cascades and atomic displacement, through which the crystal suffers direct structural damage. In detail, these two types of spikes have different influences on the target. In the electronic spike region, spike-related electronic ionization distorts the electronic configuration of the periodical structure. Due to a large energy transfer between ions and electrons, thermal heat would be induced. But it disperses very rapidly by fast electron migration and vibration or through phonon emission. The excited electrons and atoms of the lattices come into equilibrium very slowly, so that the lattice would persist at a high temperature for a certain time period, but below the sample melting point at a normal beam flux. However, this excitation would enhance remarkably defect diffusion and the migration of displaced atoms. The electronic-spike-induced temperature would be sufficiently high to anneal the interstitial-vacancy pairs as well as other defects in the region. Under the nuclear spike, the direct ion-nuclear collision cascade leads to a large momentum transfer and may locally generate high temperature along the ion transport paths near the EOR and the displacement tracks of knocked-on lattice atoms. When the instant ion energy loss is intense, this temperature can reach the crystal melting point. As a result, the crystal undergoes a c-a transition through local melting and rapid quench process in a time of a few picoseconds. Individual regions resolidify into a quasi-liquid (amorphous) structure, which differs from the crystalline structure that would form if the cooling occurred more slowly than the crystal relaxation time. The behaviour of the nuclear spike is different from the displacement spike described by Brinkman where the sample resolidifies to a crystalline structure with nucleation of dislocations. However, it is consistent with the results of a recent computer simulation based on molecular dynamics[9].

Therefore, during ion implantation there exist three primary processes: 1.) the creation of lattice defects and amorphous zones by nuclear spikes, 2.) migration of displaced atoms, implants, and defects under the influence of electronic spikes due to changes of stoichiometry and defect concentration, and 3.) recombination of implantation-induced and residual defects, and recrystallization of amorphous zones (in situ dynamic annealing) stimulated by electronic spikes. In III-V compounds, due to the difference in the constituents and the properties of the two sublattices, the nuclear spike has a different displacement rate for each type of sublattice atom, resulting in a deviation in local stoichiometry. Thus, the ion induced microscopic structural changes would be different in different compounds. However, the electronic spike damage to the sample surface would be very much the same. All of these have been observed in our experiment of MeV ion implantation into III-V compound semiconductors through XTEM and CRBS analysis. In general, at a low implantation dose, due to a competition between damage generation and annealing, only a high density of ion irradiation induced defects can be found (see Figs. 2.11 and 2.12ab). It follows a distribution closely correlated with the nuclear stopping power profile, located at the EOR of the ion, R, with a width close to the ion range straggling, ΔR. The concentration of point defects in each point before reaching a critical level for amorphization is associated with the integrated ion energy deposited through nuclear stopping there. But the observed number of defects is also dependent on the implantation conditions, such as the target temperature and the beam flux intensity. The case for this has been shown in GaAs implanted with 2 MeV oxygen ions at RT and LT (see Section 3.3). In the region near the surface, there is an almost defect free region. As the dose increases, amorphous zones at the EOR of the ions become more visible and more stable. Precipitation of amorphous pockets in the crystalline matrix can be easily found (see Figs. 2.14bc). In this case we have directly observed the spike-induced amorphous clusters at the EOR and along the paths of knocked-on atoms (see Fig. 2.14c). A continuous buried amorphous layer forms when these initially amorphized zones overlap fully — a heterogeneous c-a phase transition. At the surface region where the electronic spike dominates, the defect concentration density increases due to the accumulation of nuclear damage and the outgoing diffusion of defects. At a very high dose, a uniform and buried amorphous layer forms with a sharp interface at the EOR (see Figs. 2.11 and 2.14d). Its maximum depth is determined by the ion maximum range, which is well defined statistically by the incident ion energy. Towards the surface, the amorphous transition occurs as heavy damaged crystalline regions collapse when the defect density reaches a critical value and a homogeneous phase transition emerges. The implanted amorphous layer, from a macroscopic view, extends towards the surface after an amorphous layer is formed at the EOR by nuclear spike damage.

The ion-induced lattice damage and amorphization are also associated with lattice strain generation and saturation. As we discussed in the last chapter, the relaxation of ion induced defects leads to the build-up of lattice strain. On the other hand, the presence of the nuclear spike-damaged zones also gives rise to tension, the surrounded rigid framework of undamaged lattice prevents relaxation of damaged zones, causing lattice strain in the crystalline neighbourhood. The formation of a continuous amorphous layer provides a plastic region for the lattice strain to relax. The lattice strain saturation occurs when the strain production and relaxation reach an equilibrium state. Thus, the strain saturation level is expected to be uniquely defined by the nature of the target crystal, independent of the ion species and incident energy.

5.3 Homogeneous Nucleation and Epitaxial Regrowth — Mechanism of Recrystallization During Thermal Annealing

The behaviour of an implantation-damaged layer under thermal annealing is another important subject in the study of ion implantation, because the degree of implant activation, defect annealing, and recystallization of the amorphous layer determines the quality of the implanted crystal. Many investigations have been undertaken on this subject with conventional thermal annealing process, and most recently with rapid thermal annealing. Most of them concentrated on the changes of electrical properties — activation of the implants and annealing of implantation-induced defects.

Whereas for both single element and compound semiconductors there may be similar traits in lattice damage and amorphization under ion implantation, the mechanisms of defect annealing and recrystallization in implanted samples are quite different. One obvious evidence is that the activation energy for defect annealing in compounds is much lower than in Si and Ge. The minimum temperature for defect annealing is around 200 °C for III-V compounds, while it is 500 °C for Si. As another example, the regrowth structure from ion-implantation-induced amorphous regions in Si tends to be free of secondary defects — especially micro-twin and stacking faults. In contrast, regrowth of such layers in III-V compounds results in a large amount of disorder, which has been observed in GaAs. Our annealing experiments of MeV-ion-implanted InP with a conventional process presented in Chapter 2 have clearly revealed the annealing behavour of InP by XTEM , XRC, and CRBS measurements. This evidence has led to a better insight of the mechanism for defect annealing and the a-c transition in MeV ion implanted III-V compounds.

As we observed, recrystallization during high temperature annealing can be proposed to go through two kinds of processes: homogeneous nucleation (HN) and solid phase epitaxial (SPE) regrowth. SPE is a common process that occurs in the recrystallization of implanted amorphous layers in semiconductors. The SPE process originates at the crystalline-amorphous interface, and the interface then advances in a layer-by-layer manner. Atoms in the amorphous region make bonds with those in the single crystal substrate or the upper damaged crystalline surface layer. The rough nature of the boundaries at the interfaces and the regrowth orientation effect[3,10] eventually result in a microfaceted and simply-connected growth front from the interfaces. It would be expected that the growth rate in the [100] direction is fastest followed by [110], and then [111]. However, as predicted by Sadana et al.[1,5], the {111} directions would have a high probability for nucleating planar microtwin defects, because the energy of a [111] twin boundary is the lowest of many planar defects for the diamond structure. The {111} facets would provide favorable sites for accommodation of a dopant concentration above the solid solubility limit and non-stoichiometry that is produced by the implantation. Seeding from the original stacking faults and twins formed during implantation in the crystalline substrate, bundles of stacking faults will propagate rapidly along with solid phase epitaxial regrowth. The HN process involves thermally-activated crystalline nucleation in the central region of the transition layer. In a microscopic view, the ion implanted layer can still be seen to be a composite of numerous randomly-oriented fine crystallites. The nucleation proceeds to grow from those fine crystalline nuclei. As there are a large number of growth fronts in various orientations, there is a growth competition among neighboring crystallites, resulting in a polycrystalline structure in the center of the buried implanted layer. Normally, SPE is the dominant process because its growth rate is much larger than the HN. This occurs in keV-ion-implanted amorphous layers and low dose MeV-ion-implanted amorphous layers that are very thin. However, when the ion implanted layer is very thick (more than 1 μm), such as in the case of high dose MeV-ion-implanted layers, there would be a competition between these two growth processes. The recrystallization will end when epitaxial layers with stacking fault bundles from both interfaces impinge upon the central nucleated polycrystalline layer. We have observed this phenomenon in InP, which was implanted with MeV nitrogen ion to a dose of $10^{16}/\text{cm}^2$.

5.4 Conclusions

In conclusion, our study has led us to a better understanding of the mechanisms of MeV-ion-implantation-induced amorphization and subsequent thermal-annealing-stimulated recrystallization in III-V compound semiconductors. In MeV ion implantation, the ion-lattice interactions induce two energetic spikes — electronic spikes and nuclear spikes, causing electronic damage in the region near the target surface and structural damage in the region near the EOR of the ions. A continuous amorphous layer is first formed through the heterogenous transition due to overlapping of the individual amorphous clusters generated by nuclear spikes. The amorphous layer extends towards the surface under homogenous transition when the defect concentration reaches a critical level and the crystal collapses. The nuclear spike plays a dominant role in the initial lattice structural damage and the c-a transition. The electronic spike enhances defect migration and recombination, which marks it distinct from keV ion implantation where the electronic spike has a minimal effect. Though the nature of the nuclear spike in both kev and MeV ion implantation is very much the same, its effect on lattice damage is homogenous in the MeV case due to a large energy spread from the integrated energy straggling of the incident MeV ions before the nuclear spike occurs. During high temperature annealing, thermally-activated recrystallization in the buried amorphous layer is stimulated. In the center of the buried layer, homogeneous nucleation takes place to form a polycrystalline structure. Near the amorphous-crystalline interfaces, solid phase epitaxial regrowth emerges. Seeding from the implantation-induced defects at the interfaces, a highly disordered structure with long range stacking faults and microtwins grows, impinging upon the central polycrystalline structure.

5.5 References

1. F. Seitz, Physics Today, 5(6) (1952) 6.
2. J. A. Brinkman, J. Appl. Phys. 25(8) (1954) 961.
3. D. K. Sadana, Nucl. Instr. and Methods, B7/8 (1985)375; and references therein.
4. U. Gonser and B. Okkerse, Phys. Rev. 109(3) (1958) 663.

5. A. Seeger, Proc. Int. Conf. on Peaceful Use of Atomic Energy, 1958, p.250.
6. J. R. Beeler and D. G. Besco, Phys. Rev. 134A (1964) 530.
7. L. Chatterton and F. H. Eisen, Proc. 1st Int. Conf. on Ion Implantation (Gordon and Breach, New York) (1971) p.445.
8. O. W. Holland, M. K. El-Ghor, and C. W. White, Appl. Phys. Lett., 53 (1988) 1282.
9. T. Diaz dela Rubia, R. S. Averback, R. Benedek, W. E. King, Phys. Rev. Lett., 59 (1987) 1930.
10. D. K. Sadana, T. Sands, and J. Washburn, Appl. Phys. Lett. 44 (1984) 623.

Chapter 6

APPLICATION OF MeV ION IMPLANTATION TO SEMICONDUCTOR LASER DEVICE FABRICATION

6.1. Introduction

Ion beam processing of semiconductors with keV ions is a well-established technique for material surface modification and for electrical device fabrication. Its application for fabricating electronic and optoelectronic devices can be found in numerous reports. However, as we presented before, extending the beam energy to the MeV range in the processing offers many decided advantages in terms of a greater range of the ions, which results in deep implantation with minimum radiation damage at the sample surface. Thus, it allows unique opportunities for the property modification of interfaces and deeply buried layers, and has high potential for three-dimensional device fabrication[1]. In several areas, especially for III-V compound semiconductors, MeV ion beam processing has several promising applications because it has capabilities complementary to alternative methods such as thermal diffusion, chemical etching, and epitaxial regrowth. In this chapter, one example of an application of MeV ion beam processing in III-V optoelectrical device fabrication will be presented.

We have undertaken an investigation of the utilization of MeV oxygen ion implantation to fabricate directly single quantum well (SQW) graded-index separate confinement heterostructure (GRINSCH) AlGaAs/GaAs lasers[2]. This has been shown to be a simple and very promising technique for semiconductor laser device processing. The devices made in this way have achieved high performance with high quantum differential efficiency of over 85% in a 360 μm long and 10 μm wide stripe-geometry device. The results have also demonstrated that excellent electrical isolation (breakdown voltage of over 30 volts) and low threshold currents (22 mA) can be obtained with MeV oxygen ion isolation. It is proposed that oxygen-ion-implantation-induced selective carrier compensation and compositional disordering in the quantum well region as well as radiation-induced lattice disordering in $Al_xGa_{1-x}As/GaAs$ may be mostly responsible for electrical and optical modification of interfaces and the buried layers in this fabrication process.

Following a general consideration on fabrication technology of semiconductor lasers, the fabrication process for SQW-GRINSCH lasers with MeV oxygen ion implantation will be presented in detail in Section 6.3. In Section 6.4 the mechanism of high performance in ion implanted lasers will be discussed, along with remarks on the application of MeV ion implantation for fabrication of other semiconductor laser systems.

6.2. General Consideration on Semiconductor Laser Fabrication

Development of semiconductor lasers has gained tremendous interest in recent years, as it is believed that future generations of supercomputers will rely on monolithic semiconductor lasers for their internal communication, in addition to their other applications. In semiconductor laser technology, considerable attention is still being paid to low threshold, high efficiency, and large power devices[3−13]. Among many limiting factors that affect the device performance, the injection current control and electrical carrier and optical field confinement are most important. Many efforts have been made to reduce the leakage current and improve the transverse confinement by developing fabrication techniques and novel structures. Double heterostructure (DH)[6], graded-index separate-confinement heterostructures[7,8], and single quantum well (SQW) or superlattice structures[9,10] have been developed to give better optical wave guiding and electrical carrier confinement in the vertical direction. Methods of buried heterostructure[11], impurity diffusion [12], and compositional lattice disordering[13] have been utilized in conventional fabrication for current control and lateral confinement. However, conventional fabrication processes commonly involve a complex procedure. As an example, one typical and successful example of the popular laser system incorporating a transverse confinement with the buried heterostructure[11,14] is represented in Figure 6.1. To fabricate these devices, multiple steps have to be taken, as illustrated in Figure 6.2. First, three layers: the laser active layer (undoped GaAs) sandwiched by two cladding layers (n-$Al_xGa_{1-x}As$ and p-$Al_yGa_{1-y}As$) is epitaxially grown on an n-GaAs crystalline substrate. The structure is then chemically etched through a mask down to the substrate level, leaving a thin rectangular mesa composed of the original layers. A "burying" $Al_zGa_{1-z}As$ layer is then regrown on both sides of the mesa, following with a growth of a dielectric layer (silicon oxides or silicon nitrides) by thermal processing on the top, opening a window by lithography to align with the mesa stripe for passing the injection current. Finally, ohmic contacts are evaporated and alloyed onto the two surfaces. The most important feature of the buried heterostructure laser is that the active GaAs region is surrounded on all sides by the lower index AlGaAs, so that electromagnetically the structure is that of a rectangular dielectric waveguide. The transverse dimensions of the active region and the index discontinuities (i.e., the Al mole fractions x, y, and z) are so chosen that only the lowest order transverse mode can propagate in the wave guide. Another important feature of this laser is the confinement of the injected carriers at the boundaries of the active region due to the energy band discontinuity at the GaAs/AlGaAs interface. These act as potential barriers inhibiting carrier escape out of the active region. GaAs semiconductor lasers utilizing this structure have been fabricated more typically with a threshold current of ~20 mA, and the external differential quantum efficiency of about 30~50% at 300K. The devices with other novel structures (QW, GRIN-SCH, or combined structures) have achieved optimal results with very low threshold current[3,5,12] down to 1 mA, and the external quantum effeciency[4,5] up to 70%.

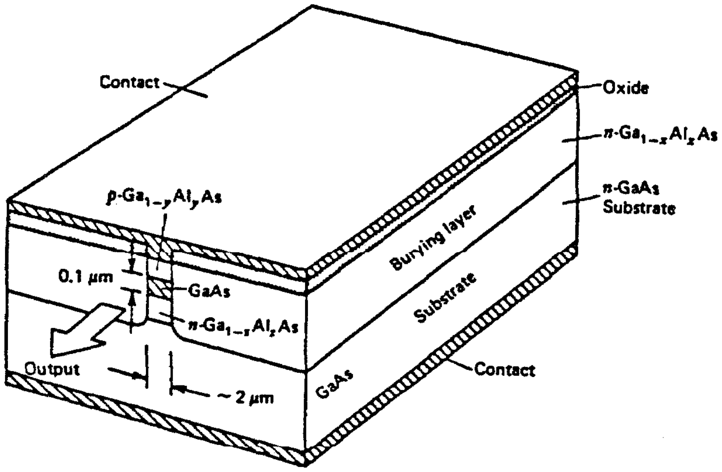

Figure 6.1 An example of a conventional buried heterostructural laser, fabricated with etching and epitaxial regrowth processes. (Taken from ref. 11.)

For the device fabrication techniques, in addition to several conventional methods such as diffusion, etching, and burying insulation layer regrowth, all of which have been shown to have some technical difficulties, ion implantation has been proven to provide some advantages for modifying buried layers and interfaces, especially for III-V compound semiconductor systems as have been presented in the last two chapters. It was established that selected ion species can create insulating or semi-insulating layers in semiconductor crystals. Such high resistivity layers placed in appropriate regions block current flow through undesired leakage paths in semiconductor lasers. In the AlGaAs-GaAs system, bombardment with protons or deuterons, which utilizes the lattice damage mechanism, was first employed to demonstrate such a possibility[15–16]. Oxygen ion implantation by chemical doping has been shown to result in a stable semi-insulating material[17–19] and has previously been reported as a current confinement technique for planar stripe lasers[20,21]. This is also a potentially promising technique for current confinement in AlGaAs/GaAs channeled substrate planar lasers[22]. Some work on Be or Fe ion implantation into the InGaAsP/InP system for laser fabrication has also been

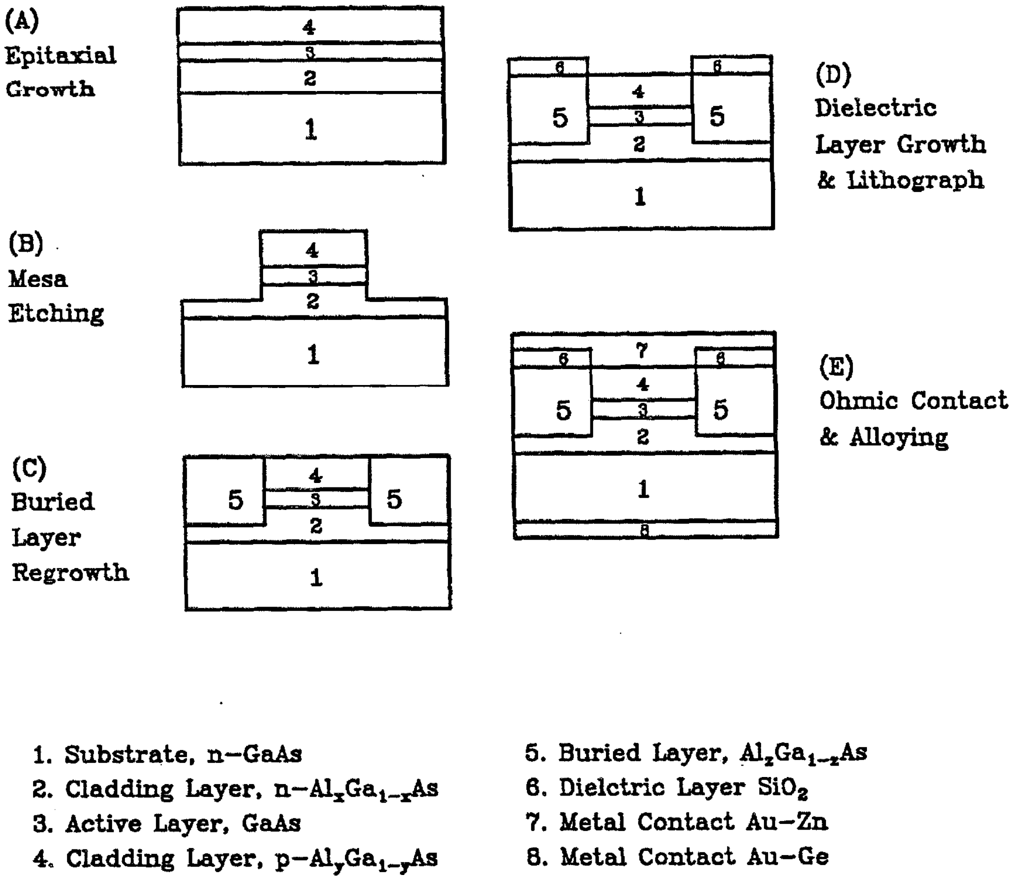

Figure 6.2 A sketch of the procedure for fabrication of a buried heterostructure semiconductor laser.

reported[23,24]. However, most of the above mentioned investigations were carried out by preparing a semi-insulating layered substrate through keV ion implantation followed by expitaxial growth of active and cladding layers on top. In our investigation presented here, fabrication of SQW-GRINSCH lasers has employed MeV oxygen ion implantation. It has taken advantage of selective carrier compensation, chemical doping, and implantation-induced compositional disordering with Al interdiffusion through deep implantation, and provides for current control and carrier

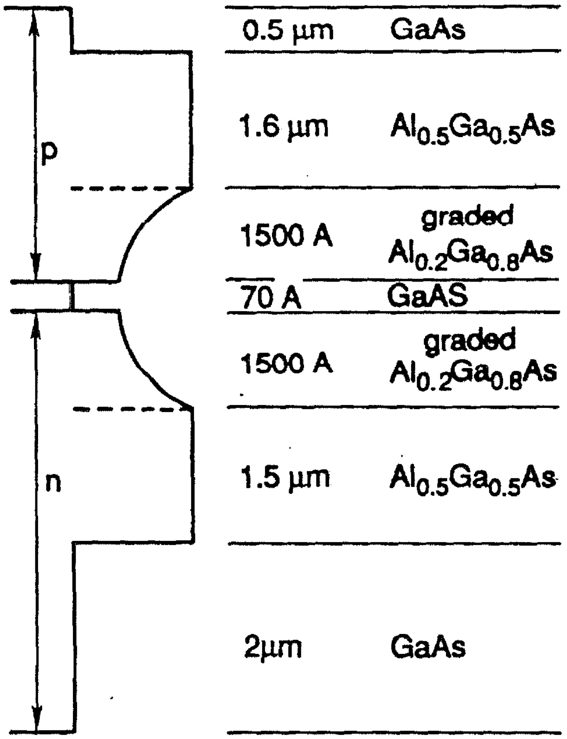

Figure 6.3 A sketch of the layer structure of a single quantum well GRIN-SCH AlGaAs-GaAs laser grown by the MBE method.

confinement, resulting in better device performance and electrical characteristics.

6.2. Fabrication of SQW-GRINSCH (Al,Ga)As Lasers by MeV Oxygen Ion Implantation

The SQW-GRINSCH AlGaAs/GaAs layer structure used in this study, as shown in Figure 6.3, was grown by the molecular beam expitaxy (MBE) method on an n-type Si doped < 100 > oriented GaAs substrate. A 2 μm GaAs buffer layer with uniform composition was first grown on the substrate in order to reduce substrate related defects. Following the growth of a Si-doped $Al_{0.5}Ga_{0.5}As$ cladding layer, a 70Å quantum well active layer was sandwiched between two graded-index

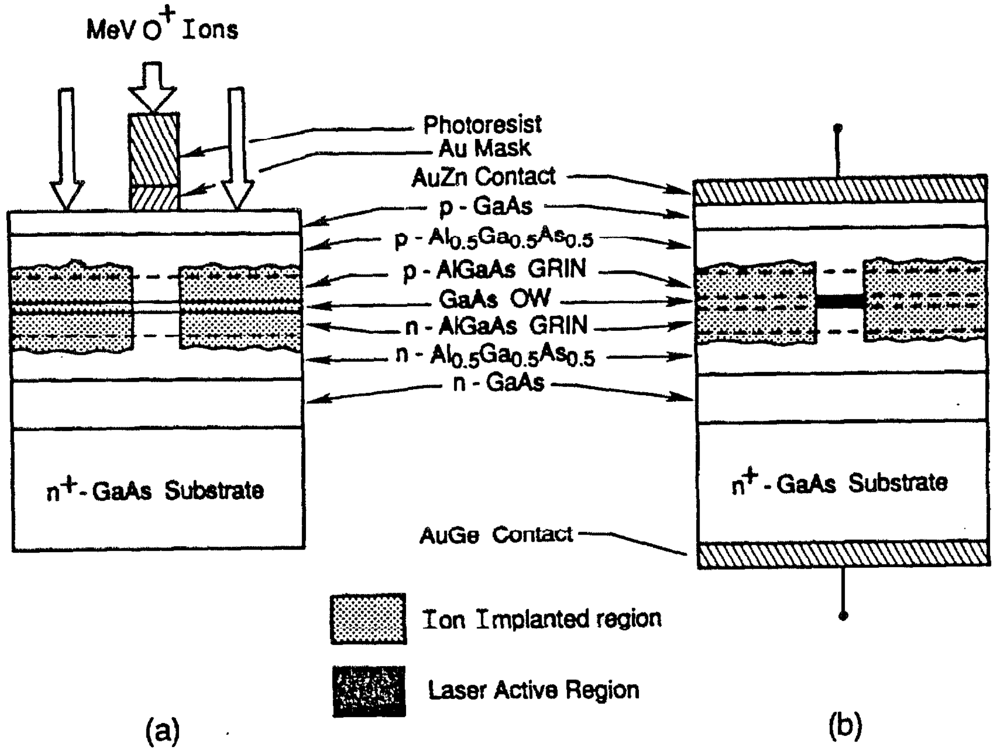

Figure 6.4 Cross sectional views of (a) a masked and as-implanted single quantum well GRINSCH laser device chip, and (b) an oxygen-implantion-fabricated laser device with such a structure.

$Al_xGa_{1-x}As$ wave guide layers of 1500Å thickness, in which the Al mole fraction was varied from x=0.5 to x=0.2 towards the quantum well edges. These graded-index $Al_xGa_{1-x}As$ layers provide parabolic waveguide regions for vertical confinement both for electrical carriers and the optical field. The growth was then continued with a Be-doped $Al_{0.5}Ga_{0.5}As$ upper cladding layer and a GaAs cap contact layer.

MeV oxygen ion implantation was employed for the lateral confinement, as indicated schematically in Figure 6.4. The processing of the device began with delineating the mask stripes along the < 110 > direction on the surface by using photolithography. The mask stripe is 10 μm wide and consists of a 3500Å gold film with a 4 μm thick photoresist (AZ4400) layer on top. It defines the laser cavity width and provides enough material to prevent 2 MeV oxygen ions from reaching the lasing region and causing implantation damage. Ion implantation was carried out at room temperature using the Caltech Tandem accelerator. The beam energy of 1.8 MeV was chosen according to our data on oxygen ion range versus beam energy in GaAs and photoresist as well as standard stopping power data. A dose of $2\times10^{15}/\text{cm}^2$ was found to be optimal with a beam flux under 1 $\mu\text{A}/\text{cm}^2$. Such a condition was chosen in order to let the implanted layer straddle the graded-index layers and the quantum well layer and completely compensate the original electrical conducting carriers in the desired isolation region with minimal radiation damage in the surface layers as well as in the quantum well side edges. A diagram of the masked and as-implanted sample is shown in Figure 6.4a along with an indication of oxygen ion implanted region.

Following implantation the mask was removed by a chemical procedure consisting of etching the sample in HCl acid for 1 min for the photoresist layer, and then etching in a commercial gold etchant for the Au film. The sample was then annealed in a graphite heater at 650°C for 10 min in N_2 ambient gas in order to remove the damage produced by the implantation. This optimum condition was determined in a test of the annealing procedure for oxygen-implanted n-type and p-type GaAs, where we observed the effect of selective carrier compensation as was presented in Chapter 4. Finally, the AuZn was deposited to contact the surface p-type GaAs, and AuGe was evaporated to the backside to contact the n-type GaAs substrate. These metal contacts were alloyed at 450°C for 20 sec. The individual laser chips were then cleaved without subsequent coating to obtain the reflecting end facets for testing. A schematic diagram of a fabricated device is shown in Figure 6.4b.

For comparison, a SiO_2 stripe-geometry laser was also fabricated from the same MBE grown wafer as that used for implantation-fabricated devices. The SiO_2

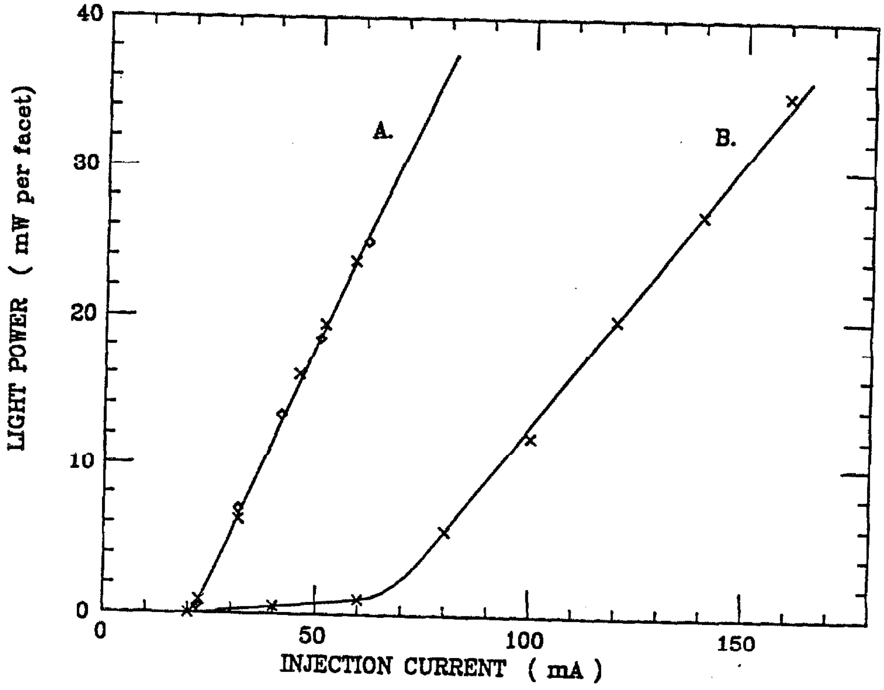

Figure 6.5 Light output characteristics of a single quantum well GRINSCH AlGaAs-GaAs laser fabricated (A) by high energy oxygen ion implantation with a cavity of 10μm $\times$360μm (I_{th} = 22 mA, η_{exp} = 85 %) and (B) with SiO_2 isolating stripe with a cavity of 10μm $\times$420μm (I_{th} = 65 mA, η_{exp} = 51 %).

layer was 2000Å thick and thermally grown on the sample surface. The laser stripe was 10 μm wide and the cavity was 420 μm long.

Optical characterization of the fabricated lasers was performed at room temperature under a probe station. For a typical device of cavity length 360 μm, the lasing emission wavelength is 0.842 μm. The light output from two end facets were tested to be same. The characteristic curve of the output light power per facet versus the pulsed injection current (Curve A) is plotted in Figure 6.5. It has been found that the threshold current is about 22 mA, and the threshold current density is 610 Acm^{-2}. A total slope efficiency (both as-cleaved facets combined) associated with this particular laser is about 1.25 W/A. The corresponding total external quantum efficiency over 85% was obtained. As a comparison, the output characteristic curve (Curve B) of a SiO_2 stripe laser has also been plotted in Figure 6.5, where it is shown that the threshold current in this 10 μm wide and 420 μm stripe laser is about 65 mA and the total external quantum efficiency is about 51%.

In addition, the electrical characteristics of the laser diode were also measured. A typical current-voltage curve is presented in Figure 6.6. The oxygen ion implantation fabricated device has also shown exellent electrical characteristics. A low leakage current and a high and sharp reverse breakdown voltage of over 30 volts in the reverse bias has been obtained. The reported experimental value of this parameter for SiO_2 stripe lasers is about 5~7 volts[25].

6.4. Mechanisms of High Performance in MeV Oxygen Ion Implanted Lasers

The mechanism of improved high performance in MeV-oxygen-ion-implanted lasers is rather complex. As pointed out earlier, high performance of semiconductor lasers requires crucial current control and lateral electrical and optical confinement, the same as for the vertical confinement. Compared to conventional processes for buried heterostructure laser fabrication, oxygen ion implantation provides a simple and promising technique with fewer critical steps. It takes advantages of all effects produced by implantation. First, the deep-level-associated high resistivity in the implanted region gives directly a precise injection current control around the laser active region, instead of using SiO_2 on top of the layers. This minimizes significantly the device threshold current. Ion-implantation-induced compositional lattice disordering should be the main feature responsible for high lasing quantum efficiency. Intermixing of the GaAs quantum well layer with surrounded GRIN $Al_xGa_{1-x}As$ layers induces Al composition diffusion, resulting in an Al mole fraction increase in

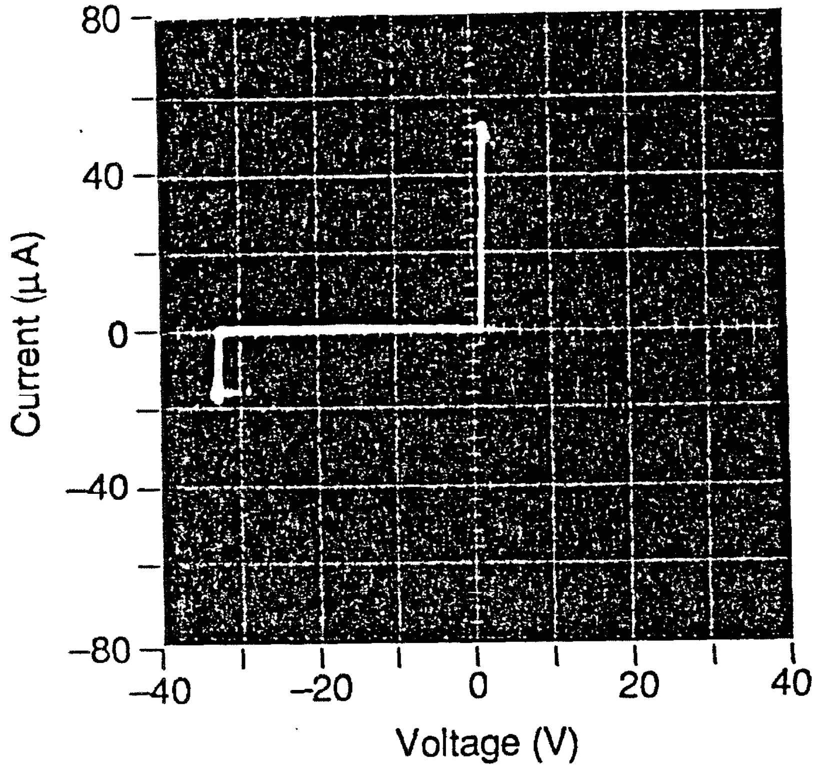

Figure 6.6 Electrical characteristics of a single quantum well GRINSCH AlGaAs-GaAs laser fabricated by high energy oxygen ion implantation as shown in Figs. 3 and 4.

the implanted GaAs quantum well in the lateral sides of the lasing region. In turn, it causes an bandgap energy up-shift and a refractive index change in the layer, and provides useful modification for electrical carrier confinement and optical wave guiding to the GaAs lasing area. In fact, quantum well layer disordering has been employed to fabricate sophisticated buried heterostructure lasers[26–28], where the layer disordering was induced by impurity diffusion through thermal annealing. Ion implantation can provide more effective, selective, and maskable means to lattice disordering. The experiment has indicated that implantation damage alone is efficient for this purpose, but an active impurity ensures more of a complete effect[29].

In our case, the quantum well disordering with Al interdifussion was directly induced by implanted oxygen ions in a low temperature process, and simultaneously cooperated with high resistivity generation in one step. High efficiency in oxygen ion implanted lasers has also indicated that the optical absorption by residual radiation-induced damage and associated deep traps is very low, since most of the radiation lattice damage has been recovered through the post-implantation annealing process at high temperature.

In addition, oxygen ion implantation induced electrical isolation has better heat resistance and thermal stability than that of a SiO_2 stripe, since GaAs has much higher thermal conductivity, 100 times over SiO_2 materials[21]. In the oxygen-ion-implanted laser, the power-dissipating active region is bounded directly by ion-implanted, electrical insulating GaAs or AlGaAs layers in the sides and AlGaAs on the top and bottom to conduct heat to the heat sink. On the other hand, in the SiO_2 isolated laser, thermal conduction is also constrained by the area of the conductor stripe. On both sides, the SiO_2 layer forms a significant thermal barrier. In this sense, one should expect better laser lifetime and reliability in implanted lasers than in SiO_2 stripe lasers. This may also be a possible reason for improvement of the breakdown voltage.

6.5. Remarks on Application of MeV Ion Implantation for Fabrication of Other Laser Devices

Formation of buried insulating layers and modification of interfaces by ion implantation into semiconductors as well as their application to device fabrication are exploited in modern electronic device technology. Application to fabrication of field-effect transistors, microwave and optoelectronic devices has been described in many reports. Most common applications can be classified into two catagories[30]. One technique is to prepare a semiconductor-on-insulator (SOI) structure by ion implantation with candidate ions; then the material serves as a substrate for further device fabrication. Most early ion-implanted laser systems were processed in this way. Another method is to cause high resistivity directly in the desired regions by implantation in a layered device, providing a current blocking region for better device performance. In the latter case, the deep implantation with MeV ions is presented in this chapter. As is found in the III-V compound semiconductor materials that only a moderate beam dose is required in order to produce high resistivity doping by ion implantation. In addition, heavier oxygen ions tend to minimize the energy straggling effect compared to proton implantation. As a result, lateral spreading under the shadow mask is reduced during implantation, giving a high lateral spatial resolution and sharp interfaces. All this makes the implantation technique very promising for practical utilization.

We have also proposed to apply MeV ion implantation to device fabrication of the InP laser system[30]. We found that MeV nitrogen ion implantation can generate high resistivity in n-type InP crystals. Two different laser structures with ion implantation for fabrication have been suggested. Figure 6.7a shows an $In_xGa_{1-x}As_yP_{1-y}$/InP double heterostructure laser with a highly resistive layer made by implantation with nitrogen for lateral current control and carrier confinement. This scheme has been shown to be a simple and effective technique through the demonstration of the example presented above. Another example shown in Figure 6.7b is a buried crescent $In_xGa_{1-x}As_yP_{1-y}$/InP laser. The substrate is prepared by direct ion implantation to form a buried insulating and semi-insulating layer in an InP crystal, followed by channel etching and epitaxial regrowth of a double heterostructure with a crescent active region.

6.6. Conclusions

In summary, single quantum well GRINSCH lasers have been fabricated using high energy oxygen ion implantation in combination with optimized thermal annealing. High external quantum efficiency, low threshold current, and excellent electrical characteristics were obtained on 10 × 360 μm^2 stripe lasers. This technique introduces simultaneously buried high resistivity for the current control and

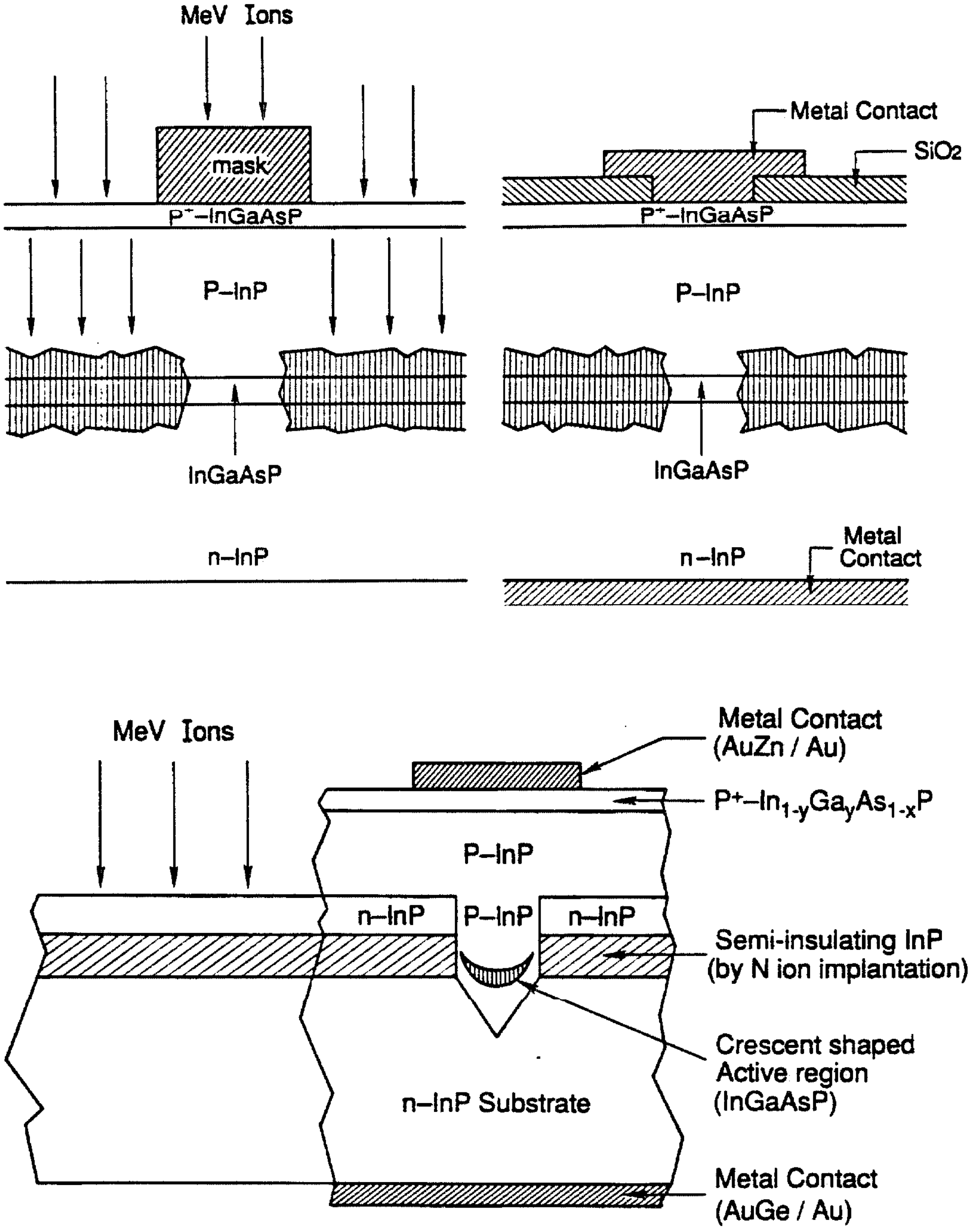

Figure 6.7 Schematic cross sections of proposed In$_x$Ga$_{1-x}$As$_y$P$_{1-y}$/InP laser devices: (a) fabricated with MeV ion implantation, providing a high resistivity region around the active area for lateral current control and carrier confinement; (b) buried cresent double heterostructure in a semiconductor-on-insulator (SOI) Inp substrate prepared by MeV ion implantation.

compositional lattice disordering for transverse confinement and minimizes the critical processing steps required by conventional processing. It is shown that oxygen-ion-induced selective electrical compensation in n-type GaAs and AlGaAs as well as implantation-induced lattice disordering around the quantum well layer provides directly a good electrical isolation with a good spatial resolution. Oxygen ion bombardment can also induce Al composition interdiffusion in AlGaAs/GaAs superlattices, giving compositional disordering in the quantum well layer and graded-index regions, thus resulting in lateral optical confinement and reduced optical absorption.

This application demonstrates the possibility and capability of MeV ion beam processing for III-V semiconductor device applications. Precise control, high repeatability, and the low dose requirement give this technique advantages over conventional processing techniques and thus is simplified and thereby more attractive.

6.7. References

1. T. A. Tombrello, Journal de Physique (France), Col. C2 (1989) C2-1.
2. The results have been reported. See: F. Xiong, T. A. Tombrello, H. Wang, T. R. Chen, H. Z. Chen, H. Morkoç, and A. Yariv, Appl. Phys. Lett., 54 (1989) 730; and Mat. Res. Soc. Symp. Proc. Vol. 144 (1989) 367.
3. K. Y. Lau, P. L. Derry, A. Yariv, Appl. Phys. Lett. 52 (1988) 88.
4. P. L. Derry, A. Yariv, K. Y. Lau, N. Bar-chaim, K. Lee, and J. Rosenberg, Appl. Phys. Lett., 50 (1987) 1773.
5. R. D. Dupuis, J. P. Van der Ziel, R. A. Logan, J. M. Brown, and C. J. Pinzone, Appl. Phys. Lett., 50 (1987) 407.
6. Y. Arakawa and A. Yariv, IEEE J. Quant. Elect. QE-21 (1985) 1666.
7. W. T. Tsong, R. A. Logan, and J. A. Ditzenberger, Electron. Lett. 18 (1982) 845; and W. T. Tsong, Appl. Phys. Lett., 40 (1982) 217.
8. P. L. Preey, T. R. Chen, Y. H. Zhuang, J. Paslaski, M. Mittelstein, K. Vahaka, and A. Yariv, Appl. Phys. Lett., 53 (1988) 271; and A. Larsson, M. Mittelstein, Y. Arakawa, and A. Yariv, Electron. Lett. 22 (1986) 79.

9. O. Wada, T. Sanada, M. Kuno, and T. Fujii, Electron. Lett., 21 (1985) 1025.
10. J.R. Shealy, Appl. Phys. Lett. 52 (1988) 1455.
11. T. Tsukada, J. Appl. Phys., 45 (1974) 4899.
12. A. Kurobe, H. Furnyama, S. Naritsuka, Y. Kokubun, and M. Nakamura, Electron. Lett. 22 (1987) 1117.
13. R. L. Thornton, R. D. Burnham, T. L. Paoli, N. Jun. Holonyak, and D. G. Deppe, Appl. Phys. Lett., 47 (1985) 1239.
14. A. Yariv, *Quantum Eletronics*, 3rd edition, (John Wiley and Sons Press, New York) (1989) p.252.
15. J. C. Dyment, J. C. North, and L. A. D'Asaro, J. Appl. Phys. 44 (1973) 207.
16. J. C. Dyment, L. A. D'Asaro, J. C. North, B. I Miller, and J. E. Ripper, Proc. IEEE, 60 (1972) 726.
17. P. N. Favennec, G. P. Pelous, M. Binet, and P. Baudet, in *Ion Implantation in Semiconductord and Other materials*, ed. B. L. Crowder (New York, Plenum) (1973) pp. 621.
18. P. N. Farennec, J. Appl. Phys. 47 (1976) 2532.
19. S. J. Pearton, M. P. Iannuzzi, C. L. Reynolds Jr., and L. Peticolas, Appl. Phys. Lett., 52 (1988) 395.
20. J.M. Blum, J. C. McGroddy, P. G. McMullin, K. K. Shih. A. W. Smith, and J. F. Ziegler, IEEE J. Quant. Elect. QE-11 (1975) 413.
21. H. Beneking, N. Grote, H. Krautle, and W. Roth, IEEE J. Quant. Elect. QE-16 (1980) 500.
22. N. Grote, H. Kraulte, and H. Beneking, in *Gallium Arsenide and Related Compounds*, Inst. Phys. Conf. Ser. 45 (1979) 484.
23. S. Uchiyama, K. Moriki, K. Iga, and S. Furukawa, Japan. J. Appl. Phys. Lett. 21 (1982) L639.
24. D. P. Wilt, B. Schwartz, B. Tell, E. D. Beebe, and R. T. Nelson, Appl. Phys. Lett. 44 (1984) 290.
25. H. Z. Chen, A. Ghaffari, H. Wang, H. Morkoç, and A. Yariv, Appl. Phys. Lett., 51 (1987) 1320.

26. T. Fukuzawa, S. Semura, H. Saito, T. Ohta, Y. Uchida, and H. Makashima, Appl. Phys. Lett. 45 (1984) 1.

27. K. Meehan, P. Gavrilovic, N. Holonyak, Jr., R. D. Burnham, and R. L. Thornton, Appl. Phys. Lett. 46 (1985) 75.

28. P. Gavrilovic, K. Meehan. J. E. Epler, N. Holonyak, Jr., R. D. Burnham, R. L. Thornton, and W. Streifer, Appl. Phys. Lett. 46 (1985) 857.

29. Y. Hirayama, Y. Suzuki, and H. Okamoto, Jap. J. Appl. Phys., 11 (1985) 1498.

30. F. Xiong, T. A. Tombrello, T. R. Chen, H. Wang, Y. H. Zhuang, and A. Yariv, Nucl. Instr. and Methods. B39 (1989) 487.

Chapter 7

CONCLUSIONS AND CLOSING REMARKS

> *This is not the end. It is not even the beginning of the end.*
> *But it is, perhaps, the end of the beginning.*
>
> *(Sir Winston Leonard Spencer Churchill, 1874-1965)*

In conclusion, from the experimental results presented in this work, firstly, it is evident that HEIM induces marked effects in III-V compound semiconductors distinct from LEIM. In addition to deep implantation, HEIM induces also varied lattice damage processes during implantation. Characterizing the MeV-ion-implanted layers in III-V compound semiconductors by a variety of analytical techniques, we have obtained a clear insight of implantation-induced lattice damage and a comprehensive understanding of physical processes involved. As presented in the results in Chapters 2 and 3, and discussed in Chapter 5, MeV ions induce nuclear spikes through nuclear collision cascades at the region close to the EOR of ions, which is very similar to LEIM; they also produce distinct electronic spikes by ionization and excitation in the surface region, which LEIM does not have. Nuclear spikes cause atomic displacement, resulting in persistent structural damage to crystalline lattices. The direct c-a phase transition occurs when these damaged zones undergo a process involving fast intensive heating and rapid quenching. A uniform amorphous layer forms when individual amorphous regions overlap. In the electronic-spike-damaged surface region, however, massive electronic ionization and excitation of lattice atoms stimulate the diffusion of lattice defects and migration of the displaced lattice atoms and implants. Strong evidence of this electronic spike enhanced effect has been revealed in MeV oxygen ion implantation induced Al interdiffusion in AlAs/GaAs SLs (Section 3.4) and in implantation enhanced in situ dynamic damage annealing during RT implantation (Section 3.3). The lattice strain is another distinct feature present in MeV ion implanted crystals. By examining primary lattice defect features and defect generation processes during implantation (Chapter 4), we conclude that it is different defect characteristics (generation, diffusion, and relaxation) that are responsible for the lattice strain build-up and saturation in ion implanted crystals. In most semiconductor crystals, primary vacancies and their complexes are normally dominant after implantation due to ionization-enhanced fast diffusion of interstitials, resulting in positive strain build-up. The strain magnitude is much more pronounced in III-V compounds than in single elemental crystals because of the complicated variety and features of defects in III-V compounds. In the special example of InP crystals (so far the only one case we found), it gives negative strain because interstitials may be possessed with the excess defect population over vacancies due to the high generation rate of indium interstitials and small diffusivity of defects in InP. Implantation-induced high electrical resistivity in III-V compounds is another important effect discovered. MeV nitrogen ions can create a buried semi-insulating layer in InP with resistivity about $10^6\Omega/\sqcup$. Oxygen ions have a selective carrier compensation effect in GaAs, with resulting high resistivity in n-type material. This has been used for electrical isolation as well as carrier confinement in fabricating high efficiency GaAs laser devices, which were presented in Chapter 6.

This work has also demonstrated the complimentary nature of a variety of analytical techniques in charaterizing buried implanted layers produced by MeV ions. The combination of all these modern techniques has made it possible and efficient to study MeV ion beam processing of materials, especially for surface and interface modification and analysis.

MeV ion implantation as an extensive means of ion beam processing for material property modification is still at its beginning stage. It will attract more interest in thenear future in semiconductor technology as well as in other material systems. In a sense, it provides a unique tool for modifying interfaces or buried layers without "scratching" the surface. On the other hand, it can also modify the material surface by the electronic effect, instead of by lattice damage. Semiconductor technology is a very promising field for its application. However, one should get a good understanding of the mechanisms of the lattice damage process and other associated effects under given implantation conditions before putting it into practice. More attention may be required for the work on III-V compound semiconductors Because, as a complex system, they have a complex variety of lattice defects as well as features that are distinct from single elemental semiconductors. Although the investigation results on the subject of MeV ion implantation into III-V compound semiconductors presented in this thesis, which encompass from fundamental studies to practical applications, may be incomplete, we sincerely hope that it has provided an insight and seed that will encourage further interest to be dedicated to this field.

— NOW, ENDS! —

APPENDIX A

A LIST OF THE WORK DONE AT CALTECH

1. *FulinXiong*, T. A. Tombrello, H. Wang, T. R. Chen, H. Morkoç, and A. Yariv, "Fabrication of GaAs/AlGaAs Quantum Well Lasers with MeV Oxygen Ion Implantation", presented in Material Research Society 1988 Fall meeting, published in Mat. Res. Soc. Symp. Proc. Vol. 144 (1989) 367-372.
2. *FulinXiong* and T. A. Tombrello, "MeV Ion Beam Processing in III-V Compound Semiconductors", presented as an invited talk at the Tenth Conference on the Application of Accelerators in Research and Industry, Nov. 7-9, 1988, Denton, Texas; published in Nuclear Instruments and Methods B40/41 (1989) 526-532.
3. *FulinXiong*, T. A. Tombrello, H. Wang, T. R. Chen, H. Z. Chen, H. Morkoç, and A. Yariv, "High Efficiency Single Quantum Well GRINSCH GaAs/AlGaAs Lasers Fabricated by MeV Oxygen Ion Imlantation", Applied Physics Letters, 54(8) (1989) 730-732.
4. *FulinXiong*, C. W. Nieh, and T. A. Tombrello, "XTEM and HRTEM Studies of Structural Phase Transitions in MeV Ion Implanted InP Crystals", Ultramicroscopy 30 (1989) 242-248.
5. *FulinXiong* "XTEM Study of Phase Transition in MeV Ion Implanted InP" (extended abstract), presented in the 46th Annual Meeting of Electron Microscopy Society of America; published Proc. of the 46th Annual Meeting of the Electron Microscopy Society of America, Ed. by G. W. Bailey, San Francisco Press, (1988) 796-797.
6. *FulinXiong*, T. A. Tombrello, T. R. Chen, H. Wang, Y. Zhuang, Yariv, "Formation of Buried High Resistivity Layers in InP Crystals by MeV Nitrogen Ion Implantation", presented at the Sixth International Conference on Ion Beam

Modification of Materials, June 12-17, 1988, Tokyo, Japan; published in Nuclear Instruments and Methods B39 (1989) 487-491.

7. *FulinXiong*, C. W. Nieh, D. N. Jamieson, T. Vreeland Jr., and T. A. Tombrello, "Amorphization and Recrystallization in MeV Ion Implanted InP Crystals", presented in Material Research Society 1987 Fall meeting, published in Mat. Res. Soc. Symp. Proc. Vol. 100 (1988) 105-111.
8. C. W. Nieh, *FulinXiong*, C. C. Ahn, Zhuying Zhou, D. N. Jamieson, B. Fultz, T. Vreeland Jr., and T. A. Tombrello, "Formation of Buried Oxides in Mev Oxygen Ion Implanted Silicon Crystals", presented in Material Research Society 1987 Fall meeting, published in Mat. Res. Soc. Symp. Proc. Vol. 107 (1988) 73-78.
9. *FulinXiong*, C. W. Nieh, D. N. Jamieson, T. Vreeland Jr., and T. A. Tombrello, "Characterization of High Energy Heavy Ion Implanted InP Crystals by a Variety of Techniques", presented in the International Symposium on Application of Ion Beam Produced by Small Accelerators, Oct. 20-24, 1987, Jinan, Shandong, China; published in Vacuum (Great Britain) 39 (1989) 177-182.
10. D. Huang, G. Ji, U. K. Reddy, H. Morkoç, *FulinXiong*, T. A. Tombrello, "Photoreflectance, Absorption and Nuclear Resonant Reaction Studies of $Al_xGa_{1-x}As$ Grown by Molecular Beam Epitaxy", J. Appl. Phys., 63(11) (1988) 5447.
11. *FulinXiong*, T. A. Tombrello, H. Z. Chen, H, Morkoç, and A. Yariv, "Directed Determination of Al Depth content in MBE Grown AlGaAs by NRRA and XRC", presented at the 8th MBE Workshop on Sept. 10-11, 1987 at University of California, Los Angeles; published in J. Vac. Sci. and Tech. B6(2) (1988) 758-762.
12. *Fulin.Xiong*, F. Rauch, Z. Zhou, C. Shi, R. P. Livi, and T. A. Tombrello, "Hydrogen Depth Profiling in Solids: A Comparison of Several Resonant Nuclear Reaction Techniques", Nuclear Instruments and Methods B27 (1987), 432-441.
13. T. Bartin, J. Pronko, F. Junga, W. Opyd, A. Mardinly, *FulinXiong*, and T. A. Tombrello, "Electrical and Structure Changes in GaAs Crystals from High-Energy Heavy-Ion Implants", presented at the 9th Conference on the Application of Accelerations in Research and Industry, Nov. 10-12, 1986, Denton, Texas,

Nuclear Instruments and Methods B24/25 (1987) 548.

14. C. R. Wei, T. Jones, T. A. Tombrello, T. Vreeland, Jr., *FulinXiong*, Z. Zhou, G. Burns, and F. H. Dacol, "Radiation Defect-induced Lattice Contraction of InP", presented in Material Research Society 1986 Fall meeting, published in Mat. Res. Soc. Symp. Proc. Vol. 74 (1986) 517-522.
15. *FulinXiong*, F. Rauch, C. Shi, R. P. Livi, and T. A. Tombrello,"Comparison of Several Nuclear Reaction Techniques for Hydrogen Depth Profiling in Solids", presented in Macrobeam Analysis Society 1986 Annual Meeting; published in Microbeam Analysis -1986, edited by A. Romig, Jr. and W. Chambers, San Francisco Press, (1986) 85-88.